Sofia University "St. Kliment Ohridski"
Faculty of Physics

Simona Ilieva Ilieva

High-energy hadron-nuclear interactions

MEASUREMENT OF THE PRODUCTION CROSS SECTION OF 31 GEV/C PROTONS ON CARBON VIA BEAM ATTENUATION IN A 90-CM-LONG TARGET

DOCTORAL THESIS

submitted for the degree of
Doctor of Philosophy

Scientific specialty: 4.1 Physical sciences
Elementary Particles and High Energy Physics

Scientific supervisor: Assoc. Prof. Mariyan Bogomilov, PhD

March 2021

Abstract

Neutrino beams at accelerator-based neutrino experiments originate from meson decays in flight. These mesons are produced in hadron-nucleus interactions in extended targets. Detailed understanding of the neutrino source is key to neutrino cross-section and oscillation measurements. However, Monte Carlo prediction of the neutrino flux has a limited precision mainly due to large hadron production uncertainties. To improve the flux prediction and lower its systematic uncertainty, modeling of hadronic interactions in simulations is tuned with hadron production data. These data include particle yields and interaction cross sections, which are used to re-weight particle production and interaction rates in Monte Carlo. Purposeful hadron production measurements are performed at the NA61/SHINE fixed target experiment at the CERN Super Proton Synchrotron. Currently, these measurements are tailored to the requirements of the T2K experiment in Japan and the Fermilab long-baseline neutrino beamlines. Employed are beams of different type and energy on targets of various thickness and material. Some NA61/SHINE results have already been implemented in the T2K neutrino flux prediction and have considerably reduced its total systematic uncertainty. The T2K beam is produced in the decays of hadrons, which emerged from the interactions of a 31 GeV/*c* proton beam inside a 90-cm-long graphite target. These interactions are recreated at the NA61/SHINE experiment when a 31 GeV/*c* incident proton beam collides with a replica of the T2K target. Analysis of such data collected in the year 2010 is the focus of this work. The task is to extract the production cross section in $p + C$ interactions at 31 GeV/*c* beam momentum. The maximal magnetic field configuration of the NA61/SHINE spectrometer is used. The dataset contains about 1.2 M recorded events. The adopted strategy is to measure the beam attenuation in the thick target and relate it to the production cross section. Such an approach minimizes the physics model dependence of the final result. The estimated production cross section is

$$\sigma_{\text{prod}} \; = \; 227.6 \; \pm \; 0.8(\text{stat}) \, {}^{+}_{-} \, {}^{1.9}_{3.2}(\text{sys}) \; - \; 0.8(\text{mod}) \text{ mb.}$$

It is in agreement with previous NA61/SHINE results obtained in measurements with a thin graphite target. Compared to them, the current estimate provides improved precision with a total fractional uncertainty of less than 2%. The accordance between the reported production cross section and thin-target values suggests the reason for the observed tension between neutrino flux predictions tuned with thin- and replica-target data is still to be determined. Moreover, the presented result is to be used to constrain the output of the T2K beam simulation by re-weighting the interaction rate of beam protons inside the target. This is expected to further reduce the uncertainty of the T2K neutrino flux.

Contents

List of Tables

List of Figures

Chapter 1

Introduction

Contents

Laboratory neutrino beams are typically initiated by a high-intensity proton beam impinging on a thick target of light material, giving rise to neutrino-yielding hadrons. Measurements related to the production of these hadrons are called hadron production measurements. They are essential for constraining the neutrino flux prediction in neutrino oscillation experiments paying their due in unveiling the elusive nature of neutrinos.

This chapter serves as an introduction to the neutrino particle and neutrino physics. First, neutrino-related discoveries are outlined. Then, the concept of neutrino oscillations and current knowledge of oscillation parameters are described. Finally, the generation of laboratory neutrino beams is discussed and an overview of related hadron production measurements is given.

1.1 Milestones in the history of neutrinos

The discovery of radioactivity and the puzzling at that time continuous electron energy spectrum in β-decay led distinguished members of the physics society back in the 1920s, such as Niels Bohr [1], to question the validity of energy conservation in that process. In 1930, in a memorable letter [2] to his colleagues, Wolfgang Pauli restored the belief in energy conservation by postulating the existence of a neutral, light, spin $1/2$ particle. Four years later, in his theory of β-decay, Enrico Fermi coined the word neutrino as the name of that particle. The first experimental confirmation for the existence of neutrinos was a Nobel prize winning achievement. It was awarded to Clyde Cowan and Frederic Reines who actually observed the neutrino anti-particle: the anti-neutrino [3]. They placed two large tanks of water with cadmium chloride ($CdCl_2$) dissolved in them near a nuclear reactor. The tanks were sandwiched between three scintillator layers. Reactor anti-neutrinos interacted with protons in the solution via inverse β-decay:

$$\bar{\nu} + p \rightarrow n + e^{+}. \tag{1.1}$$

Positrons, which were produced in that process, annihilated with electrons and gave rise to two gamma rays. In addition, neutrons were captured by cadmium and a third gamma ray was released. The coincidence of all three gamma-ray signals gives a unique signature of an anti-neutrino interaction, which Cowan and Reines reported in 1956. Moreover, it was the electron anti-neutrino that was experimentally probed. Neutrinos are the neutral counterpart leptons to the charged leptons $(e^{-}, \mu^{-}, \tau^{-})$ and similarly have three flavours: electron, muon, and tau neutrinos. In 1962, Leon M. Lederman, Melvin Schwartz, and Jack Steinberger discovered the second neutrino flavour: the muon neutrino ν_{μ} [4]. The neutrinos they used were a product of pion decay. The primary pions were produced in the interactions of a 15 GeV proton beam on a beryllium target. The Nobel prize in Physics in 1988 was awarded to the three physicists for the discovery of the muon neutrino and the employed novel neutrino beam method. In 1998 a third neutrino flavour, tau neutrino ν_{τ}, was discovered at the DONUT experiment at Fermilab [5].

In parallel to the discovery of neutrino flavours, another riddle formed. In 1968 Ray Davis reported the first measurements of the neutrino flux originating from nuclear fusion in the Sun. The hypothesis was that the Sun produces electron neutrinos and that all of them reach the Earth. This presumption was tested by putting a tank of chlorine deep underground and counting the number of produced argon atoms in the anticipated reaction:

$$\nu_{e} + {}^{37}Cl \rightarrow {}^{37}Ar + e^{-}. \tag{1.2}$$

The experimental approach allowed Davis to measure the ν_{e} flux. And the reported value was only a third of the expected number shall the Standard Solar Model (SSM) be valid [6]. This discrepancy is known as the solar neutrino problem. One possible explanation to this observation could be neutrino decay. Another suggests that the underlying process leading to this surprising result is neutrino oscillation. The idea of neutrino flavour mixing was introduced by Maki, Nakagawa, and Sakata [7] around the time of the ν_{μ} discovery. Furthermore, in 1967 Pontecorvo proposed neutrino flavour oscillations [8]: one type of neutrino transforms into another. Decades later, neutrino oscillations were experimentally confirmed while probing neutrinos coming from cosmic ray interactions in the atmosphere. In this case, neutrinos are produced in hadron decays in the upper layers of the atmosphere. Then, the expected ratio between muon and electron neutrinos is

$$R(\frac{\nu_{\mu}}{\nu_{e}}) = 2. \tag{1.3}$$

However, a deficit of ν_{μ} to ν_{e} in the atmospheric neutrino flux was observed at the *Kamiokande* underground Cherenkov detector and later at its even larger successor, the *Super Kamiokande* [9]. This result is known as the atmospheric neutrino problem. Next measurements of neutrino energy spectra as a function of zenith angle, reported by the Super-Kamiokande collaboration in 1998 [10], were only consistent with neutrino oscillations. In the end, in 2001 the conclusive evidence of neutrino oscillations came from the Sudbury Neutrino Observatory (SNO) in Canada. The solar neutrino problem was once again examined by looking at three independent neutrino interactions

$$\nu + {}^{2}H \rightarrow p + p + e^{-} \tag{1.4}$$

$$\nu + e^{-} \rightarrow \nu + e^{-} \tag{1.5}$$

$$\nu + {}^{2}H \rightarrow \nu + p + n. \tag{1.6}$$

The first one is sensitive only to ν_{e}. The second process is applicable to all neutrino flavours, but has a preference to electron neutrinos. The third interaction is sensitive to all flavours equally.

The SNO measurements validated the solar ν_e flux results by R. Davis and showed no tension between the measured total neutrino flux and the SSM prediction [11]. The solar neutrino puzzle and the atmospheric neutrino problem were finally resolved by the confirmation of neutrino oscillations. Nowadays, dedicated neutrino oscillation studies provide other experimental and theoretical challenges.

1.2 Properties of the neutrino particle

In the Standard Model (SM) of particles and interactions, neutrinos are electroneutral, massless elementary particles that are fermions and have single state chirality: neutrinos are left-handed and anti-neutrinos are right-handed. Moreover, neutrinos pair with the corresponding charged leptons to form left-handed weak isospin doublets that couple to the weak gauge bosons. In the SM, there are three neutrino flavours: electron, muon, and tau neutrinos. They match the number and flavour of the charged leptons counterparts of the isospin doublets. In principle, additional neutrino states could exist, but they would not couple to the W and Z gauge bosons and are consequently called sterile neutrinos. At present, there is no strong experimental evidence that such neutrinos exist. On the other hand, neutrino oscillations are experimentally confirmed. They indicate that neutrinos are massive, see Sec. 1.4. Neutrino oscillations are a manifestation that neutrino flavour eigenstates $(\nu_e, \nu_\mu, \nu_\tau)$ and neutrino mass eigenstates (ν_1, ν_2, ν_3) are not identical. The mechanism that generates masses of the neutrinos is not yet understood. However, some constraints on neutrino masses exist. From precise measurements of the end of the electron energy spectrum in β-decay, the KATRIN collaboration announced in 2019 an upper limit of the electron neutrino mass of $m_\nu < 1.1$ eV (90% CL) [12]. An additional constraint on neutrino masses and also on the number of neutrino flavours comes from cosmological measurements. In such cases, reported values depend on many cosmological parameters and assumptions. For example, combining measurements from the Planck experiment of the fluctuations in the cosmic microwave background with baryon acoustic oscillations (BAO) data, the effective number of neutrino flavours becomes $N_{\text{eff}} = 2.99 \pm 0.17$ [13]. This value is in agreement with the Standard Model prediction. Also in Ref. [13], a limit on the sum of neutrino masses $\Sigma m_\nu < 0.12$ eV is assessed when one assumes a free degenerate active neutrino mass and combines the Planck data with BAO measurements.

To theoretically describe massive neutrinos, one must go beyond the Standard Model and introduce a mass term to the SM Lagrangian. One possibility to do so is to presume neutrinos acquire mass the same way other massive SM particles do - via the Higgs mechanism. Then, a Dirac mass term is constructed in the form

$$Ł_D = -m_D(\bar{\nu}_R \nu_L + \bar{\nu}_L \nu_R). \tag{1.7}$$

Contrary to the SM, where all neutrinos are left-handed, a Dirac term introduces a right-handed neutrino component, ν_R. It allows neutrino coupling to the Higgs field. The Dirac mass, m_D, is the respective coupling constant. The left-handed neutrino is denoted by ν_L. By construction the Dirac mass term conserves total lepton number, L. This means neutrinos and anti-neutrinos must have opposite lepton numbers: $L(\bar{\nu}) = -L(\nu)$. Therefore, a Dirac mass term implies neutrinos and anti-neutrinos are distinct particle states.

Since neutrinos have no electric charge, another possibility to assign a mass term to them is to assume the neutrino is its own anti-particle. Then one can use the charge conjugate of the left-handed neutrino, ν_L^C, which is right-handed, and obtain a Lorentz-invariant left-handed Majorana mass term

$$Ł_{ML} = -\frac{1}{2} M_L \bar{\nu}_L^C \nu_L + h.c., \tag{1.8}$$

where C denotes charge conjugation. The right-handed Majorana mass term is

$$Ł_{MR} = -\frac{1}{2} M_R \bar{\nu}_R^C \nu_R + h.c. \tag{1.9}$$

These two mass terms violate total lepton number conservation by $\Delta L = \pm 2$. Furthermore, a left-handed Majorana mass term is forbidden in the SM as it breaks $SU(2)_L$ gauge invariance. A combination of a Dirac and a Majorana mass terms gives a general mass term of type

$$\begin{aligned} -\text{Ł}_{MD} &= m_D(\bar{\nu}_R\nu_L + \bar{\nu}_L\nu_R) + \frac{1}{2}M_L\bar{\nu}_L^C\nu_L + \frac{1}{2}M_R\bar{\nu}_R^C\nu_R + h.c. \\ &= \frac{1}{2}(\bar{\nu}_L^C, \bar{\nu}_R)\begin{pmatrix} M_L & m_D \\ m_D & M_R \end{pmatrix}\begin{pmatrix} \nu_L \\ \bar{\nu}_R^C \end{pmatrix} + h.c. \end{aligned} \tag{1.10}$$

After the mass matrix in Eq. 1.10 is diagonalized, which is done using unitary operators, neutrino flavor eigenstates are transformed to mass eigenstates. If $M_L = 0$, which is consistent with the SM, and if $M_R >> m_D$, the obtained mass eigenvalues after diagonalization are

$$M_\nu = \begin{pmatrix} m_D^2/M_R & 0 \\ 0 & M_R \end{pmatrix}. \tag{1.11}$$

Since m_D represents the strength of the Yukawa coupling of neutrinos to the Higgs field, it is expected that m_D is of the order of the charged fermion masses, i.e. ~ 1 MeV. In the approximation that M_R is much larger than m_D, the heavier the mass eigenstate $m_2 = M_R$, the lighter the state $m_1 = M_D^2/M_R$. This is the See-Saw mechanism [14–16]. It provides a natural explanation as to why neutrino mass is much smaller than the mass of other charged leptons and gives a sterile neutrino candidate: the heavy ν_2 state. It also requires that neutrinos are Majorana particles[1]. If the neutrino is its own anti-particle, a process called neutrinoless double beta decay is possible:

$${}^A_ZX \rightarrow {}^A_{Z+2}Y + 2e^-. \tag{1.12}$$

Currently several experiments [17–19] are trying to detect such a process, but its existence is not officially confirmed.

1.3 Flavour mixing

If neutrinos have non-zero masses, a set of mass eigenstates $|\nu_i\rangle$ (i = 1, 2, 3, ..., n) with defined masses, m_i, will exist. The mass eigenstates are the eigenstates of the free Hamiltonian and describe the neutrino propagation. On the other hand, neutrino interactions with matter are described by the flavour eigenstates $|\nu_\alpha\rangle$ with a defined flavour α. The flavour eigenstates couple to the gauge bosons. When a reaction with neutrino production occurs, each generated neutrino has a fixed flavour, but an unknown mass. As a result, it can be presented as a superposition of the mass eigenstates

$$\nu_\alpha = \sum_i U_{\alpha i}^* \nu_i, \tag{1.13}$$

where $U_{\alpha i}^*$ is a unitary matrix, called neutrino mixing matrix. If neutrinos are massless, this matrix is the identity. Equation 1.13 can be inverted to describe mass eigenstates as a mixture of flavour eigenstates:

$$\nu_i = \sum_i U_{\alpha i}\nu_\alpha. \tag{1.14}$$

The neutrino mixing matrix in the case of 3 neutrino flavours can be expressed in terms of three mixing angles, θ_{12}, θ_{13}, and θ_{23}, a CP-violating phase, δ_{CP}[2], and two Majorana phases, α_1 and α_2. In this

---

[1] A Lagrangian having both Dirac and Majorana mass terms implies neutrinos are Majorana particles.

[2] δ_{CP} is often called Dirac phase.

parameterization the mixing matrix is

$$U_{\alpha i} = \begin{pmatrix} U_{e1} & U_{e2} & U_{e3} \\ U_{\mu 1} & U_{\mu 2} & U_{\mu 3} \\ U_{\tau 1} & U_{\tau 2} & U_{\tau 3} \end{pmatrix} =$$

$$= \begin{pmatrix} c_{12}c_{13} & s_{12}c_{13} & s_{13}e^{-i\delta_{CP}} \\ -s_{12}c_{23} - c_{12}s_{23}s_{13}e^{i\delta_{CP}} & c_{12}c_{23} - s_{12}s_{23}s_{13}e^{i\delta_{CP}} & s_{23}c_{13} \\ s_{12}s_{23} - c_{12}c_{23}s_{13}e^{i\delta_{CP}} & -c_{12}s_{23} - s_{12}c_{23}s_{13}e^{i\delta_{CP}} & c_{23}c_{13} \end{pmatrix} \begin{pmatrix} e^{i\alpha_1/2} & 0 & 0 \\ 0 & e^{i\alpha_2/2} & 0 \\ 0 & 0 & 1 \end{pmatrix} \quad (1.15)$$

$$= \begin{pmatrix} 1 & 0 & 0 \\ 0 & c_{23} & s_{23} \\ 0 & -s_{23} & c_{23} \end{pmatrix} \begin{pmatrix} c_{13} & 0 & s_{13}e^{-i\delta_{CP}} \\ 0 & 1 & 0 \\ -s_{13}e^{i\delta_{CP}} & 0 & c_{13} \end{pmatrix} \begin{pmatrix} c_{12} & s_{12} & 0 \\ -s_{12} & c_{12} & 0 \\ 0 & 0 & 1 \end{pmatrix} \begin{pmatrix} e^{i\alpha_1/2} & 0 & 0 \\ 0 & e^{i\alpha_2/2} & 0 \\ 0 & 0 & 1 \end{pmatrix},$$

where $s_{ij} = sin\theta_{ij}$, $c_{ij} = cos\theta_{ij}$, $i = 1, 2, 3$ and $\alpha = e, \mu, \tau$. This matrix is known as the PMNS (Pontecorvo-Maki-Nakagawa-Sakata) matrix. Without loss of generality, it is a standard convention to take the angles $\theta_{ij} \,\epsilon\, [0, \pi/2]$ and the phase $\delta_{CP} \,\epsilon\, [0, 2\pi]$. If neutrinos are Dirac fermions, the matrix containing the Majorana phases, α_1 and α_2, is the identity. The Majorana phases only appear in lepton number violating processes, such as neutrinoless double beta decay. They do not enter neutrino oscillation probabilities since neutrino oscillations conserve lepton number.

1.4 Neutrino oscillations in vacuum

As previously mentioned, neutrinos are produced in charged-current processes[3] as specific flavour states, $|\nu_\alpha\rangle$, that are a superposition of the mass eigenstates

$$|\nu(t=0)\,\rangle = |\nu_\alpha\rangle = \sum_i U^*_{\alpha i}\,|\nu_i\rangle\,. \quad (1.16)$$

Here t denotes the time and $t = 0$ refers to the initial state. Travelling through space, however, it is the mass eigenstates $|\nu_i\rangle$ that evolve with time. If the neutrino propagates through vacuum, each of the mass eigenstates will acquire its own phase factor, $e^{-iE_i t}$, where $E_i = \sqrt{p_i^2 + m_i^2}$ is the energy of the i-th mass eigenstate. With time, the neutrino state will no longer be a pure flavour eigenstate

$$|\nu(t)\rangle = \sum_i U^*_{\alpha i} e^{-iE_i t}\,|\nu_i\rangle = \sum_i U^*_{\alpha i} e^{-iE_i t} \sum_\beta U_{\beta i}\,|\nu_\beta\rangle\,. \quad (1.17)$$

The probability that after time t, the neutrino state will be the flavour eigenstate $|\nu_\beta\rangle$ is

$$P(\nu_\alpha \to \nu_\beta) = |\langle\nu_\beta|\nu(t)\rangle|^2 = \left|\sum_i U_{\beta i} U^*_{\alpha i} e^{-iE_i t}\right|^2\,. \quad (1.18)$$

When a neutrino is produced in one flavour eigenstate, but during propagation evolves in time to a different flavour eigenstate, the process is called neutrino oscillation. For ultra-relativistic neutrinos[4], if

---

[3] The weak interaction mediated by the charged $W^\pm$ bosons is a charged-current one.

[4] Ultra-relativistic neutrinos have mass which is much smaller compared to their total energy, i.e. $E_i = \sqrt{p_i^2 + m_i^2} \simeq p_i + m_i^2/(2E)$.

one assumes the mass eigenstates are described as plane waves and their momenta are all equal ($\vec{p_i} = \vec{p}$), the probability for neutrino oscillation in vacuum becomes

$$\begin{aligned} P(\nu_\alpha \to \nu_\beta) = \delta_{\alpha\beta} - 4\sum_{i>j} Re\left[U^*_{\alpha i}U_{\beta i}U_{\alpha j}U^*_{\beta j}\right] sin^2\left(\frac{\Delta m^2_{ij}L}{4E}\right) \\ +2\sum_{i>j} Im\left[U^*_{\alpha i}U_{\beta i}U_{\alpha j}U^*_{\beta j}\right] sin^2\left(\frac{\Delta m^2_{ij}L}{2E}\right), \end{aligned} \tag{1.19}$$

where $\delta_{\alpha\beta}$ is the Kronecker delta, $L \simeq ct$ is the distance travelled by the neutrino and $\Delta m^2_{ij} = m^2_i - m^2_j$. The probability that anti-neutrinos oscillate is

$$\begin{aligned} P(\bar{\nu}_\alpha \to \bar{\nu}_\beta) = \delta_{\alpha\beta} - 4\sum_{i>j} Re\left[U^*_{\alpha i}U_{\beta i}U_{\alpha j}U^*_{\beta j}\right] sin^2\left(\frac{\Delta m^2_{ij}L}{4E}\right) \\ -2\sum_{i>j} Im\left[U^*_{\alpha i}U_{\beta i}U_{\alpha j}U^*_{\beta j}\right] sin^2\left(\frac{\Delta m^2_{ij}L}{2E}\right). \end{aligned} \tag{1.20}$$

Any difference between the neutrino and the anti-neutrino oscillation probabilities in Eqs. 1.19 and 1.20 would indicate CP violation in the lepton sector. It would be possible only if the mixing matrix is complex. On the contrary, the survival (non-oscillation) probability for neutrinos and anti-neutrinos

$$P(\nu_\alpha \to \nu_\alpha) = P(\bar{\nu}_\alpha \to \bar{\nu}_\alpha) = 1 - 4\sum_{i>j}\left[U^*_{\alpha i}U_{\alpha i}\right] sin^2\left(\frac{\Delta m^2_{ij}L}{4E}\right) \tag{1.21}$$

is identical as $U^*_{\alpha i}U_{\beta i}U_{\alpha j}U^*_{\beta j}$ is real for $\alpha = \beta$. This means CP violation is experimentally observable only if one looks for the appearance of a given neutrino flavour in an initial neutrino flux of another flavour. Oscillation probabilities depend on the Dirac (CP-violating) phase. However, they are not sensitive to the Majorana phases since the combination $U^*_{\alpha i}U_{\beta i}$ enters Eqs. 1.19 and 1.20. Furthermore, oscillation probabilities depend on the sine of the squared differences of the neutrino masses. Therefore they indicate neither the sign of the mass splittings nor the masses themselves. In case all neutrino masses are zero or degenerate

$$P(\nu_\alpha \to \nu_\beta) = \delta_{\alpha\beta} \tag{1.22}$$

and neutrinos do not oscillate. Solar and atmospheric neutrino data indicate this is not the case. As neutrinos produced in the Sun or emitted in the collisions of cosmic rays with the atmosphere have different energy scales, solar and atmospheric neutrino oscillation experiments are sensitive to different squared mass splittings. Atmospheric oscillations are mostly of type $\nu_\mu \to \nu_\tau$ and depend on the mass splitting

$$\Delta m^2_{atm} \approx 2 \times 10^{-3} eV^2. \tag{1.23}$$

Solar neutrinos are produced as ν_e and during their propagation oscillate to ν_μ or ν_τ. The relevant squared mass splitting in this case is

$$\Delta m^2_{sol} \approx 8 \times 10^{-5} eV^2. \tag{1.24}$$

The difference between these mass splittings is about two orders of magnitude. In addition, the solar neutrino data indicates the sign of Δm^2_{sol}. Thus, it is known that $m_2 > m_1$. However, there is no experimental evidence whether the third mass eigenstate, mass indicated by m_3, is the lightest or the heaviest one. It is a well-established convention that mass ordering $m_3 > m_2 > m_1$ is denoted

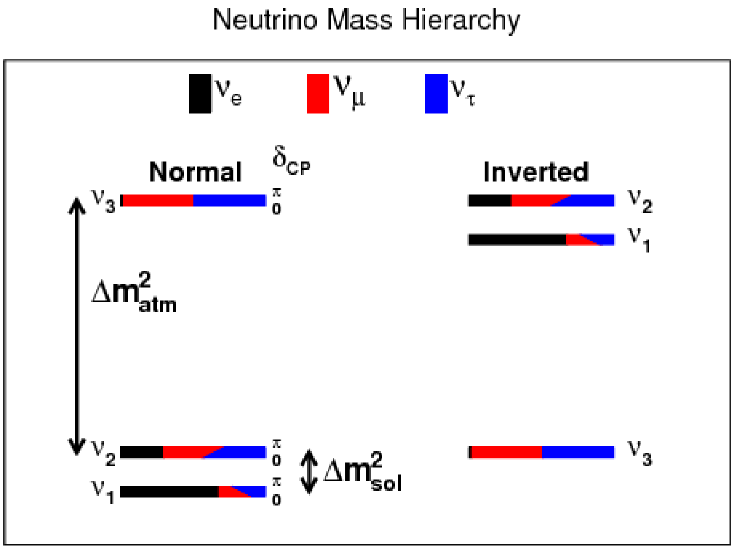

Fig. 1.1: Neutrino ν_e, ν_μ, and ν_τ flavour content in neutrino mass eigenstates ν_1, ν_2, and ν_3 for normal (left) and inverted (right) mass ordering. The change in flavour content as a function of δ_{CP} is also given. The figure is from Ref. [20].

as the normal hierarchy and $m_2 > m_1 > m_3$ is the inverted hierarchy. Mass ordering and flavour composition of mass eigenstates is portrayed in Fig. 1.1.

An interesting case, which is also relevant for neutrino oscillation experiments, is the two-flavour neutrino oscillation. In that case, the mixing matrix, U, is parameterized by a single mixing angle, θ, and becomes

$$U = \begin{pmatrix} cos\theta & sin\theta \\ -sin\theta & cos\theta \end{pmatrix}. \tag{1.25}$$

In addition, the vacuum Hamiltonian for two neutrino flavours is

$$H = \frac{\Delta m^2}{4E} \begin{pmatrix} cos2\theta & sin2\theta \\ -sin2\theta & cos2\theta \end{pmatrix}. \tag{1.26}$$

Then, the probability for the oscillation $\nu_\alpha \to \nu_\beta$ in vacuum, described by the same mixing angle, θ, and a single mass squared difference, Δm^2, is

$$P(\nu_\alpha \to \nu_\beta) = P(\bar{\nu}_\alpha \to \bar{\nu}_\beta) = sin^2 2\theta sin^2 \left(\frac{\Delta m^2 L}{4E} \right), \beta \neq \alpha. \tag{1.27}$$

As the oscillation probabilities for neutrinos and antineutrinos are the same, CP violation is impossible. The probability in Eq. 1.27 is sensitive to two theoretical parameters, namely the mixing angle and the mass splitting, and two experimental parameters: the neutrino energy, E, and the distance between the neutrino source and the detector, L. The mixing angle is related to the amplitude of the oscillation, while the squared mass splitting is related to its wavelength. Respecting typical units of neutrino energy and detector-source distance, the probability in Eq. 1.27 can be rewritten to

$$P(\nu_\alpha \to \nu_\beta) = P(\bar{\nu}_\alpha \to \bar{\nu}_\beta) = sin^2 2\theta sin^2 \left(1.27 \Delta m^2 [eV^2] \frac{L[km]}{E[GeV]} \right), \beta \neq \alpha. \tag{1.28}$$

In practice, the ratio L/E is the experimental quantity in studies of neutrino oscillations in both vacuum and matter.

1.5 Neutrino oscillations in matter

When neutrinos travel through matter, such as the Sun, the Earth, a supernova, they interact with the medium. The corresponding Hamiltonian, H, has two terms:

$$H = H_0 + V. \tag{1.29}$$

One of them is the free kinetic term, H_0, which describes neutrino propagation in vacuum. The other one, labelled here as V, is induced by neutrino interactions with matter electrons and nucleons. Both charged and neutral current interactions can occur. They are mediated by Z and W bosons respectively. As flavour is conserved in SM processes, only ν_e and $\bar{\nu}_e$ interact with electrons via charged currents (CC). These interactions have potential

$$V_{CC} = \pm\sqrt{2}G_F N_e, \tag{1.30}$$

where positive sign is for electron neutrino and negative one is for electron anti-neutrino, G_F is the Fermi constant, $G_F = 1.166 \times 10^{-5} GeV^{-2}$, and N_e is the number density of electrons. On the other hand, each neutrino flavour and matter constituent can participate in neutral current (NC) interactions. The corresponding matter potential term is

$$V_{NC} = -\frac{G_F}{\sqrt{2}} N_x, \tag{1.31}$$

where N_x is the number density of neutrons that depends on the spatial position, x. In Eq. 1.31, the potential contributions from electrons and protons cancel out since matter is usually neutral: $N_p = N_e$.

Once again, lets now refer to a two-flavour neutrino case. More specifically, lets consider ν_e and ν_μ flavours. The Hamiltonian for these two neutrino flavours is

$$H = \frac{\Delta m^2}{4E}\begin{pmatrix} cos2\theta & sin2\theta \\ -sin2\theta & cos2\theta \end{pmatrix} + V_{CC}\begin{pmatrix} 1 & 0 \\ 0 & 0 \end{pmatrix} + V_{NC}\begin{pmatrix} 1 & 0 \\ 0 & 1 \end{pmatrix}, \tag{1.32}$$

where the first term describes neutrino propagation in vacuum, see Eq. 1.26, and the following two potential terms take into account that CC interactions are relevant for ν_e only, while both neutrino flavours, ν_e and ν_μ, participate in NC interactions. The Hamiltonian in Eq. 1.32 can be transformed [21] to the form

$$H = \frac{\Delta m_M^2}{4E}\begin{pmatrix} cos2\theta_M & sin2\theta_M \\ -sin2\theta_M & cos2\theta_M \end{pmatrix}, \tag{1.33}$$

where the matter mixing angle θ_M and the mass splitting Δm_M^2 are defined as

$$sin^2 2\theta_M \equiv \frac{sin^2 2\theta}{sin^2 2\theta + (cos2\theta - x)^2} \tag{1.34}$$

$$\Delta m_M^2 \equiv \Delta m^2 \sqrt{sin^2 2\theta + (cos2\theta - x)^2} \tag{1.35}$$

$$x \equiv \frac{2\sqrt{2}G_F N_e E}{\Delta m^2}. \tag{1.36}$$

The Hamiltonian in Eq. 1.33 has the same form as the one in Eq. 1.26. The two are identical under the substitution: θ_M to θ and Δm_M^2 to Δm^2. Therefore, one expects that matter effects also induce neutrino oscillations. Moreover, the probability for two-flavour oscillation in matter is

$$P(\nu_\alpha \to \nu_\beta) = sin^2 2\theta_M sin^2\left(\frac{\Delta m_M^2 L}{4E}\right) \beta \neq \alpha \tag{1.37}$$

It is same as that for oscillations in vacuum, see Eq. 1.27, under the above-mentioned parameter exchange.

Despite these similarities, neutrino oscillations are modified when neutrinos pass through matter. The reason is that CC interactions single out ν_e. This was first pointed out by Mikheev, Smirnov, and Wolfenstein in Refs. [22, 23] and is called the MSW effect. For neutrino propagation in matter, there exists a resonance where flavour mixing is maximal. It happens for $sin^2 2\theta_M = 1$, which is satisfied for a mixing angle $\theta_M = \pi/4$. In such a case, $x = cos2\theta$ and the resonant number density of electrons, N_e^R, is

$$N_e^R = \frac{\Delta m^2 cos2\theta}{2\sqrt{2}G_F E}. \tag{1.38}$$

It is important to note that θ_M can have maximal magnitude regardless of the value of θ, as long as $\theta \neq 0$. But the matter density may or may not stay constant along the neutrino path. Thus the condition in Eq. 1.38 might be met at a given stage of neutrino propagation. Such a scenario can happen in the Sun. Solar neutrinos are created as electron ones in the dense regions the Sun's core. There the electron density is larger than the one in Eq. 1.38. Also, the mixing angle at neutrino production is almost 90° and electron neutrinos are produced primarily as one of the mass eigenstates. One can assume the Sun's plasma has a smooth density variation from the core towards the surface. Consequently, neutrinos pass through a region where $N_e = N_e^R$, mixing is enhanced, and the dominant flavour component of a given mass eigenstate changes. Later on, neutrinos escape the Sun and enter the vacuum. There electron density drops to zero. Solar neutrinos continue their propagation in vacuum and may reach a detection point where neutrino flavour composition gets measured. The survival probability, P_{ee}, in such a scenario is given by $P_{ee} = sin^2\theta$, which significantly differs from the one expected in vacuum: $P_{ee} = 1 - \frac{1}{2}sin^2 2\theta$. This is the reason for the deficit of solar ν_e measured by R. Davis in 1968 and the SNO collaboration in 2001. Neutrino oscillations in matter and the MSW effect in the Sun explain the solar neutrino puzzle.

1.6 Neutrino oscillation experiments

1.6.1 Types

Neutrino flavour transitions are experimentally studied at neutrino oscillation experiments. These experiments are sensitive to the mixing angles and the mass squared differences. There are generally two types of oscillation experiments: disappearance and appearance ones. In neutrino disappearance experiments researchers look for a deficit of neutrinos of the initial flavour type at some distance from the neutrino source. In neutrino appearance experiments, after the beam travels a certain distance, one looks for neutrinos of any flavour other than the initial one. Actually, the oscillation probabilities in both vacuum and matter, see Eqs. 1.27 and 1.37, depend on the ratio of two experimental parameters: L/E, where L is the distance between the neutrino source and the detector and E is the neutrino energy. The signature of neutrino oscillations is flavour composition that displays periodic variations for a given L/E ratio.

When neutrinos originate from natural sources, such as the Sun, both neutrino energy and distance to the source are fixed. If the neutrino source is man-made, detectors can be placed at a desired distance and neutrino energy might be fixed or a subject to selection. For instance, nuclear reactors are artificial sources of antineutrinos, whose energy is defined by nuclear fission. Human-made neutrino beams can also be produced in the decays of mesons in flight. Those mesons are produced in hadron-nucleus interactions of proton beams on extended targets[5]. This was the Nobel prize-winning approach used by Lederman, Schwartz and Steinberger in Ref. [4]. In that case, the energy spectrum of detected neutrinos can be selected by changing the proton beam energy or placing the detector at a given angle to the neutrino beam direction. The setting of the ratio L/E means that a neutrino oscillation

---

[5] The thickness of an extended target is of the order of a meter.

experiment is optimized to examine a particular mass splitting. The reason for this can be found in Eq. 1.28 and is further explained as follows:

$$\text{If} \quad \Delta m^2 << E/L, \qquad \text{then} \quad < sin^2\left(1.27\Delta m^2 \frac{L}{E}\right) >\approx 0 \quad \text{and} \quad \begin{array}{l} P(\nu_\alpha \to \nu_\beta) \approx 0 \\ P(\nu_\alpha \to \nu_\alpha) \approx 1 \end{array}$$

$$\text{If} \quad \Delta m^2 >> E/L, \qquad \text{then} \quad < sin^2\left(1.27\Delta m^2 \frac{L}{E}\right) >\approx \frac{1}{2} \quad \text{and} \quad \begin{array}{l} P(\nu_\alpha \to \nu_\beta) \approx \frac{1}{2} sin^2 2\theta \leq \frac{1}{2} \\ P(\nu_\alpha \to \nu_\alpha) \geq \frac{1}{2} \end{array}$$

In case $\Delta m^2 << E/L$, the oscillation probability is too small to be experimentally observed. In case $\Delta m^2 >> E/L$, the oscillations average over the source-detector distance and sensitivity to mass splitting is lost. Maximal sensitivity is achieved when $\Delta m^2 \sim E/L$. Respective of the chosen, or naturally defined, distance between the neutrino source and the detector, experiments divide to short or long baseline ones. Short baselines are of the order of hundreds of meters, while long ones are of the order of hundreds of kilometers. Regardless of the baseline length or neutrino energy, neutrino oscillation experiments targeting the solar or atmospheric mass splitting are operating in solar or atmospheric regime. Observations in the solar regime provide information about the mixing angle θ_{12}, while searches in the atmospheric one are sensitive to θ_{23}. Currently, measurements of the third mixing angle, θ_{13}, are carried out by reactor and accelerator-based neutrino experiments. In reactor neutrino experiments oscillation parameters are measured by comparing the neutrino flux coming from nuclear reactors placed at different distances from the detector. In accelerator neutrino experiments, on the other hand, the beam composition near the neutrino source is compared to the one measured at some distance L. Accelerator neutrino beams will be further discussed in Sec. 1.7.

1.6.2 Current status of measurements

Since the establishment of neutrino oscillations, measurements of related parameters are being carried out at numerous experiments of various types. This results in the continuous development of employed experimental techniques and the regular updates of measured values: squared mass splittings, mixing angles and the CP-violating phase. It also sometimes leads to tension between results reported by different collaborations. Up until very recently that was the case for the solar mass splitting results of the KamLAND experiment [24] and solar neutrino experiments like the Super-Kamiokande (SK) [25] experiment. KamLAND is a reactor neutrino experiment that measures electron anti-neutrinos produced at 53 nuclear reactors, which have different proximity to the 1-kiloton liquid scintillator detector. SK is a 50-kiloton water Cherenkov detector that is designed to study neutrino oscillations and proton decay. The value of Δm^2_{12} preferred by KamLAND was a bit higher than the one from solar experiments. With the newest SK results [26], this discrepancy of the best-fit Δm^2_{12} values has decreased from 2σ to around 1σ, as shown on Fig. 1.2 and in Ref. [27].

In the atmospheric regime, measurements of mixing angles and squared mass splittings are made at atmospheric experiments, such as IceCube DeepCore [29, 30] and SK, and at accelerator-based long-baseline neutrino experiments, like T2K [31], MINOS [32] and NOνA [33]. The latest results are given in the left panel of Fig. 1.3. The data from T2K [34] and NOνA [35] have the best precision, which is indicated by the corresponding narrower contours on Fig. 1.3. For inverted mass ordering (IO), there is a mild preference for the second octant of θ_{23}, i.e. $\sin^2\theta_{23} > 0.5$. It originates from the T2K data [36].

The third mixing angle, θ_{13}, is most precisely determined in reactor neutrino experiments. Its value was reported by Double Chooz, Daya Bay, and RENO in 2012 [38–40]. The value of θ_{13} was of particular interest since it was the last non-zero mixing-angle announcement. All mixing angles must differ from 0 to have CP violation in the lepton sector. Latest reactor neutrino results are summarized in the right panel of Fig. 1.3. Overall, they are in good agreement.

Current knowledge of the CP-violating phase, δ_{CP}, is presented in Fig. 1.4. Leptonic CP violation is tested by comparing the probabilities $P(\nu_\mu \to \nu_e)$ vs $P(\bar{\nu}_\mu \to \bar{\nu}_e)$ in appearance experiments. Recent updates on the bounds of δ_{CP} were made by T2K [34, 41] and NOνA [35]. Their results come from

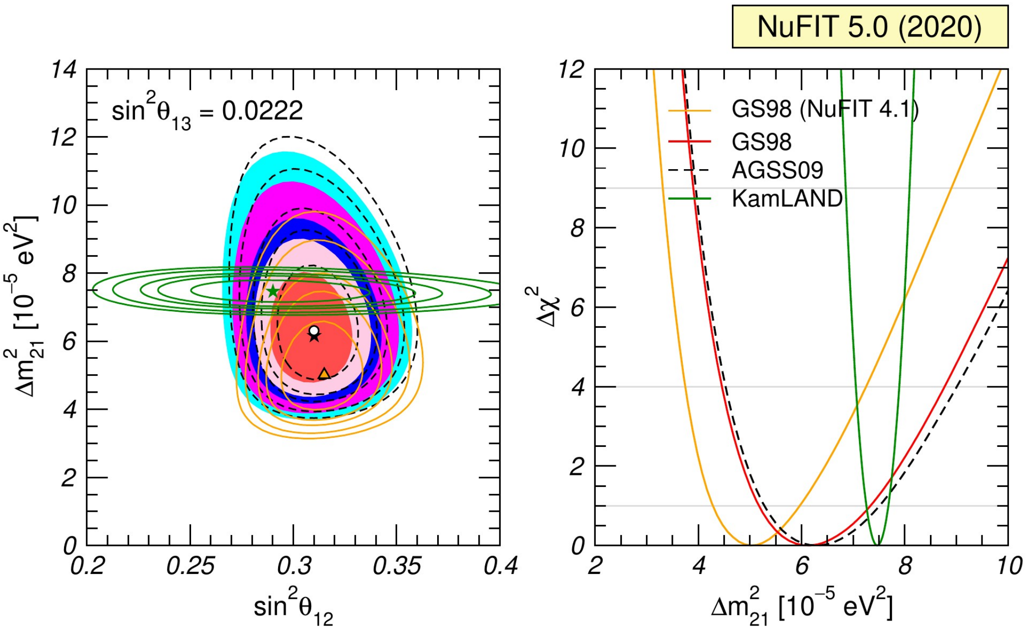

Fig. 1.2: Left: Allowed contours of Δm^2_{12} *vs.* $\sin^2\theta_{12}$ *for solar data combined with two versions of the Standart Solar Model, GS98 and AGSS09 [28] (coloured regions with best fit marked by a black star or contour lines with a white dot for the best fit value) and for KamLAND data (solid green lines and best fit marked by a green star) with fixed* $sin2\theta_{13} = 0.022$ $(\theta_{13} = 8.6°)$*. The orange lines indicate the previous result of the global analysis of solar data. Right:* $\Delta\chi^2$ *dependence on* Δm^2_{12} *for the same analyses after marginalizing (integrating) over* θ_{12}*. The figure is taken from Ref. [27].*

combined analyses of both neutrino and antineutrino oscillation data. Measurements from the two collaborations are in best agreement in the IO case, and if $\delta_{\mathrm{CP}} \approx 3\pi/2$. For the NO though, there is tension between the results: T2K data again shows a preference for $\delta \approx 3\pi/2$, which is disfavoured by NOνA. Combining T2K and NOνA data with reactor data yields improvement in the determination of δ_{CP}, due to the existing correlation between θ_{13} and the CP phase.

1.6.3 Global fit and future prospects

Latest experimental results, some of which were presented in the previous Sec. 1.6.2, are combined together in global fits. The following results are assessed from the global analysis NuFIT 5.0 [27] of neutrino oscillation data, which was available by July 2020. Two-dimensional projections of confidence regions for the six-dimensional fit of the six oscillation parameters, $\theta_{12}, \theta_{23}, \theta_{13}, \Delta m^2_{21}, \Delta m^2_{31}$ (NO) or Δm^2_{32} (IO), and δ_{CP}, are presented in Fig. 1.5. The global fit confirms the slight preference for the second octant of θ_{23} with best fit at $\sin^2_{23} = 0.57$. The best fit for the CP phase is $\delta_{\mathrm{CP}} = 195°$. If one restricts to IO, where T2K and NOνA results for δ_{CP} agree the most, the CP phase remains close to the maximal CP-violating value, $\delta_{\mathrm{CP}} = 3\pi/2$. As for the mass ordering, the current global analysis indicates NO is still preferred as in previous fits [43], but with decreased significance. Inverted ordering is now disfavored at 1.6σ level, while this level used to be 2.5σ in the previous NuFit 4.1. This decrease is also related to the latest results by the T2K and NOνA collaborations that favour IO.

With these updated data, the allowed 3σ ranges for the elements of the leptonic mixing matrix, the PMNS matrix, are

$$|U|^{\text{with SK1−4 atm}}_{3\sigma} = \begin{pmatrix} 0.801 \to 0.845 & 0.513 \to 0.579 & 0.143 \to 0.155 \\ 0.234 \to 0.500 & 0.471 \to 0.689 & 0.637 \to 0.776 \\ 0.271 \to 0.525 & 0.477 \to 0.694 & 0.613 \to 0.756 \end{pmatrix}. \tag{1.39}$$

---

[6] It has been recently reported in Ref. [42] that a sensitive measurement of δ_{CP} at present cannot be provided by separate analysis of neutrino and antineutrino channels.

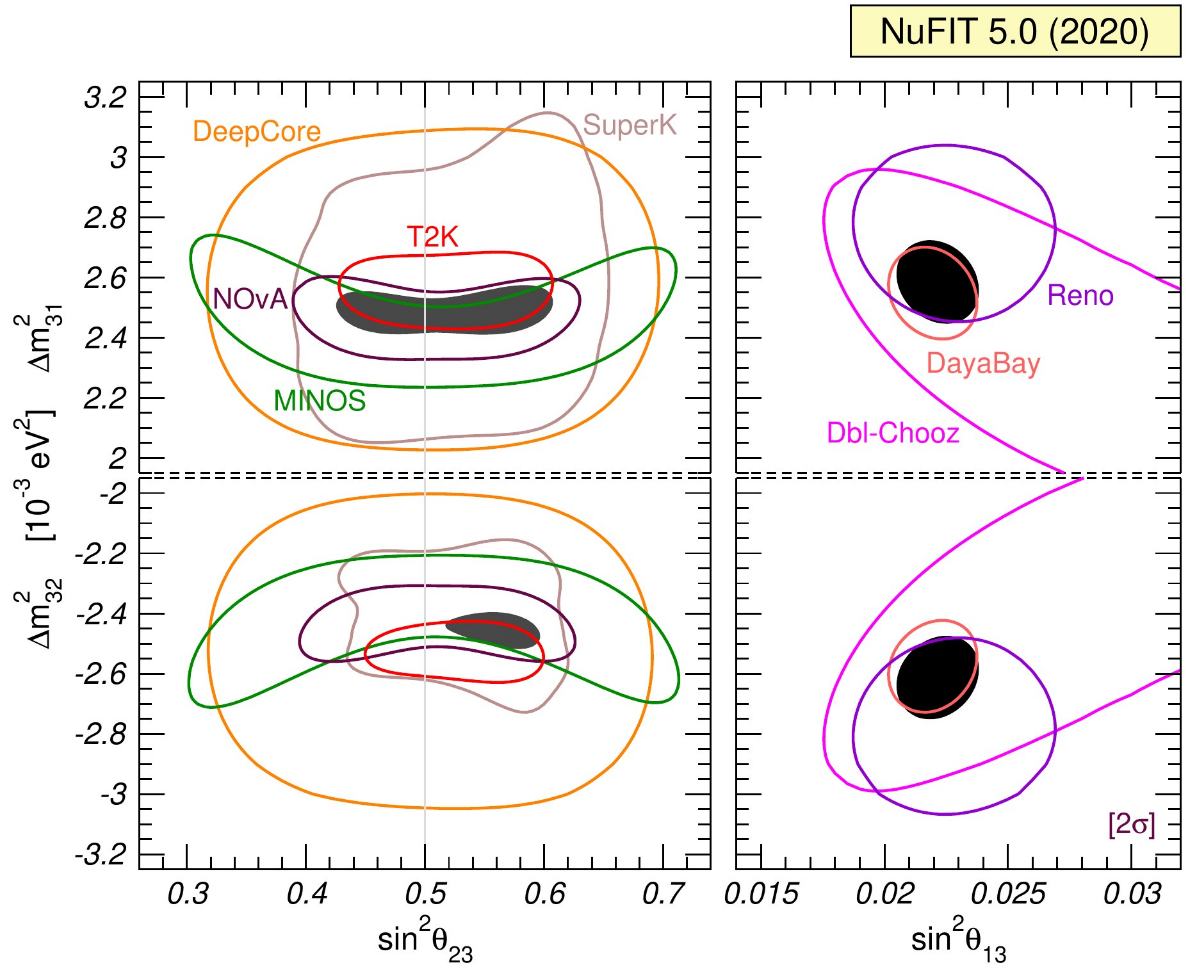

Fig. 1.3: Atmospheric and reactor neutrino data, where upper panels show results for the normal mass ordering (NO) case (index $l = 1$) and lower ones for the inverted mass ordering (IO) case ($l = 2$). Left: Allowed regions of $\sin^2\theta_{23}$ and Δm^2_{31}. Data from MINOS (green), NOνA (dark-redwood) and T2K (red), as well as atmospheric data from IceCube DeepCore (orange) and SK (light-brown) is given. A combination of all these data is indicated by the dark-grey area. Here a prior on θ_{13} is included to account for reactor bounds. Right: Allowed regions of $\sin^2\theta_{13}$ and Δm^2_{31} from Daya-Bay (pink), Double-Chooz (magenta) and RENO (violet) data. Their combination is given in the black regions. In all panels solar and KamLAND data for θ_{12} and Δm^2_{21} are used. Contours are defined with respect to the global minimum of the two mass orderings. The figure is taken from Ref. [37].

For a discussion of the used notation for U, see the caption of Fig. 1.5. Knowledge of the PMNS matrix elements is improving. Still, the current precision of their values is much lower than that of the elements of the quark mixing matrix, which can be found in the Particle Data Group report in Ref. [44].

Another global fit of neutrino oscillation data is available in Ref. [45]. At present, pending issues to be addressed at neutrino oscillation experiments include the mass ordering and the value of the CP-violating phase. Determination of these two parameters will have an impact on other studies as well. The models that predict the matter-antimatter asymmetry in the early universe would benefit from a precise measurement of δ_{CP} in the lepton sector. On the other hand, neutrino mass ordering is crucial for neutrino mass models. The key to better measurements of both mass ordering and δ_{CP} is precise knowledge of θ_{23} as the appearance probabilities depend on $\sin^2\theta_{23}$. Currently, some progress is made in the determination of θ_{23}: a mild preference to the second octant is recognized. Next generation of neutrino experiments, such as DUNE [46] and Hyper-K [47], will have increased sensitivity to θ_{23}, the CP phase, and mass hierarchy. Until then, the current long-baseline accelerator neutrino experiments T2K and NOνA provide the most stringent data.

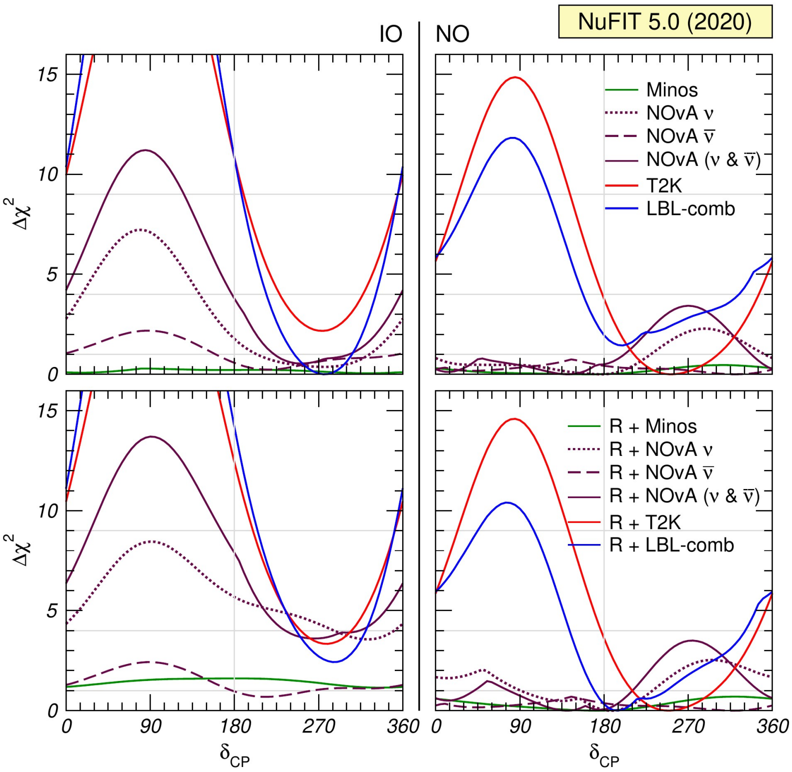

Fig. 1.4: Bounds on $\delta_{\rm CP}$ from MINOS (green), NOνA (dark-redwood), T2K (red) and their combined result (blue). Neutrino data from NOνA are given by dotted lines, while NOνA anti-neutrino data are shown as dashed lines[6]*. A combination of the two is presented as a solid line. The left panels correspond to the IO case, the right ones to NO. The upper panels show $\delta_{\rm CP}$ from long-baseline accelerator experiments (LBL) with the inclusion of a prior on θ_{13} that accounts for reactor bounds. Lower panels show $\delta_{\rm CP}$ constraints for the combination of the full LBL and reactor experiments data. In all panels solar and KamLAND data for θ_{12} and Δm^2_{21} are used. $\Delta\chi^2$ is defined with respect to the global minimum of the two mass orderings. The figure is taken from Ref. [37].*

1.7 Laboratory neutrino beams

The generation of a man-made neutrino beam is a multistage process. First, a hadron beam, typically a proton one, is accelerated at an accelerator complex. Then, the beam collides with a target. There are two alternatives for the target type. In one of them, the target is a large block of a dense material. It serves as a beam dump and absorbs most of the beam protons and their long-lived secondary products. However, some of the short-lived particles, such as charmed mesons, will decay to neutrinos before interacting. The produced neutrinos will leave the target to create a neutrino beam. This is the beam dump method. It was employed by the DONUT collaboration to generate a tau neutrino beam in the decays of D_S mesons, which were produced in a tungsten target [5].

In another approach, the accelerated proton beam is focused onto a nuclear target of light material, such as carbon or beryllium. As a result, particles of different type are produced. Later on, a set of magnetic horns is used to select particle charge. Magnetic horns are essentially aluminum coaxial conductors, which generate a toroidal magnetic field when electrical current flows through them [48]. By setting the direction of the current in the horns, positively or negatively charged particles are focused. These particles further continue propagation in a decay volume, which is long enough to let them decay to neutrinos. The majority of produced neutrinos come from pion and kaon decays and are muon neutrinos. Actually, hadrons of positive charge give rise to neutrino beams, while negatively charged ones generate anti-neutrino fluxes. The decay volume is usually filled with helium or is under vacuum to minimize particle interaction inside it. The choice of the initial hadron beam energy, the target material, and its dimensions aims to maximize pion and kaon production in the target.

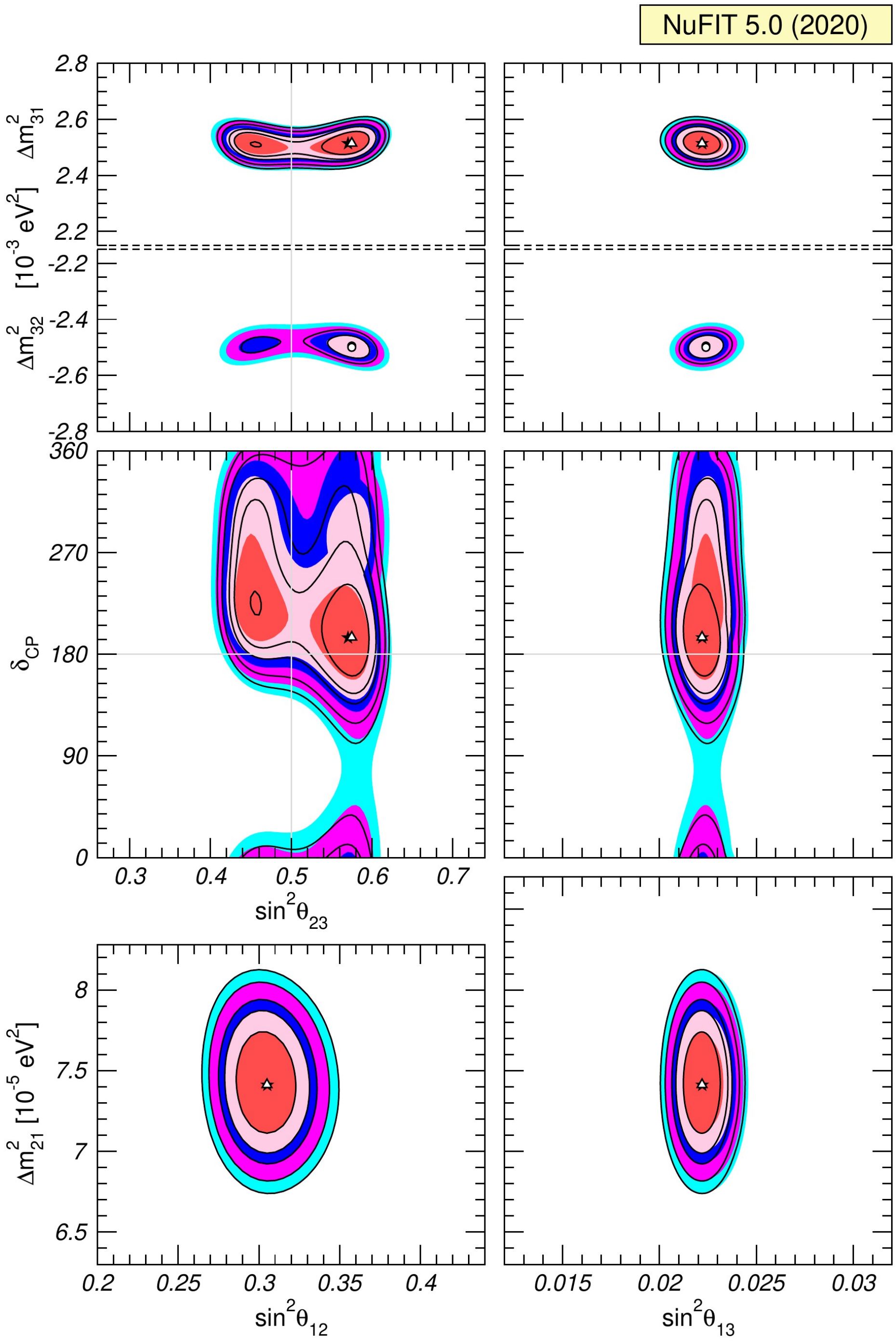

Fig. 1.5: Global 3ν oscillation analysis. Each panel shows the two-dimensional projection of the allowed six-dimensional region after marginalization with respect to the undisplayed parameters. The global analysis is carried out with and without the tabulated χ^2 map for SK atmospheric data from Runs 1 to 4. Coloured bands (black contour curves) represent results without (with) those maps. The different contours correspond to the two-dimensional allowed regions at 1σ, 90%, 2σ, 99%, 3σ CL (2 dof). The regions in the lower four panels are obtained from $\Delta\chi^2$ minimized with respect to the mass ordering. The figure is taken from Ref. [27].

After the decay volume, a beam dump absorbs most of the charged particles remaining present in the beam. However, in addition to neutrinos, high-energy muons can escape this absorber. These muons are further detected by muon monitors placed after the dump. This way, the intensity of the beam and its direction can be probed. As for the rest of particles, they are set free to propagate through the ground. The soil stops all particles other than neutrinos, which continue their flight in the desired direction. In the end, a focused, narrow-band neutrino beam is created.

As described above, neutrino beam generation is a complex process. Around 90% of the obtained neutrinos are decay products of hadrons produced in the target. Others originate from decays of particles, which emerged from out-of-target interactions of secondary hadrons, e.g. in the magnetic horns. In order to make flavour oscillation measurements, one has to understand the neutrino source. However, placing a detector in the high-intensity secondary hadron beam after the target will affect the beam evolution. The other option is to have a detailed full chain Monte Carlo simulation of the neutrino beam generation. But for some of the relevant momentum and angular regions, Monte Carlo models provide very different predictions of hadron production and so of the neutrino beam composition and energy spectrum [49]. Because of these limitations of both in situ measurements and simulations, hadronic beamline interactions dominate the neutrino flux uncertainty at accelerator-based neutrino experiments. To lower it down, data from external hadron production experiments are used to constrain hadron production in Monte Carlo. These reference data include interaction cross sections and particle yields. The latter are often given in terms of momentum-angle phase space. It is worth noting that Monte Carlo models keep developing, benefiting from the growing amount of hadron production data. In the next section, hadron production measurements and their implementation in neutrino beam simulations are discussed.

1.8 Hadron production measurements

Hadron production data can be implemented in the generators of hadronic interactions or used to re-weight Monte Carlo output, when predicting the neutrino flux for a given beamline. Hadron production experiments are fixed-target experiments that are performed over a wide range of incident beam momenta between 10 and 450 GeV/c, using proton and pion beams on targets of different materials (Be, C, Al, etc.) [50]. Here selected measurements will be discussed.

The NA20 and the NA56/SPY experiments at CERN studied hadron production in proton interactions on beryllium targets with beams at 400 and 450 GeV/c, respectively. Charged pion, kaon, proton, and anti-proton yields were extracted for targets of different lengths and later converted to inclusive cross sections for particle production [51–54]. In order to allow extrapolation to different beam energies, these cross-section data were parameterized using the BMPT parameterization by Bonesini *et al.* [55]. The proposed empirical formula described the NA20 and NA56/SPY data with 10% accuracy. Nevertheless, when scaled to lower energies, the differences between the data and the BMPT estimates increase. Figure 1.6 presents the comparison of the BMPT parameterization with one-particle inclusive production cross-section data, which was measured in 24 GeV/c proton beam interactions on a beryllium target [56]. As Fig. 1.6 shows, the shapes of the measured and the parameterized distributions are in good agreement. However, the BMPT results of pion production are 35% lower compared to data at that momenta [55]. Additionally, Bonesini *et al.* offer a scaling to different target materials. This A-dependent scaling was originally tested when extrapolating beryllium to carbon data. It is now, for instance, used at T2K to adapt carbon-target data to an aluminium-target case and scale interactions in the horn material [57].

The HARP experiment [58] at the CERN Proton Synchrotron conducted systematic pion-production measurements for proton beams in range 1.5 – 15 GeV/c on various targets. The results were given in terms of double-differential cross sections. In most of the measurements, the thickness of the targets along the beamline was about 5% of an interaction length, λ_I [59, 60]. Still, measurements with solid cylindrical targets of $1\lambda_I$ were performed in order to examine the extrapolation of thin-target data to the thick-target case [61]. In addition, the HARP collaboration used the Sanford-Wang empirical

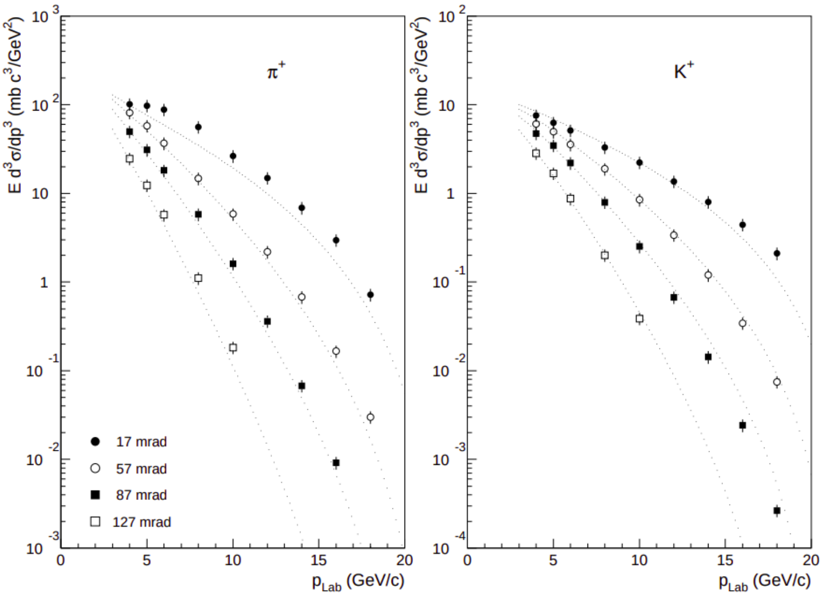

Fig. 1.6: Comparison between the BMPT parameterization based on NA56/SPY and NA20 data (dashed line) and the one-pion (left) and one-kaon (right) inclusive invariant cross sections (points) in $p + Be$ interactions at 24 GeV/c. The figure is taken from Ref. [55].

formula [62–64] to fit their pion-production results[7] [60]. A view of parameterized and measured pion-production data in $p+C$ interactions at 12 GeV/c beam momenta is given in Fig. 1.7. The parameterization deviates from the data at large momenta and polar angle regions. Besides them, there is reasonable agreement between the two. This demonstrates available data coverage can be extended to additional momentum-angle phase space or scaled to different target material and incident beam momenta. HAPR results were used in the neutrino flux calculation at the K2K [65], the MiniBooNE [66] and the SciBooNe [67] experiments to constrain pion production. These data were used as input for the simulation of pion production in the target.

Some hadron production experiments took data that was specifically tailored to the neutrino flux prediction at a given neutrino oscillation experiment. Such was the case for the MIPP experiment [69], which collected data relevant to the Fermilab's NuMI[8] line [70]. The experiment measured charged particle production cross sections using beams of $\pi^{\pm}, K^{\pm}, p$, and $\bar{p}$ in range $5 - 120$ GeV/c on various targets, such as beryllium, carbon, aluminium, and liquid hydrogen. MIPP had a dedicated run with 120 GeV/c protons on the NuMI target, resulting in charged pion yields [71] and an estimate of the K/π production ratio [72]. These results are used to weight the pion and kaon yield prediction from Monte Carlo and form the "thick target" flux prediction for the NuMI beam, namely for the MINERνA experiment [73]. Some of MIPP's data is also of interest for atmospheric neutrino studies and simulations of cosmic-ray air showers.

At present, hadron production measurements are being conducted at the NA61/SHINE experiment at CERN's Super Proton Synchrotron [74]. NA61/SHINE is a successor of the NA49 [75] experiment, which also provided hadron production data. Currently, NA61/SHINE has a dedicated program of reference measurements for T2K and Fermilab neutrino experiments. The latter include MINERνA, NOνA, and DUNE, which are on both the NuMI and the future Long Baseline Neutrino Facility (LBNF) beamlines. Hadron production data from NA61/SHINE includes total and differential cross sections as well as differential charged and neutral particle yields in thin- and thick-target measurements [76]. Used are proton, pion, and kaon beams at energies $30 - 120$ GeV/c and targets of carbon,

---

[7] In this procedure data with $p_{Beam} \geq 5$ GeV/c were used as for lower momenta there were problems in the convergence of the fit.

[8] NuMI stands for Neutrinos at the Main Injector

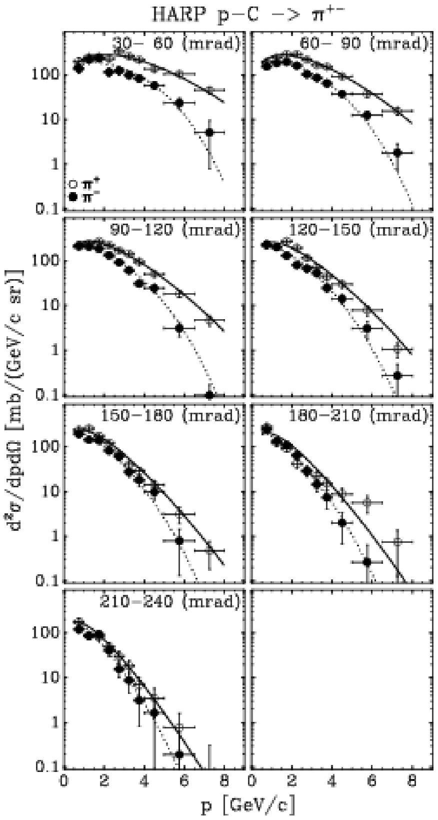

Fig. 1.7: HARP measurement of the double-differential production cross-section of positive (open circles) and negative (filled circles) pions in p+C interactions at 12 GeV/c beam momentum as a function of pion momentum in different polar angle ranges. The curves show the Sanford-Wang parameterization. The figure is taken from Ref. [68].

beryllium, and aluminium. Thick-target runs with copies (replicas) of the T2K and the NuMI targets were also performed. More details about the NA61/SHINE's T2K-related data-taking campaign are given in Chap. 3, Sec. 3.4. The vast majority of these results are already incorporated in the T2K neutrino flux prediction. In doing so, the hadronic interaction uncertainty of the T2K flux was reduced to about 5% at the neutrino energy peak [77]. As for the Fermilab-related measurements, finalized analyses are given in Refs. [78–80]. A few other studies are ongoing. The NA61/SHINE collaboration plans more hadron production measurements in the next years, focusing on high-energy charged kaon production and interactions [77]. Also, measurements with the Hyper-K [47] and the LBNF replica targets are being planned.

A brand new hadron production experiment has been recently proposed: the EMPHATIC experiment at the Fermilab Test Beam Facility [81]. It is designed to make high-precision measurements using proton and kaon beams at 2 − 120 GeV/*c* momenta on various thin nuclear targets. These data are expected to improve flux predictions at accelerator and atmospheric neutrino experiments. In 2018, EMPHATIC completed a test run in order to verify the detector's capabilities of making forward scattering measurements. In the next few years, three phases of data-taking periods are planned, including runs in the sparsely covered low-momentum region below 10 GeV/*c* [81].

Besides dedicated hadron production measurements, there are data that are also used to constrain neutrino beam simulations but were originally carried out for a different purpose: understanding nuclear interactions in high-energy hadron-nucleus collisions [82–84]. These data provide cross-section estimates for various target materials (Li, Be, C, Al, Pb, etc.) and beams of different types (p, $\pi^{\pm}$, $K^{\pm}$, $\bar{p}$) in a wide energy range. Such measurements are gradually being replaced by new hadron production results.

Chapter 2

T2K and its neutrino flux prediction

Contents

T2K (Tokai to Kamioka) is a long-baseline neutrino oscillation experiment that searches for ν_e appearance in an initial ν_μ beam to measure the mixing angle θ_{13} and for ν_μ disappearance to measure the mixing angle θ_{23} and mass difference Δm^2_{32}. The muon neutrino beam is initiated in the interactions of a 30 GeV proton beam from the Japan Proton Accelerator Research Complex (J-PARC) with a 90-cm-long graphite target. As a result, pions and kaons are produced and later on decay in flight to neutrinos. At 280 m from the target, where oscillation effects are expected to be negligible, the properties of the initial neutrino flux are measured by near detectors. Further on, at 295 km away from the J-PARC facility, oscillation effects are expected to be significant. There, at the far detector, Super-Kamiokande (SK), neutrino flavour transitions are detected. The T2K setup is presented in Fig. 2.1. To enhance the desired signal, the near and the far detectors are 2.5° off-axis to the initial neutrino beam, which results in peak energy of about 0.6 GeV. Neutrino oscillations pronounce themselves in the difference between measured and predicted neutrino flux at SK. The prediction of the flux at the far detector is based on a full chain simulation of neutrino production. As such, it is strongly dependent on the modeling of hadronic interactions inside the target. In the T2K flux prediction, hadron production data from NA61/SHINE are used to constrain meson production in the target. Accordingly, the associated model dependency of the prediction is reduced, and a step towards more precise oscillation measurements is made.

An overview of the T2K experiment is presented in this chapter, focusing on the neutrino beam generation in reality and simulation. The re-weighting procedure applied to the beam simulation output is also described and the uncertainties of the flux prediction are discussed.

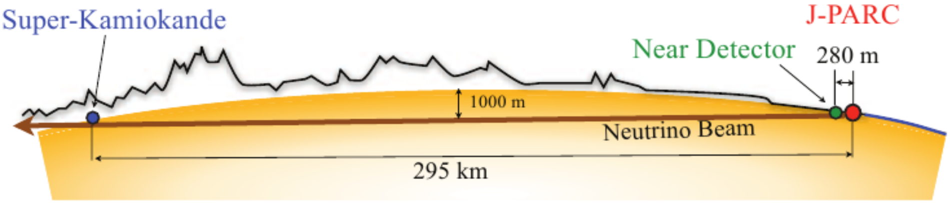

Fig. 2.1: The journey of a T2K neutrino from J-PARC, pass the Near Detectors, to Super-Kamiokande. The figure is taken from Ref. [31].

2.1 The T2K experiment

A comprehensive overview of the T2K experiment is given in Ref. [31]. Summarized information on the T2K experimental setup is proposed here.

2.1.1 Proton and neutrino beamlines

The origin of the neutrino beam at T2K is the J-PARC complex at Tokai, Japan. The acceleration chain consists of three accelerators: a linear accelerator (LINAC), a rapid-cycling synchrotron (RCS), and a synchrotron called the Main Ring (MR). First, H^- ions are accelerated to 400 MeV kinetic energy by the LINAC. Then, the electrons of the H^- ions are stripped and the resulting H^+ beam is accelerated to 3 GeV by the RCS. Afterwards, the proton beam is injected into the MR and accelerated to 30 GeV in eight bunches. From the MR, there are two extraction points: slow extraction for the hadron beamline and fast extraction for the neutrino beamline. The latter one is used for the T2K experiment. All eight bunches are extracted at once and form one beam spill. Some of the design parameters of the produced beam are 750 kW beam power at 30 GeV beam kinetic energy with approximately 3×10^{14} protons per spill. However, up to now the maximal achieved beam power is 515 kW.

The T2K neutrino beamline is composed of a primary and a secondary beamline. Its schematic overview is given in Fig. 2.2. The primary beamline transports the proton beam towards the target. It consists of a preparation section, an arc section, and a final focusing section. In the preparation and the final focusing sections, the beam is guided by normal conducting magnets. In the arc section, superconducting magnets bend the beam towards the direction of the secondary beamline by 80.7°. In all three sections, the beam is sampled to measure its intensity, position, profile, and particle loss. This way, a stable high-power beam operation is ensured. Moreover, these measurements are important for the neutrino flux prediction as the number of protons on target and beam profile size influence hadron production in the target. The systematic uncertainty of the beam width measurement is 200 μm, while the absolute proton beam intensity is measured with a 2% precision.

In the secondary beamline, the beam protons collide with the graphite target, neutrino-yielding hadrons are produced, focused by magnetic horns, and decay to neutrinos. The volume of this line is filled with helium at atmospheric pressure to reduce pion absorption. The secondary line consists of three parts: a target station, a decay volume, and a beam dump.

First is the target station, which consists of a baffle, an Optical Transition Radiation monitor (OTR), the target and three magnetic horns. An overview of this setup is given in Fig. 2.3. The baffle is a graphite block with a beam hole of 3 cm diameter. It serves as a beam collimator. The OTR is a system that uses the transition radiation (visible light) produced when the beam goes through a thin titanium-alloy foil tilted at 45° to the incident protons. This radiation is directed away from the beamline and used to produce an image of the proton beam profile.

The target is a graphite cylinder that is 90 cm in length, which corresponds to 1.9 interaction lengths, λ_I, and has a 2.6-cm diameter of the base. Its density is 1.8 g/cm^3. In 2020, T2K reached an all-time total of 1.97×10^{21} POT[1] in neutrino mode and 1.63×10^{21} POT in anti-neutrino mode [34].

---

[1] POT stands for Protons On Target.

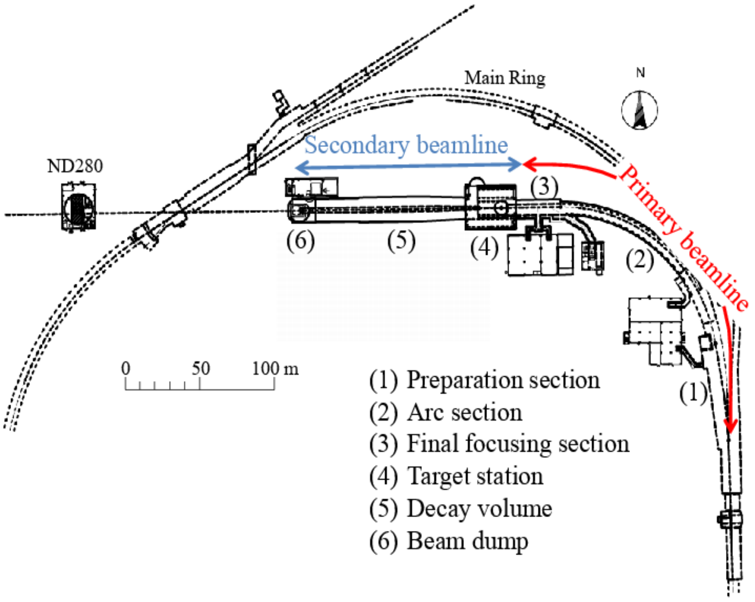

Fig. 2.2: A schematic view of the T2K primary and secondary beamlines. The figure is taken from Ref. [31].

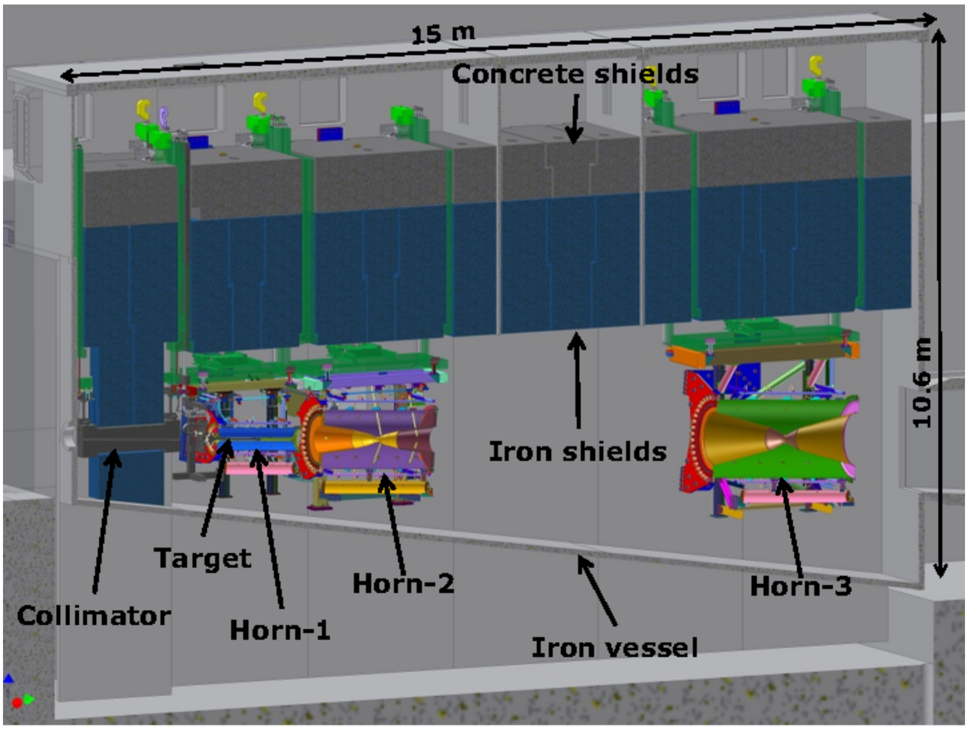

Fig. 2.3: Schematic diagram showing the target, the baffle (collimator), and the three magnetic horns. The figure is from Ref. [85].

The target core is surrounded by a 2-mm-thick graphite tube and is sealed in a 0.3-mm-thick titanium case. Helium gas flows through the gaps between the core and the tube and between the tube and the case to cool the target core. At the designed beam power of 750 kW, the temperature at the center of the target is expected to reach 700°.

The whole target vessel is placed inside the first magnetic horn, which collects the generated charged mesons. The other two horns focus them. Each of the three horns represents two coaxial conductors (inner and outer) that create toroidal magnetic field: the field varies as $1/r$ with the distance, r, from the horn axis. The horns are operated with a low-frequency pulsed current, which is synchronized with the beam spill. The full width of the current pulse is 3.6 ms. Its maximal value is 320 kA, which corresponds to a 2.1 T field. The measurement of the absolute current value has less than 2% uncertainty. The uncertainty of the magnetic field strength is approximately 2% for the first and less than 1% for the next two horns.

Charged particles are generated in nuclear interactions inside the production target. Then, the magnetic horns guide them to a decay volume, where these particles decay in flight. The decay volume is a 96-m-long steel tunnel. Its width and height (W × H) at the upstream and the downstream ends are W × H = 1.4 m × 1.7 m and W × H = 3.0 m × 5.0 m, respectively. The decay volume is surrounded by a 6-m-thick reinforced concrete shielding and is cooled by water. At its end, a beam dump absorbs all non-decayed hadrons. The core of the dump is a 75-ton graphite block that is placed in a helium vessel. Two iron plates are also installed inside the vessel, while fifteen more are situated outside it. The total thickness of the iron material is 2.4 m.

Only muons with energy above 5 GeV escape the beam dump. As muons are mainly produced alongside neutrinos in the pion two-body decay, they can be used to check the intensity and direction of the neutrino beam. For this purpose, after the beam dump, the muon flux is measured by a muon monitor. This monitor comprises of two types of detector arrays: ionization chambers and silicone PIN photo-diodes. Its intrinsic resolution for beam intensity measurements is less than 0.1%, while the design requirement is 3%. The muon profile center resolution is less than 0.3 cm, again better than the required 2-cm value. Nuclear emulsion trackers are installed downstream of the muon monitor to measure the absolute muon flux and its momentum distribution.

2.1.2 Off-axis method

T2K employs an off-axis technique [86] to enhance the neutrino oscillation signal that it is designed to observe. This method alters the shape and intensity of the neutrino flux in two ways. First, when considering pion decay, $\pi^{\pm} \to \mu^{\pm} + \nu_{\mu}(\bar{\nu_{\mu}})$, pions in a wide range of energies contribute to a much narrower range of neutrino energies in an off-axis beam. Second, for a high-energy primary proton beam and a given off-axis angle, a narrow-band high-intensity neutrino beam is achieved. These effects follow from kinematic relations and are explained in detail in Ref. [87]. In the T2K neutrino beamline, the generated muon neutrino (anti-neutrino) flux is directed at a 2.5° angle to the baseline connecting the target site and the far detector. The off-axis angle value is chosen such that for the energy of the neutrino flux peak at the far site, the oscillation probability is in its first maximum. This is presented in Fig. 2.4. At an off-axis angle of 2.5°, most neutrinos have energy of about 0.6 GeV. The T2K far detector, the SK, is 295 km away from the production target. For the resulting L/E ratio, the $P(\nu_{\mu} \to \nu_{\mu})$ survival probability is at a minimum, while the appearance probability $P(\nu_{\mu} \to \nu_{e})$ is at a maximum[2]. The off-axis angle at T2K can be set to as low as 2°, if variation of the peak neutrino energy is desired. The suppression of the high-energy neutrino tail is another benefit of the off-axis method as most of the background signal at SK is in that part of the spectrum.

---

[2] Actually, most of the initial muon neutrinos oscillate to tau neutrinos at SK. However, ν_{τ} appearance in the ν_{μ} beam is non-observable since obtained tau neutrinos are too low in energy to detect.

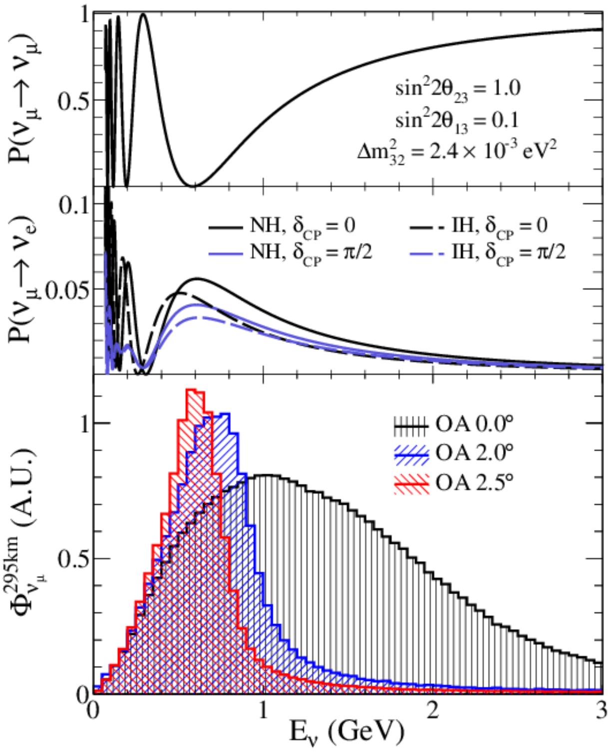

Fig. 2.4: The ν_μ survival and the ν_e appearance probabilities as a function of neutrino energy at 295 km from the production target. Top: Muon neutrino survival probability. Middle: Electron neutrino appearance probabilities. Bottom: Neutrino fluxes for different values of the off-axis angle (OA) in case of no flavour oscillation. The appearance probability is shown for two values of the CP phase, δ_{CP}, and for normal (NH) and inverted (IH) mass hierarchies (ordering). At 600 MeV beam energy, the ν_μ survival probability is minimized, while the ν_e appearance is maximized. The figure is taken from Ref. [88].

2.1.3 Near detector site

The properties of the un-oscillated neutrino beam are first sampled at 280 m from the target by two detectors: an off-axis near detector (ND280) and an on-axis Interactive Neutrino Grid (INGRID).

ND280

The off-axis ND280 detector probes the initial neutrino flux to

- provide input for the determination of the ν_μ flux at SK,
- measure the ν_e contamination in the initial beam as a function of neutrino energy,
- study the ν_μ interactions to allow predictions of the background in the ν_e appearance signal at Super-Kamiokande.

To facilitate all these measurements, the ND280 consists of several sub-detectors, which are shown on Fig. 2.5. First upstream is a pi-zero detector (POD), followed by a tracker that consists a sandwich of three time projection chambers (TPC) and two fine-grained detectors (FGD). These two detector systems are surrounded by an electromagnetic calorimeter (ECAL). All of these detectors are placed inside the old CERN UA1/NOMAD magnet [89], which provides a dipole magnetic field of 0.2 T. In addition, the magnetic yoke is instrumented with scintillators to serve as side muon range detector (SMRD).

The POD measures the ν_μ neutral current interactions on a water target

$$\nu_\mu + N \rightarrow \nu_\mu + N + \pi^0 + X. \tag{2.1}$$

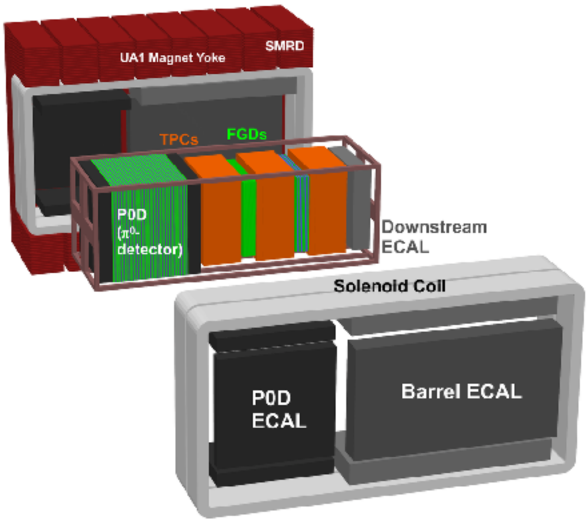

Fig. 2.5: An overview of the ND280 off-axis detector. The figure is taken from Ref. [31].

These are the main background channel for ν_e appearance in SK. The POD comprises of x and y planes of scintillator bars alternating with fillable water bags, brass and lead sheets. The described structure forms a neutrino target, where the water bags can be full or empty. This allows to use a subtraction method to determine the water-target cross sections.

In the tracker, the TPCs provide 3D track reconstruction, particle identification via dE/dx measurements, and also momentum determination as they are placed inside the UA1 magnet. These detectors are boxes filled with gas, where a cathode plane and a segmented sense plane[3] create a uniform electric field that is roughly aligned with the external magnetic field. When a charged particle passes through the gas, it ionizes it to produce electrons, which drift towards the segmented sense plane. The position in 2D is determined from the segment's position on the sense plane. The third coordinate is obtained from the electron drift time. The sense planes are read out by 72 micromegas detectors [90]. The used gas mixture is Ar:CF_4:iC_4H_{10} (95:3:2). The position resolution of the TPCs is typically around 0.7 mm. The energy loss resolution is about 7.8% for minimum ionizing particles[4], which is less than the design requirement of 10%.

Also in the tracker, the two fine-grained detectors (FGDs) provide a target for neutrinos and tracking of produced charged particles. Their dimensions are identical, but their structure is different. The first FGD consists of 30 layers of 192 scintillator bars each. The layers are perpendicular to the beam and are oriented in the x or y direction in an alternating manner. The second FGD comprises of seven modules of plastic scintillator alternating with six layers of water. Each of the seven scintillator modules has two layers of 192 scintillator bars: one aligned in the horizontal direction and the next in the vertical direction. The total number of scintillator bars is 2,688. The total thickness of the water layers is 15 cm. Measurements of interaction rates in the two FGDs allow to determine interaction cross sections for neutrinos in carbon and water.

An electromagnetic calorimeter (ECAL) surrounds the POD, TPCs, and FGDs. It employs layers of plastic scintillator bars as active material, while lead absorber layers are placed in between them. The ECAL has 13 modules: six of them surround the tracker (TPCs+FGDs) on four sides, parallel to the z (beam) axis, and one downstream module (Ds-ECAL) covers the tracker's exit, another six modules surround the POD detector on its four sides (POD-ECAL). The ECAL measures the energy and the direction of photons and allows reconstruction of π^0's produced in neutrino interactions inside the detectors it encloses.

---

[3] The sense plane serves as an anode plane.

[4] A particle is called a minimum ionizing particle (or mip) when its mean energy loss rate in matter is close to the minimum. Most relativistic particles are considered mips.

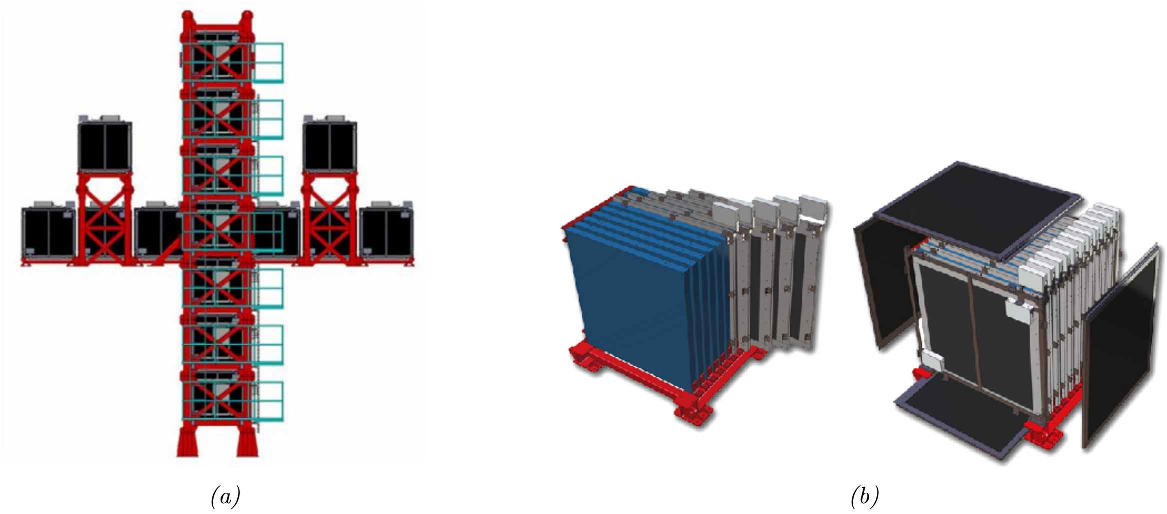
(a) *(b)*

Fig. 2.6: The INGRID detector. Figure (a): A general view of the INGRID detector. The cross-shaped layout with two additional off-axis modules on the horizontal arms of the cross. Figure (b): An INGRID module. Left: The sandwich structure of tracking planes (blue) and iron planes (grey). Right: The veto planes (black) on the outer part of the module. The figure is taken from Ref. [31].

The SMRD consists of 440 scintillator modules inserted in the air gaps between the steel plates of the UA1 magnet yokes. The UA1 magnet consists of 16 C-shaped yokes grouped in pairs to form a series of 8 consecutive rings. This magnet surrounds the inner detectors on four sides. The SMRD detects escaping muons flying at large angles to the beamline and measures their momenta. It triggers on through-going cosmic-ray muons and helps identify backgrounds from beam neutrino interactions in the surrounding cavity walls or the magnet.

INGRID

The on-axis INGRID detector monitors the neutrino beam direction and intensity on a daily basis. It consists of 14 identical 10 cm × 10 cm modules arranged in a cross of horizontal and vertical groups. The detector shape is symmetrical and centered on the beam axis. Two additional modules are placed outside of the main cross on top of the horizontal arms. Figure 2.6 displays the structure of the INGRID detector. All 14 modules have a sandwich-like structure of 9 iron plates and 11 tracking scintillator planes, which are surrounded by veto scintillator planes. The detector measures neutrino interactions on iron. The total target, i.e. iron, mass in each module is 7.1 tons. The veto planes reject interactions outside the module. The tracking planes consist of 24 horizontal and 24 vertical scintillator bars. The beam center is measured with precision better than 10 cm, which corresponds to 0.4-mrad precision at 280 meters downstream of the production target.

2.1.4 Far detector site

The interaction rates of the oscillated T2K neutrino beam are measured at the Super-Kamiokande facility. Besides serving as a far detector in T2K, SK is a stand-alone detector and experiment, where solar neutrinos [91], atmospheric neutrinos [92,93], and proton decay are studied [94]. SK is the world's largest Cherenkov detector. It is an underground cylindrical cavern filled with 50 ktons of pure water that is read by about 13,000 photomultipliers (PMTs). The Super-Kamiokande detector is shown in Fig. 2.7. It is divided into two volumes: a central inner detector (OD) and an outer detector (OD), that encloses the inner one. The ID is read out by more than 11,000 inward-facing PMTs. The inner wall of the OD is only sparsely instrumented with less than 2,000 outward-facing PMTs. The main purpose of the OD is to serve as a veto of cosmic-ray muons. Still, by looking for coincidence with the T2K beam, neutrino-induced events detected by the OD can be used as a signal.

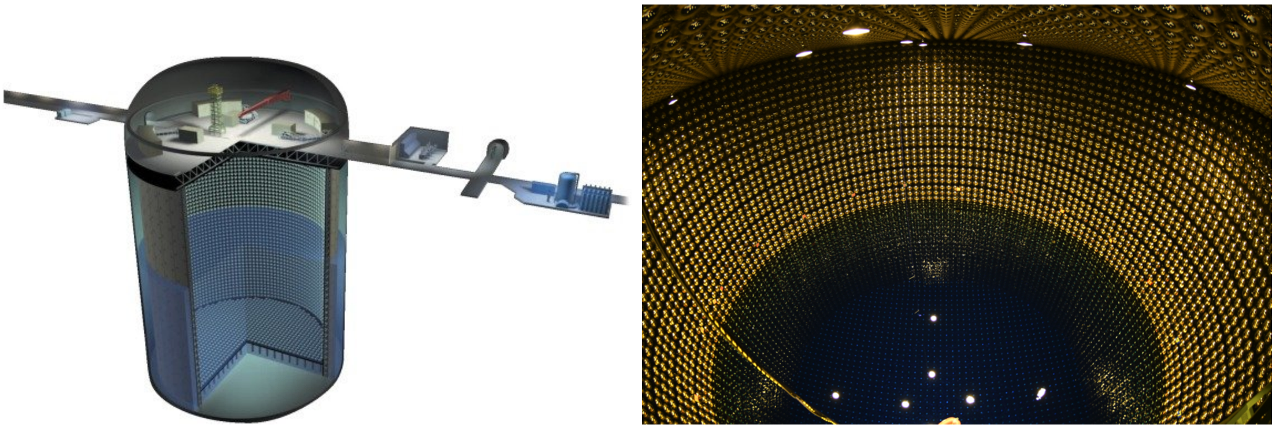

(a) (b)

Fig. 2.7: The Super-Kamiokande detector. Figure (a): The Super-Kamiokande detector with the surrounding facilities. A cut through the detector shows the inner and outer detectors, partially filled with water. The figure is from Ref. [95]. Figure (b): A look inside the inner detector, partially filled with water. The images is from the SK website [96].

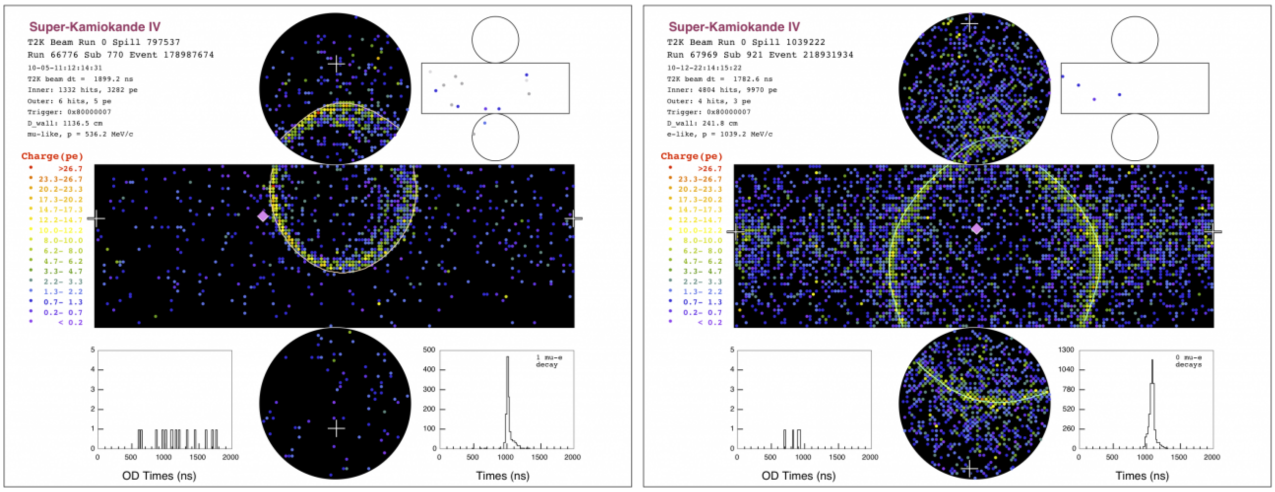

(a) (b)

Fig. 2.8: Event displays from the Super-Kamiokande detector. A muon-like (a) and an electron-like (b) event as seen by the Super-Kamiokande photomultipliers. The images are from the SK website [96].

The T2K far detector measures the flavour composition of the neutrino beam by counting charged current quasi-elastic (CCQE: $\nu_l + n \to l + p$; $l = \mu, e$) interactions of ν_μ and ν_e via detecting the produced leptons of their respective flavour. These charged leptons produce Cherenkov radiation in the water since their velocity is larger than the phase velocity of light in the same medium. The characteristic cone of Cherenkov light reaches the detecting walls and forms a ring-like structure of active PMTs. The shape of that ring is affected by the multiple Coulomb scattering that leptons undergo in the water. For the lighter particle, the electron, this effect is more pronounced than it is for the heavier muon. Consequently, the muon ring is much more clear and sharp than the electron one. The SK event reconstruction software uses this difference to identify muon- and electron-like particles. A typical display of the two types of rings is shown on Fig. 2.8. By counting these rings and identifying the particles that initiated them, it is possible to quantify ν_e appearance and ν_μ disappearance.

In August 2020, the SK collaboration reported completing of the first stage of gadolinium (Gd) loading in the the water of the Super-Kamiokande detector [96]. The achieved gadolinium concentration is 0.01%. It will be increased over the next few years to allow the detection of supernova relic neutrinos. When such neutrinos go through the SK, they interact in the water, mostly by inverse β-decay, and neutrons are produced. In the future, these neutrons would be captured by *Gd* to generate a gamma cascade. The gamma signal will be detected by the PMTs and manifest the first-ever observation of supernova relic neutrinos [97]. The addition of *Gd* is expected to improve the performance of the SK detector in all its research topics, including neutrino oscillations in the T2K beam.

2.1.5 Analysis strategy

Neutrino oscillations at T2K are probed by searching for ν_μ disappearance from the ν_μ beam and ν_e appearance in the ν_μ flux at the far detector. The measured signal rate at SK, denoted N^{obs}_{SK}, is compared to a prediction of that rate, N^{exp}_{SK}, to determine $sin^2 2\theta_{13}$ in ν_e appearance or $sin^2 2\theta_{23}$ and Δm^2_{32} in ν_μ disappearance. The expected event rate at SK, N^{exp}_{SK}, as a function of the reconstructed neutrino energy, E^{rec}_ν, is

$$\begin{aligned} N^{exp}_{SK}(E^{rec}_\nu) &= \int dE_\nu \Phi^{exp}_{SK}(E_\nu) \cdot P_{osc}(E_\nu) \cdot \sigma(E_\nu) \cdot \epsilon_{SK}(E_\nu) \cdot R_{SK}(E^{rec}_\nu, E_\nu) \\ &\quad \times M_{SK} \times POT, \end{aligned} \tag{2.2}$$

where Φ^{exp}_{SK} is the predicted flux at SK, P_{osc} is the oscillation probability, σ is the cross section of the neutrino-nucleus interaction, ϵ_{SK} is the SK detection efficiency, R_{SK} is the SK detector response function, which represents the probability to reconstruct the true neutrino energy, E_ν, as E^{rec}_ν, M_{SK} is the target mass of SK, and POT stands for number of protons on the target [98]. One of the main contributions to the systematic uncertainty in Eq. 2.2 comes from the precision of the Φ^{exp}_{SK} prediction[5]. This prediction is based on Monte Carlo. Moreover, it is difficult to obtain a precise neutrino flux prediction relying solely on simulations because of the underlying uncertainties of all physical processes involved in the neutrino beam generation. Notably model dependent is the hadron production in proton-nucleus interactions. A dedicated effort to constrain the T2K beam simulation with external hadron production data is discussed in Sec. 2.2.2.

Neutrino oscillation experiments, including T2K, perform near detector measurements of the neutrino flux, which are also employed to reduce the flux-related uncertainties. If one compares the measurements at the near and the far detector, correlated uncertainties will cancel. To achieve that, the relation between the fluxes at the two detector sites, that is the *far-to-near* ratio, has to be well defined. In T2K, a covariance matrix method is used for the task [98, 99]. The flux covariance matrix contains the flux uncertainties at SK and ND280 and the correlation between them. To use this method, the neutrino flux has to be predicted for each neutrino flavour at the far and near detectors in bins of neutrino energy. The near detector flux prediction is constrained by ND280 measurements. Then, the allowed region of the near detector prediction is extrapolated to the far detector using the estimated correlation in the covariance matrix. Further details of this procedure can be found in Ref. [98]. Its roots are with the near and far detector flux predictions made using the T2K beam simulation.

2.2 Neutrino flux prediction

The flux and energy spectrum of neutrinos at the T2K detectors (INGRID, ND280 and SK) are predicted with a full chain simulation of neutrino production. The simulation starts with the proton beam upstream of the baffle and ends with the decay of hadrons and muons to neutrinos. Then, a re-weighting procedure is applied to the hadronic interactions in each event to constrain the modeling of these processes. In the end, flux prediction uncertainties and the total uncertainty are estimated.

---

[5] Another key systematic uncertainty source is the neutrino-nucleus interaction model that gives the interaction cross section $\sigma(E_\nu)$.

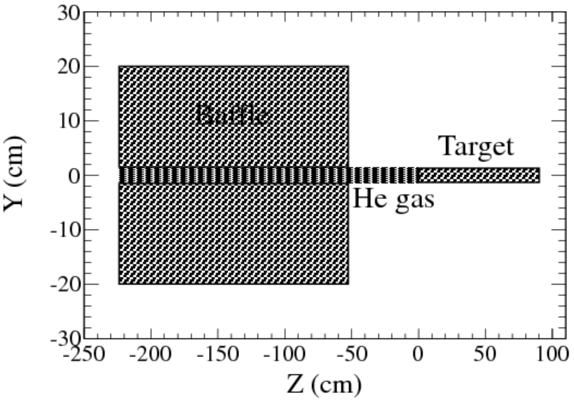

Fig. 2.9: A two-dimensional view of the baffle and target geometry set in the T2K Fluka *simulation. The figure is taken from Ref. [88].*

2.2.1 Beam simulation

The T2K beam simulation describes processes in the secondary beamline. It is important to have a full simulation of that beamline in order to model primary interactions and possible re-interactions of hadrons before they decay to neutrinos. The T2K beam Monte Carlo includes proton beam interactions inside the target and the baffle, secondary interactions in and outside the target, and tracking of particles until they re-interact, decay or kinetic energy drops below a pre-set threshold.

Interactions of beam protons in the thick graphite target, subsequent particle production, and target re-interactions are modeled using the Fluka generator [100–102]. This model is chosen since it is in best agreement with available hadron production measurements. The incident beam profile in the simulation is set based on the proton beam spatial distribution and divergence obtained from data. The initial kinetic energy of the beam protons is set to 30 GeV, which corresponds to 30.92 GeV/c momentum. The simulated target and baffle geometry is presented in Fig. 2.9. The baffle is described as a graphite block with a central cylindrical hole, which is 3 cm in diameter. The target is set as a 90-cm-long graphite rod with a 2.6-cm diameter of the base. Helium fills the volume along the beam axis both in the baffle and between the baffle and the target. All particles are traced until they escape the model geometry shown in Fig. 2.9. Information of particle properties at that exit point, such as particle type and kinetic variables, is recorded. In addition, full production chain of the particle is saved to the Fluka output.

Next is the J-PARC Neutrino Beam Simulation (JNUBEAM). JNUBEAM is a Geant3 [103] Monte Carlo that includes the baffle, target, horn magnets, helium vessel, decay volume, beam dump, and muon monitors. The geometry of the above-mentioned components is set according to the final mechanical drawings of the constructed beamline. The JNUBEAM simulation includes also the INGRID, ND280 and SK detectors, whose positions are given by survey measurements [88]. Hadronic out-of-target interactions in JNUBEAM are modeled by the GCALOR model [104]. The recorded particle information from the previous Fluka Monte Carlo is used as an input for JNUBEAM.

In this simulation step, particles are firstly tracked through the horn magnetic field, where they can interact with the horn material. Since the target station is placed inside the first horn, it is also included in the simulation. Next, particles are propagated through the decay volume, which is filled with helium, and the surrounding concrete shield that includes the beam dump. Tracking stops when particles decay or their kinetic energy falls below 10 MeV. The meson and lepton decays outlined in Tab. 2.1 are the ones considered in JNUBEAM as channels of neutrino production. The branching ratios are based on latest PDG data [44]. To lower computing time, all produced neutrinos are forced to point in the direction of SK or at a randomly chosen point in the near detector planes. This is done since ND280 and INGRID see the production target as a line, while the neutrino source is point-like for SK. To account for this trick, the actual probability of neutrino production in these two

Particle	Decay Products	Branching Ratio [%]
$\pi^{\pm}$	$\mu^{\pm}\nu_{\mu}(\bar{\nu}_{\mu})$	99.987
	$e^{\pm}\nu_{e}(\bar{\nu}_{e})$	0.0123
$K^{\pm}$	$\mu^{\pm}\nu_{\mu}(\bar{\nu}_{\mu})$	63.56
	$\pi^{0}e^{\pm}\nu_{e}(\bar{\nu}_{e})$	5.07
	$\pi^{0}\mu^{\pm}\nu_{\mu}(\bar{\nu}_{\mu})$	3.35
K_L^0	$\pi^{\pm}e^{\mp}\bar{\nu}_{e}(\nu_{e})$	40.55
	$\pi^{\pm}\mu^{\mp}\bar{\nu}_{\mu}(\nu_{\mu})$	27.04
$\mu^{\pm}$	$e^{\pm}\nu_{e}(\bar{\nu}_{e})\bar{\nu}_{\mu}(\nu_{\mu})$	100

Tab. 2.1: Decay channels and branching ratios for neutrino-yielding particles. Electron neutrinos, born in the decays of K_L^0 or the subsequent decays of muons, form a background to the muon neutrino beam. Branching ratios are taken from Ref. [44].

favored directions is calculated. It is then used to weight the corresponding event. This probability, the neutrino energy, flavour, and production history are saved as an output of JNUBEAM.

The following step in the prediction of the neutrino flux is re-weighting of the simulated hadron production processes using reference hadron production data.

2.2.2 Re-weighting method

In the T2K beam simulation, all interactions inside the target are modeled with FLUKA, while those outside of the target are handled by the GCALOR model. In order to constrain the output of these models, hadronic interactions in neutrino history are re-weighted using reference hadron production data. The re-weighting procedure scales the Monte Carlo predictions, of interaction rates and differential hadron production along the secondary beamline, to external data. Respectively, reference measurements include interaction cross sections and particle yields, which are obtained from thin- ($\sim$ 2 cm in length) and replica-target measurements. Thin target measurements account for single interactions, while replica target ones reflect the numerous interactions in the production target. As there are many re-interactions in the neutrino production chain, it is convenient to have a naming scheme of all particles involved in that process. In T2K, if hadrons originate from interactions of the primary beam protons, they are said to be secondary. Tertiary hadrons are those produced in interactions of hadrons other than the beam protons. Both secondary and tertiary hadrons can decay to neutrinos. Therefore, hadron production measurements are performed for protons at the initial beam momentum and for hadrons at lower momenta. The re-weighting procedure of the T2K flux prediction is largely based on the NA61/SHINE hadron production data. Other employed data samples can be found in [88]. The related NA61/SHINE measurements are described in detail in Chap. 3, Sec. 3.4. In the following paragraphs, the re-weighting of the output of the T2K beam simulation is outlined.

Differential hadron production re-weighting

Differential hadron production is re-weighted by means of differential multiplicities, $\frac{dn}{dp}(\theta, p_{in}, A)$,

$$\frac{dn}{dp}(\theta, p_{in}, A) = \frac{1}{\sigma_{\text{prod}}(p_{in}, A)} \frac{d\sigma}{dp}(\theta, p_{in}, A), \tag{2.3}$$

where p and θ are the momentum of the produced hadron and its angle relative to the incident particle (scattering angle), p_{in} is the incident particle momentum, A is the atomic number of the target nucleus, and σ_{prod} is the production cross section, which is defined as follows. In the classification of nuclear processes used in T2K, the production cross section governs the rate of interactions where hadrons are produced in the final state. The weight, $W(p_{in}, A)$, is calculated as the ratio between data and simulation

$$W(p_{in}, A) = \frac{\left[\frac{dn}{dp}(\theta, p_{in}, A)\right]_{data}}{\left[\frac{dn}{dp}(\theta, p_{in}, A)\right]_{MC}} \tag{2.4}$$

and is applied to all Monte Carlo interactions that produce hadrons. If the target material and the initial particle momentum match between the reference measurement and the simulation, the application of the weight in Eq. 2.4 is straightforward. When the initial particle momentum or the target material in data does not match the ones in Monte Carlo, the weights from Eq. 2.4 or data itself are scaled before the re-weighting is performed. If the phase-space coverage has to be extended, the BMPT parameterization is used [55]. More details about the T2K re-weighting procedure are available in Ref. [88]

Hadron interaction rate re-weighting

Only hadronic interactions in which new hadrons are produced, i.e. production processes, contribute to the neutrino flux. Consequently, the production interaction rate is re-weighted based on production cross-section measurements for hadrons of various types and energies on targets of different materials. The probability, $P(x; \sigma_{\text{prod}})$, that a particle interacts in the infinitesimal length Δx after travelling a distance x in a material of nuclear density ρ is

$$\begin{aligned} P(x; \sigma_{\text{prod}}) &= \int_{x}^{x+\Delta x} \sigma_{\text{prod}} \rho e^{-x' \sigma_{\text{prod}} \rho} dx' \\ &= \Delta x \sigma_{\text{prod}} \rho e^{-x \sigma_{\text{prod}} \rho}, \end{aligned} \tag{2.5}$$

where σ_{prod} is the production cross section. The probability that a particle goes through a given distance x in the material and does not interact is given by the survival probability, $P_{\text{surv}}(x; \sigma_{\text{prod}})$,

$$P_{\text{surv}}(x; \sigma_{\text{prod}}) = e^{-\rho \sigma_{\text{prod}} x}. \tag{2.6}$$

The weight applied to tune the interaction rate in simulation is given by the ratio of the interaction probabilities from data and Monte Carlo

$$W = \frac{P(x; \sigma'_{\text{prod}})}{P(x; \sigma_{\text{prod}})} = \frac{\sigma'_{\text{prod}}}{\sigma_{\text{prod}}} e^{-x(\sigma'_{\text{prod}} - \sigma_{\text{prod}})\rho}. \tag{2.7}$$

The distance Δx cancels out in Eq. 2.7. For particles that decay before interacting or do not interact going through a length x, the weight is

$$W = e^{-x(\sigma'_{\text{prod}} - \sigma_{\text{prod}})\rho}. \tag{2.8}$$

There is no dependence on the production cross section ratio in Eq. 2.8. A comparison between production cross-section measurements and the two models used in the T2K beam simulation, FLUKA and GCALOR, is given in Fig. 2.10. FLUKA is used to model interactions inside the target, while GCALOR models interactions out of the production target. Overall, FLUKA predictions are in good agreement with the data in a wide range of incident particle momenta. This is not the case for GCALOR, especially for interactions at low incident momenta. In view of that, the GCALOR production cross sections are actually re-weighted to the corresponding σ_{prod} prediction from FLUKA.

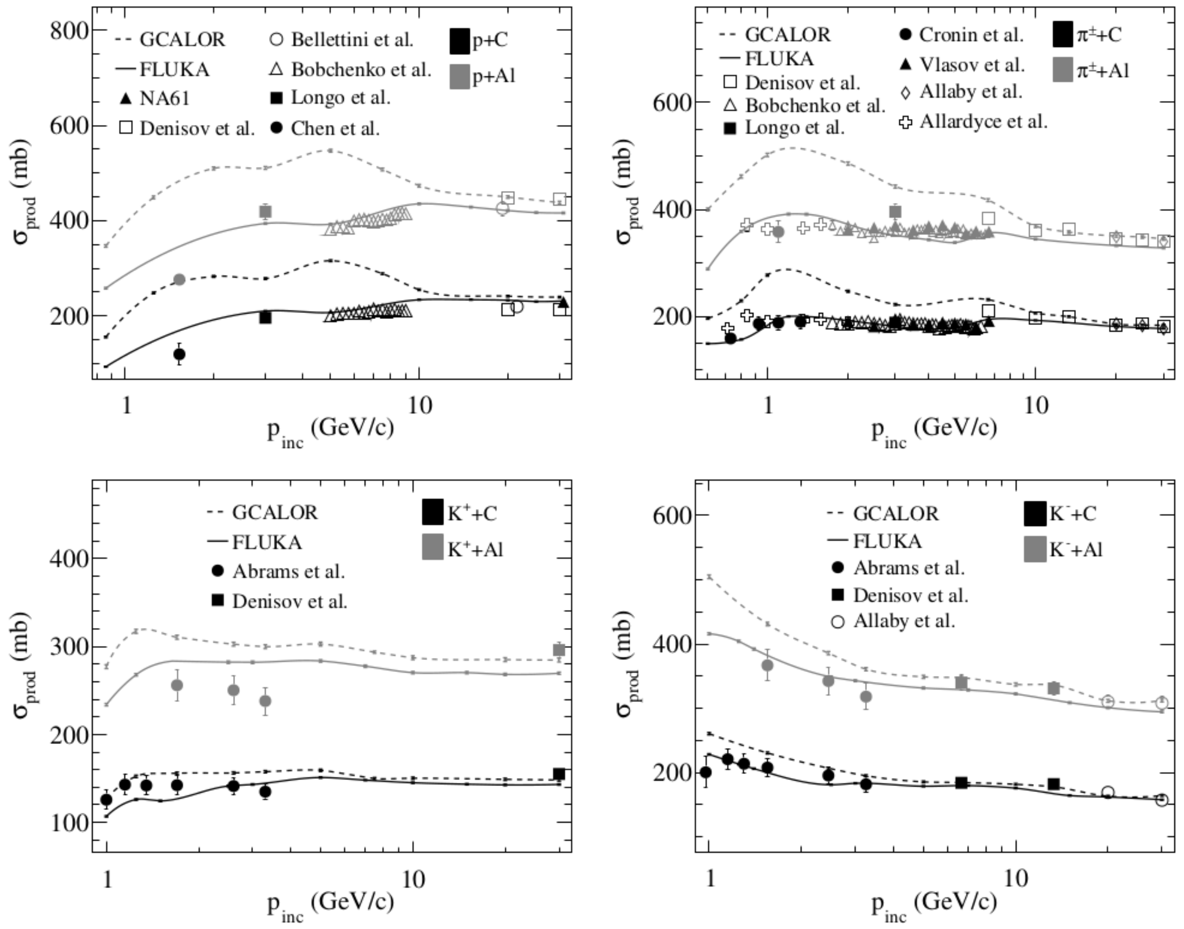

Fig. 2.10: Comparison of σ_{prod} measurements and Monte Carlo predictions for proton, kaon, and pion interactions on carbon (black) and aluminium (grey) at different incident particle momenta. The solid lines give the FLUKA *estimates and the dashed lines present the GCALOR prediction. The figure is taken from Ref. [88].*

flavour	ν_μ	$\bar{\nu}_\mu$	ν_e	$\bar{\nu}_e$
Fraction	0.9333	0.0617	0.0114	0.0017

Tab. 2.2: Flavour composition of the total SK flux in neutrino mode. The values in this table are based on data given in Ref. [88].

2.2.3 Predicted neutrino flux

Following the T2K beam simulation and the consequent re-weighting of hadron interactions in the neutrino production chain, the final T2K neutrino flux prediction is obtained for both the near and far detectors. This is the expected unoscillated neutrino flux. The predictions of the ν_μ and the ν_e fluxes at ND280 and Super-Kamiokande are shown in Fig. 2.11. The presented flux predictions are broken down by parent particle that decays to neutrino. For the ν_μ beam, at both detectors, neutrinos produced in pion decays dominate the low energy part of the spectrum, including the peak, while the bulk of high-energy neutrinos have kaon parents. A small fraction of low-energy muon neutrinos come from muon decays. The electron neutrinos are an irreducible background to the $\nu_\mu \to \nu_e$ oscillation studies. The high-energy part of the ν_e spectrum is once again populated by kaon decays. In the low-energy range, the majority of electron neutrinos come from muon decays, while kaon and pion parents contribute to a lesser extend. In addition, the fractions of different neutrino flavours in the SK flux prediction for neutrino mode, and after re-weighting is applied, are given in Tab. 2.2.

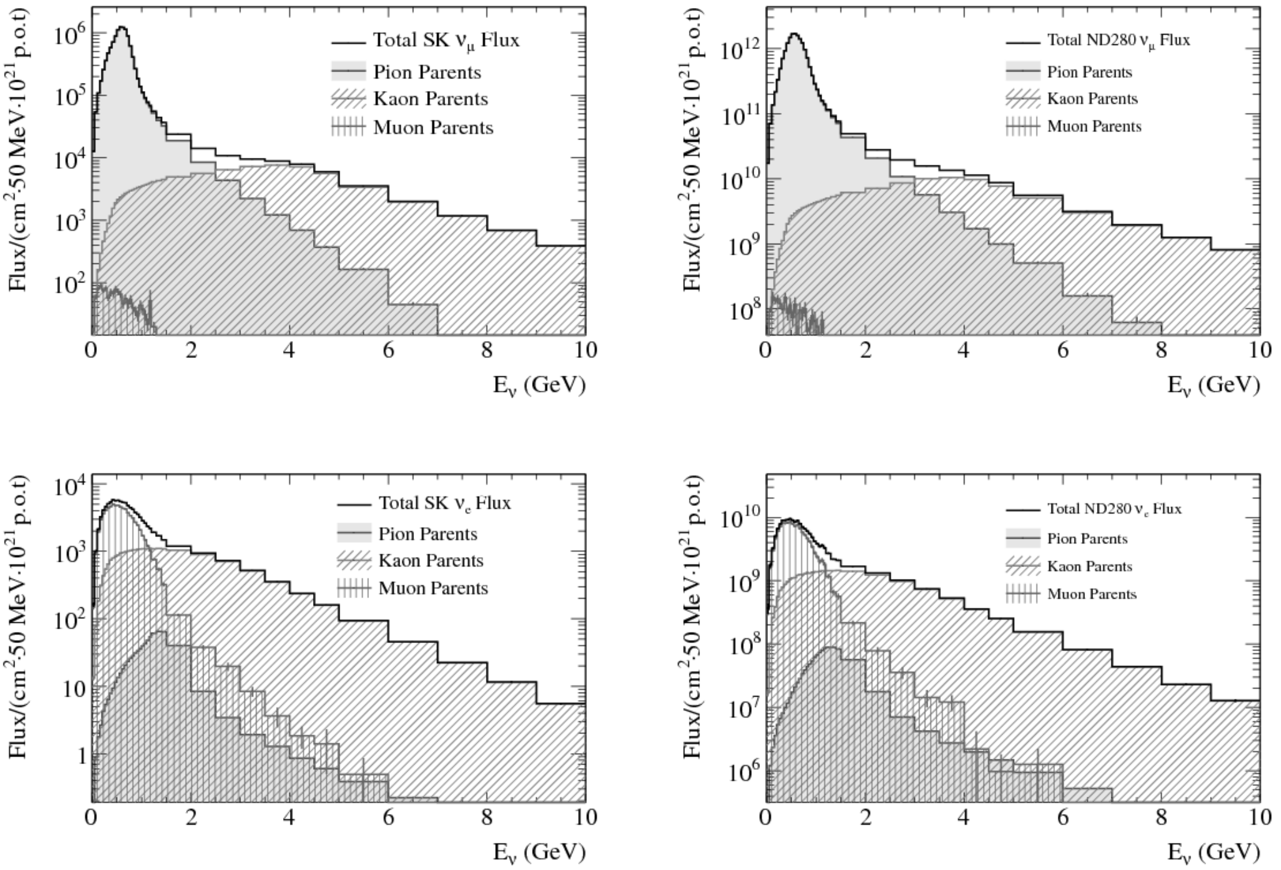

Fig. 2.11: The T2K ν_μ and ν_e neutrino flux predictions at the SK and ND280 detectors. Contributions from pion, kaon, and muon decays are overlaid on the plots. The error bars show MC statistical error. The figures are taken from Ref. [88].

2.2.4 Uncertainties of the flux prediction

The uncertainties of the neutrino flux prediction are related to proton beam properties, such as direction, spot size, and the number of protons on target, the target and horn alignment, the horn current and magnetic field, and the hadronic interactions in the beamline. The contribution of each of these factors to the total flux uncertainty is estimated by varying the corresponding simulation input parameter and evaluating the effect on the prediction by constructing a covariance matrix. This is discussed in detail in Refs. [88, 98, 99]. Then, the total uncertainty of the prediction is calculated as a sum of the covariances from independent uncertainty sources. In the following paragraphs, the major uncertainty sources of the T2K neutrino flux prediction are briefly described.

Proton beam and off-axis angle

The measured beam profile upstream of the baffle is used to generate the beam in Monte Carlo. The associated uncertainties of the position and angle of the beam center at the baffle front surface are used to evaluate the induced flux systematic uncertainty. Variations in beam position, divergence, and width mean that beam protons will go through different portions of target material, which in turn affects hadron production. The off-axis displacement of SK with respect to the beamline is largely in the vertical direction. Therefore, changes in the proton beam y position and width have an impact on the effective off-axis angle and so on the flux uncertainty. At the same time, changes in the horizontal plane have a negligible effect on the flux prediction. Additionally, the proton beam intensity measurement has a 2% precision and gives rise to a flux normalization uncertainty due to the normalization to the POT number.

The direction of the neutrino beam, which indicates the off-axis angle, is monitored by INGRID. To evaluate the systematic effect introduced by the off-axis determination, the energy and weight of each simulated neutrino is scaled to reflect possible shifts in the near and far detector positions. The corresponding uncertainty of the off-axis angle is about 0.44 mrad.

Target and horn alignment uncertainties

The systematic effect of the target alignment is studied by rotating the target in JNUBEAM in the horizontal and vertical planes. As for the horn alignment, both the horn positions and rotations are varied. Only the horn movements in the y direction and the vertical rotation of the first horn have a significant impact on the flux prediction. The fractional uncertainty due to the target and horn alignment is under 3% for neutrino energies below 7 GeV.

Horn current and magnetic field uncertainties

The uncertainties related to the horn current and the magnetic field are usually less than 2%. Their values are based on the uncertainties of the measured horn current and magnetic field strength, 1.3% and 2%, respectively.

Material modeling

In the beam simulation, the densities of all materials in the secondary beamline, including the target, are set to nominal values that have finite precision. This introduces a bias in the interaction probability and consequently the neutrino flux prediction. The corresponding uncertainty is below 2% at most neutrino energies.

Hadron production uncertainties

The leading uncertainty of the flux prediction is related to the modeling of hadronic interactions. In some reactions or certain ranges of phase space, Monte Carlo predictions for particle yields and interaction cross sections can be rather different from one another and data. Re-weighting with external hadron production data reduces this effect. Nevertheless, these data have measurement uncertainties of their own that get transferred to the flux prediction. Also, uncertainties arise from the scaling of the available data to different incident beam momenta, extrapolating it to other target materials, or extending particle yield data to uncovered phase space regions.

Pion and kaon decays generate the majority of neutrinos in the low- and high-energy part of the ν_μ beam energy spectrum, respectively. Thus, one can expect that the uncertainties coming from pion and kaon production re-weighting will affect the prediction below or above the peak. Furthermore, the interactions of secondary protons and neutrons contribute to 16% and 5% of the neutrino flux each. Consequently, their production is also constrained with external data and an uncertainty is assigned. Much like the secondary nucleons, secondary and tertiary pion interactions are also tuned and have a non-negligible contribution to the flux uncertainty, especially in the low-energy range.

There is also the uncertainty related to the total interaction rate of particles going through the various materials in the beamline. The estimate of this systematic effect is rather conservative because of the tension between cross-section results by different experimental groups. These groups typically report the production cross section, σ_{prod}, or the inelastic cross section, σ_{inel}. The later being the total cross section minus the elastic one. Then, the inelastic and the production cross sections are related via the quasi-elastic cross section, σ_{qe},

$$\sigma_{\text{prod}} = \sigma_{\text{inel}} - \sigma_{\text{qe}}. \tag{2.9}$$

In T2K, quasi-elastic processes are scatterings off of individual nuclei resulting in a single knock-out nucleon. Production cross-section measurements in $p + C$ reaction at different incident beam

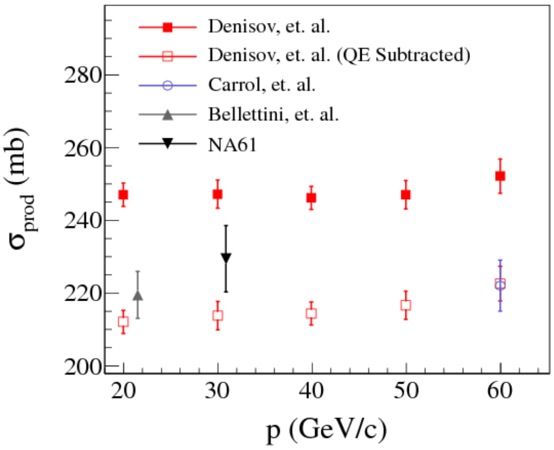

Fig. 2.12: Production cross-section measurements for protons on carbon for momenta in range 20-60 GeV/c. Data from NA61/SHINE [106], Bellettini et al. [82], Carrol et al. [83]. The data from Denisov et al. [84] are shown with and without the quasi-elastic cross section subtracted from the reported cross-section value. The figure is taken from Ref. [88].

momenta are shown in Fig. 2.12. There is an obvious disagreement between results, mainly between Denisov *et al.* data and others. The cross-section estimates by Denisov *et al.* in Ref. [84] are reported as "absorption" ones. It is not explicitly stated whether they include the quasi-elastic contribution or not. Therefore, it is unclear whether Denisov *et al.* measured inelastic or production cross section. If one subtracts the quasi-elastic contribution[6] from the results by Denisov *et al.*, a good agreement between all production cross-section results is found. Because of this ambiguity, the magnitude of the quasi-elastic cross section for a given reaction at a given incident beam momentum is taken as the systematic uncertainty of the corresponding production cross section. For proton interactions on carbon at 31 GeV/*c* incident beam momentum, the quasi-elastic cross section is around 30 mb.

Hadron production data are obtained from thin- and replica-target measurements. The thin-target data is used to constrain the Monte Carlo output in single interactions, such as interactions of secondary hadrons in the magnetic horns. Since the entire particle history is recorded, this can also be done for all interactions in the production target one-by-one. On the other hand, replica-target data re-weights at once the production chain of each particle emitted from the thick target. Thus, by weighting the particles exiting the target, one effectively weights the multiple interactions that take place inside.

Total flux uncertainty

The NA61/SHINE experiment carried out both thin- and replica-target hadron production measurements to help constrain the T2K flux prediction. The vast majority of the corresponding results are already implemented in the prediction. The output of the T2K beam simulation can be re-weighted using thin- or replica target-data separately to tune in-target interactions. This leads to two flux predictions. The ratio of the replica-tuned to the thin-tuned flux predictions is presented in Fig. 2.13. Overall, good agreement between the thin- and the replica-target predictions is found at all neutrino energies. However, around the T2K beam peak the replica-based flux prediction is about 5% lower compared to the thin-target constrained one. Investigation of the observed discrepancy is ongoing. It requires additional precise thin- and replica-target hadron production measurements.

Both thin- and replica-target data are typically used to constrain hadronic interactions in the beam simulation. A current estimate of the uncertainty of the ν_μ flux at Super-Kamiokande is

---

[6] There are different ways to determine the quasi-elastic cross section from theoretical models or available experimental data. For instance, in Ref. [105] the quasi-elastic cross section is derived using Glauber model calculations. Alternatively, in Ref. [82] Bellettini *et al.* introduced an empirical dependence allowing for quasi-elastic cross-section estimation. Currently, the EMPHATIC experiment has demonstrated capabilities of performing quasi-elastic hadron scattering measurements with uncertainties below 5%. Publication of such results is expected in the near future.

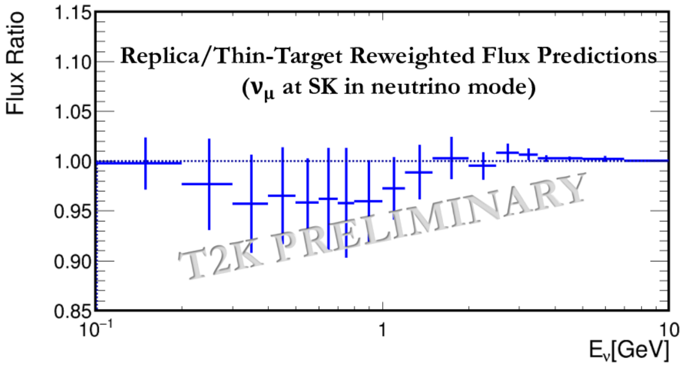

Fig. 2.13: Ratio of replica- and thin-target constrained T2K flux predictions. The vertical errors are calculated from the assigned production cross-section uncertainty. The figure is taken from Ref. [107].

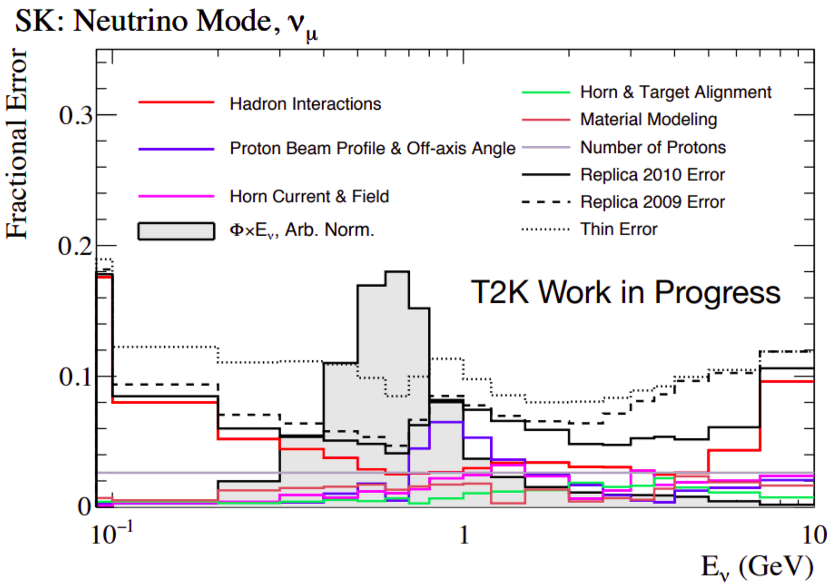

Fig. 2.14: Fractional uncertainty of the ν_μ flux at Super-Kamiokande. The contributions from different sources are given as lines of different colours. The grey area presents the normalized neutrino flux. Note the logarithmic scale on the x axis. The figure is taken from Ref. [77].

given in Fig. 2.14. A breakdown of the total uncertainty to different contributing sources is presented via coloured lines. The figure reflects two sets of thick-target data: pion yields off the T2K replica target extracted from the analysis of NA61/SHINE data from the year 2009 and pion, kaon, and proton yields off the same target obtained from the 2010 NA61/SHINE run. Since only pion production is constrained with the 2009 replica-target data, the effect of its implementation is most visible in the low energy region of the spectrum. Kaon production is tuned with the 2010 data and the corresponding effect is most visible for high-energy neutrinos. The flux uncertainty around the T2K beam peak is around 10% after implementation of all thin-target data and goes down to about 4% after the inclusion of the replica-target data, see Fig. 2.14. Actually, combining thin- and replica-target data in the re-weighting procedure, a sizeable reduction of the total uncertainty is observed in the whole neutrino energy range shown on the plot. However, in the very low (below the peak of 0.6 GeV) and very high (around 10 GeV) energy domains, more hadron production data is needed to lower the corresponding uncertainty due to hadronic interactions. In the future, the collaboration between T2K and NA61/SHINE will continue with additional thin- and replica-target hadron production measurements. The first of them is planned for the summer of 2021.

Chapter 3

The NA61/SHINE experiment

Contents

The NA61/SPS Heavy Ion and Neutrino Experiment (NA61/SHINE) is a fixed target experiment situated on a secondary beamline of the CERN's Super Proton Synchrotron (SPS). The experiment is a successor of the NA49 experiment [75]. NA61/SHINE has a rich physics program covering three different fields of research

- strong-interaction physics: search for the critical point of strongly interacting matter and study of the onset of deconfinement,
- cosmic-ray physics: hadron production measurements for improving modeling of cosmic-ray air-showers,
- neutrino physics: hadron production measurements for constraining neutrino beam simulations for the T2K and Fermilab neutrino experiments on the NuMI and LBNF beamlines: MINERνA [108], NOνA [33], and DUNE [46].

In this chapter, the NA61/SHINE detector is described, followed by an overview of the NA61/SHINE hadron production program for neutrino experiments.

3.1 The NA61/SHINE experimental setup

The NA61/SHINE large-acceptance detector is located on the H2 beamline in the CERN's North Area. The NA61/SHINE facility can receive both ion and proton beams from SPS, which are transported over the H2 beamline. The experiment can operate with targets of various materials and thickness.

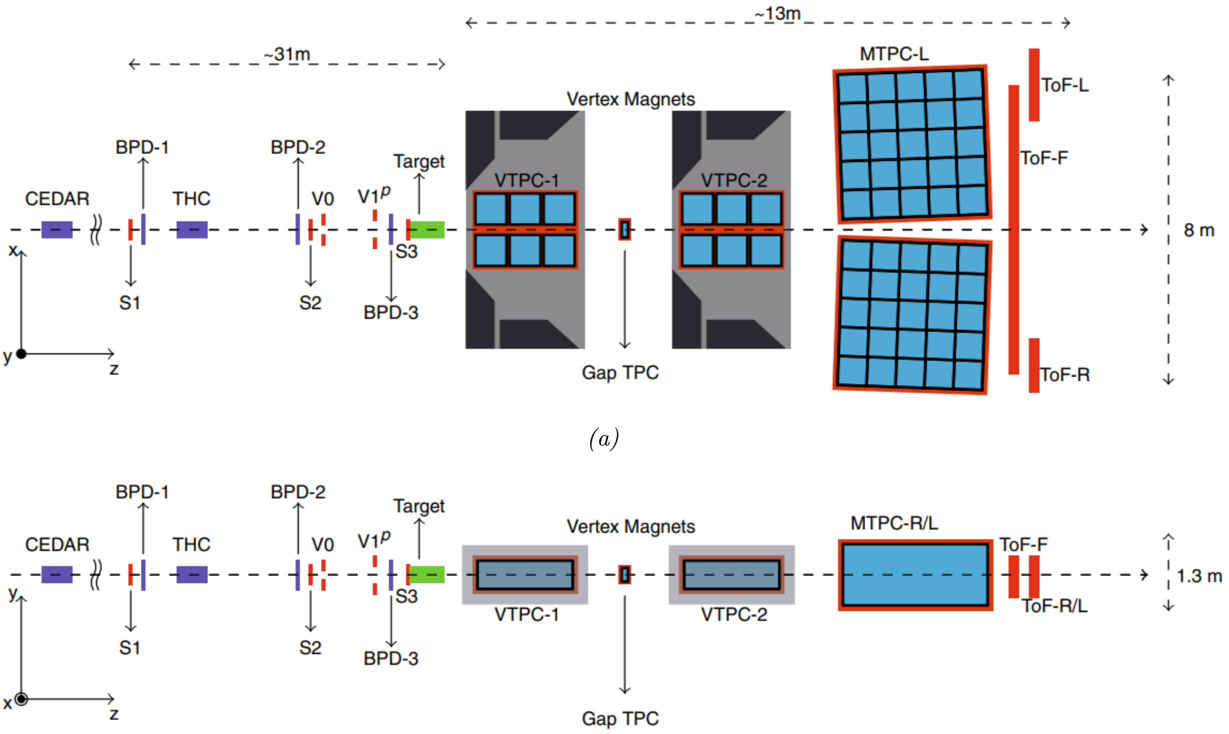

(a)

(b)

Fig. 3.1: Top (a) and side (b) view of the NA61/SHINE experimental setup during the 2010 T2K replica target data-taking. The orientation of the coordinate system is shown in the bottom-left corner. The beam is aligned with the z-axis and comes from the left.

At the NA61/SHINE spectrometer hadron-proton, hadron-nucleus, and nucleus-nucleus collisions are being studied by looking at the products of the respective interactions. The description of the NA61/SHINE spectrometer in this section is focused on the experimental setup back in the year 2010 run with a 31 GeV/c proton beam on a replica of the T2K target. The setup is presented in Fig. 3.1, where the experiment's coordinate system is shown in the lower left corner. The beam comes from the left and is aligned with the z axis. It passes through a set of scintillator and Cherenkov counters, whose signals are incorporated in the trigger system. The beam position in front of the target is measured by three multi-wire proportional chambers called Beam Position Detectors: BPD-1, 2, and 3. The NA61/SHINE experiment can facilitate thin targets with dimensions of a few centimeters and thick targets of meter-scale lengths, such as the 90-cm-long T2K production target. The T2K replica target is described in more detail in Section 3.4.1.

After the target, the properties of the produced particles are measured by five time projection chambers (TPCs). Two of them, Vertex TPC-1 and 2 denoted VTPC-1 and VTPC-2, are placed inside two superconducting dipole magnets: VTX-1 and VTX-2. Both VTPC-1 and VTPC-2 have one section on the left- and one on the right-hand side of the beamline forming a 24-cm-wide gap centered around the beam. A third TPC, the Gap TPC (GTPC), is standing between the two VTPCs and covers the forward region in the residual magnetic field. Further downstream of VTPC-2, on the left and right side of the beamline, are two large Main TPCs: MTPC-L and MTPC-R. Behind the MTPCs, scintillator walls serve as time of flight detectors: two side walls, TOF-Left (TOF-L) and TOF-Right (TOF-R), and a third TOF-Forward (TOF-F) wall. The NA61/SHINE hadron beamline and the above-mentioned detector components are described in more details in the following subsections. In addition, a comprehensive overview of the NA61/SHINE facility is available in Ref. [74].

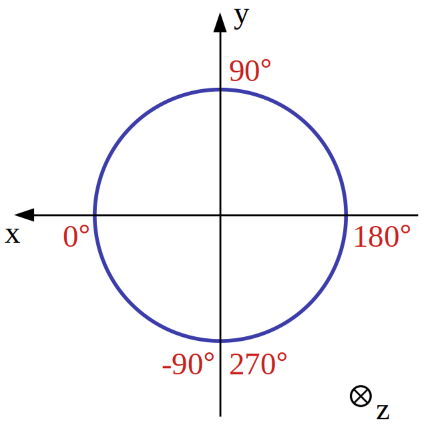

Fig. 3.2: Azimuthal angle definition in the NA61/SHINE coordinate system: $\phi = 0$ corresponds to the x axis and $\phi = \pi$ corresponds to the y axis.

3.1.1 The NA61/SHINE coordinate system

The standard detector coordinate system of the NA61/SHINE experiment is shown in Fig. 3.1 (bottom-left corner). Its origin is located on the beamline, in the center of the VTPC-2 chamber. The system is right-handed and the axes are oriented as follows. The z axis is horizontal and is aligned with the beamline. It adopts the beam direction. The x axis is also horizontal while being perpendicular to the z axis. The y axis is vertical and points upward. In this frame, the azimuthal angle, ϕ, is defined in the $x - y$ plane as

$$\phi \equiv atan \frac{p_y}{p_x}, \tag{3.1}$$

where p_x and p_y are the x and y components of the particle momentum. The sketch in Fig. 3.2 displays the value scheme of the azimuthal angle.

The polar angle, θ, is defined with respect to the beamline (z) and is

$$\theta \equiv asin \frac{p_T}{p}, \tag{3.2}$$

where $p_T = \sqrt{p_x^2 + p_y^2}$ is the transverse momentum and p is the total particle momentum. In addition, the scattering angle, θ_{scatt}, between an incoming beam track and an outgoing particle track is given by

$$\theta_{\text{scatt}} \equiv acos \left(\frac{\mathbf{p}_{\text{beam}} \cdot \mathbf{p}_{\text{track}}}{p_{\text{beam}}\ p_{\text{track}}} \right), \tag{3.3}$$

where p_{beam} is the beam momentum and p_{track} is the momentum of the outgoing particle. In the course of this thesis, the NA61/SHINE coordinate system and the presented angle definitions are employed.

3.1.2 Proton accelerator chain and the H2 beamline

The CERN accelerator complex that provides beams to the North Area is schematically presented in Fig. 3.3. The primary proton beam acceleration chain starts with the drift tube linear accelerator LINAC2. Protons in the beam originate from a bottle of hydrogen gas placed at one end of LINAC2. They are obtained from hydrogen atoms, when electrons are stripped off of atoms by an electric field. In LINAC2 the beam particles reach 50 MeV energy. Then, the beam is distributed to the four superimposed rings of the Proton Synchrotron Booster (PSB) and protons are accelerated to an energy of 1.4 GeV. Next, the particles in the four rings are recombined and sent to the Proton Synchrotron (PS). The PS has a circumference of 628 m and pushes particles to 25 GeV energy. These

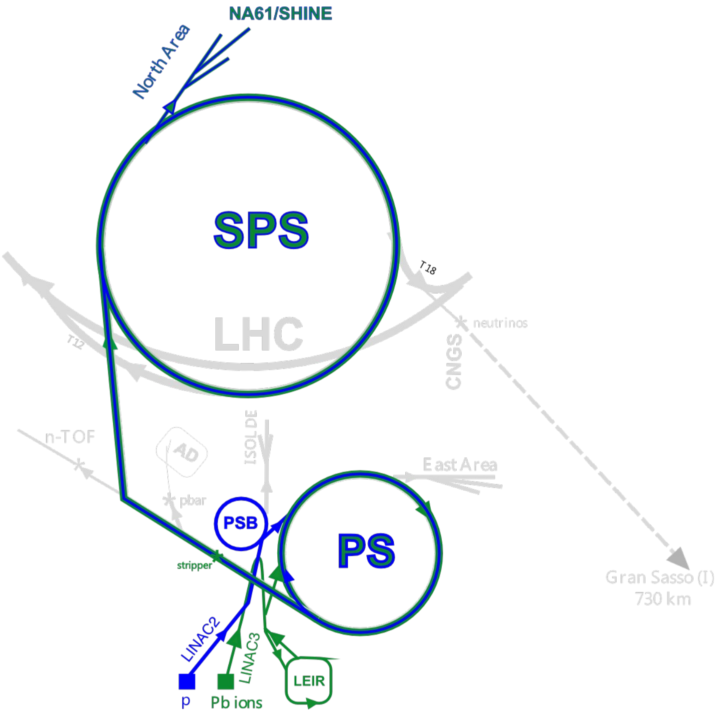

Fig. 3.3: The layout of the CERN accelerator chain that provides beams to the LHC and the North Area. The proton acceleration chain is shown in purple colour. The ion chain is given in green colour. The NA61/ SHINE detector can operate with both types of beams. The figure is taken from [74].

protons are later injected in the SPS. The SPS is 7 km in circumference and consequently two PS cycles are needed to fill it. In the SPS protons are accelerated up to 450 GeV. Then, they are send to the Large Hadron Collider (LHC) or the North Area, where the NA61/SHINE detector resides on the H2 beamline.

The SPS beam is transported over about 1 km and branched into three parts. Each of them is pointed at a primary target to produce secondary particles. By a set of upstream dipole magnets the incident angle of the primary beam to that target can be changed to modify the production angle of secondary particles. One of these targets, the T2 primary target, is the starting point of the H2 beamline. The NA61/SHINE detector is located 535 m upstream of it. The T2 target is 11 m underground for reasons of radiation safety. The vertical difference between the primary target and the experimental hall, which is at ground level, shields the experimental facilities from muons produced in primary beam interactions. The T2 target is a target station with several beryllium plates of different thickness. A plate is chosen with respect to the desired secondary beam type and momentum range. The H2 line can transport charged particles in momentum range from 9 GeV/c to 400 GeV/c. The transported hadron beams are of protons, kaons, or pions. Momentum selection is performed in the vertical plane by two large spectrometers that separate particles according to their rigidity, i.e. momentum to charge ratio. Each spectrometer consists of dipole magnets and collimators that deflect the beam and set its trajectory. Further beam definition is performed by the detectors of the NA61/SHINE trigger system.

3.1.3 Beamline detectors and trigger

For a given rigidity selection, the resulting beam is a mixture of the momentum-selected hadrons and also muons, electrons, and tertiary hadrons produced in interactions with the beamline material that all have similar momentum. A differential Cherenkov detector, the Cherenkov Differential Counter with Achromatic Ring Focus (CEDAR) [109], performs particle identification to separate these particle types. This counter is filled with gas that is nitrogen when the selected beam momentum is below 60 GeV/c, or helium for higher momenta. When a charged particle passes through the gas with

Counter	Dimensions [mm]	Hole [mm]	Position [m]
S1	60×60×5		-36.42
S2	ϕ=28×2		-14.42
S3	ϕ=26×5		-6.58
S4	ϕ=20×5		-2.11
S5	ϕ=20×5		9.80
V0	ϕ=80×10	ϕ=10	-14.16
$V0^P$	300×300×10	ϕ=20	≈-14
V1	100×100×10	ϕ=8	-6.72
$V1^P$	300×300×10	ϕ=20	-6.74

Tab. 3.1: List of the scintillator counters typically used during NA61/SHINE data-taking. The detectors' dimensions and position along the beamline is reported. Positions may vary in time due to dismounting and remounting in subsequent runs.

velocity higher than the velocity of light in that medium, Cherenkov photons are emitted at a certain angle, θ, given by

$$cos\theta = \frac{1}{n\beta}, \tag{3.4}$$

where n is the refractive index of the gas and $\beta = \frac{v}{c}$ is the velocity of the particle. It is important to note that the CEDAR is placed in a location of the beamline where beam divergence is negligible. The produced Cherenkov photons are transported and focused by an optical system onto a circular diaphragm of variable opening angle. The opening of the diaphragm is tuned so that Cherenkov photons emitted by particles of a given type would pass through the diaphragm. Behind the diaphragm, this light is detected by eight photomultipliers (PMTs). In NA61/SHINE, a 6-fold coincidence of PMT signals is used to tag the desired particle type. In addition, the pressure of the gas in the counter is adjusted to allow better separation between particles and improved precision of particle identification. Moreover, for beam momenta below 40 GeV/c, a Threshold Cherenkov detector (THC) located further downstream is used in anti-coincidence with the CEDAR to achieve higher beam purity. This detector is filled with carbon dioxide (CO_2) and is tuned so that particles of the desired type and velocity do no produce Cherenkov light. In the end, the momentum spread of the beam is below 1% and the number of misidentified particles is below 0.8%.

Besides selection of beam particle type and momentum, the tuned beam is directed towards the target by dipole magnets. A set of scintillator counters monitors and ensures the beam hits the NA61/SHINE target. Table 3.1 gives the relevant parameters and the position along the beamline of the scintillators usually used by NA61/SHINE. A few of the counters have central holes of a small diameter. These scintillators are used in anti-coincidence as veto counters and eliminate the beam halo.

The NA61/SHINE trigger system combines signals from the Cherenkov and scintillator counters along the beamline to categorize beam particles. For the proton beam on the T2K replica target data-taking four different triggers, T1-T4, were set and their definition is listed in Tab. 3.2. The T1, T2, and T3 triggers accept only beam protons. The T3 trigger selects a narrow beam profile since it features the V0 counter, which has a 0.8-cm central hole. The T4 trigger selects a wider beam profile and does not require particle identification.

The beam particles' trajectories are probed at three places upstream of the target by multi-wire proportional chambers called Beam Position Detectors (BPDs). The layout of a BPD detector is given in Fig. 3.4. The BPDs are operated with a Ar/CO_2 gas mixture. Each detector consists of two orthogonal sense wire planes that are sandwiched between three cathode planes. The outer cathode planes are sliced into 25-μm-wide strips with a 2 mm pitch. The position of every triggered beam particle in the transverse plane is measured on each of the two cathode planes of orthogonal strips, where charge is distributed on about 5 strips. A center-of-gravity method is used to calculate the beam

Trigger	Active counters
T1	S1 · S2 · $\overline{V_1^p}$ · CEDAR · $\overline{\text{THC}}$
T2	S1 · S2 · S3 · $\overline{V_1^p}$ · CEDAR · $\overline{\text{THC}}$
T3	S1 · S2 · $\overline{V_0}$ · $\overline{V_1^p}$ · CEDAR · $\overline{\text{THC}}$
T4	S1 · S2 · $\overline{V_1^p}$

Tab. 3.2: Set triggers for the 2010 T2K replica target run with the maximal magnetic filed.

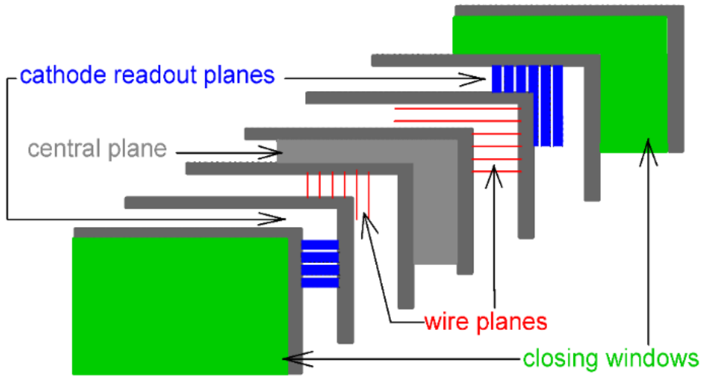

Fig. 3.4: Schematic layout of the BPD detector. Shown are the two orthogonal sense wire planes alternated with the three cathode planes.

particle position in each plane. A threshold on the signal amplitude is set to remove charge fluctuations. A 3D point is constructed by the two transverse coordinates. The precision of this position measurement is about 100 μm. It is usually required that the beam has position measurements in all 3 BPDs. Using this information, beam tracks are defined and can be extrapolated to the upstream target surface. The resulting precision of the beam position on the target front face is less than 200 μm for proton beams [75].

3.1.4 Time projection chambers

The tracking system of the NA61/SHINE spectrometer is based on time projection chambers (TPCs). These detectors allow measurements of both three-dimensional particle trajectories and energy deposit inside the chamber. Two of the NA61/SHINE TPCs, VTPC-1 and VTPC-2, are inside two superconducting dipole magnets, VTX-1 and VTX-2. Standing between the VTPCs, the forward GTPC is in the residual magnetic field. This field is uniform in the bigger part of the active volumes of the chambers and is aligned to the horizontal y axis. The maximal field generated by the VTX-1 magnet is 1.5 T, while VTX-2 creates a 1.1 T field. The resulting total bending power is 9 T m. This maximal field configuration is used with high-momentum incident beams and is scaled down for lower momenta to increase detector acceptance. The magnetic field bends charged particles into the TPCs and the fitting of their curved traces enables momentum and electric charge determination. The reported total momentum resolution is $dp/p^2 = 0.3 \times 10^4$ (GeV/c)$^{-1}$ for particles in range $4 - 100$ GeV/c. Two other large TPCs, MTPC-L and MTPC-R, are placed downstream of the magnets, symmetrically on the left and right of the beamline. They are outside of the magnetic field. These two detectors further extend the acceptance of the spectrometer and improve the energy loss measurement resolution. Parameters of the NA61/SHINE TPCs are given in Tab. 3.3.

The design and principle of operation of a TPC is presented in Fig. 3.5. Each TPC has an active volume surrounded by field-shaping electrodes, called field cage, and closed below by a cathode plate and above by a readout plane. The NA61/SHINE TPCs are filled with a gas mixture of Ar and CO_2. When a charged particle passes through the active volume, it ionizes the gas inside to produce electrons

	VTPC-1	VTPC-2	MTPC-L/R	GTPC
Size (L×W×H) [cm]	250×200×98	250×200×98	390×390×180	30×81.5×70
# of pads/TPC	26 886	27 648	63 360	672
Pad size [mm]	3.5×28(16)	3.5×28	3.6×40, 5.5×40	4×28
Drift length [cm]	66.60	66.60	111.74	58.97
Drift velocity [cm/μs]	1.4	1.4	2.3	1.3
Drift field [V/cm]	195	195	170	173
Drift voltage [kV]	13	13	19	10.2
Gas mixture	Ar/CO$_2$ (90/10)	Ar/CO$_2$ (90/10)	Ar/CO$_2$ (95/5)	Ar/CO$_2$ (90/10)
# of sectors	2×3	2×3	5×5	1
# of padrows	72	72	90	7
# of pads/padrow	192	192	192,128	96

Tab. 3.3: Parameters of the VTPCs, MTPCs and GTPC. The table is taken from Ref. [74].

and positive ions. A uniform vertical electric field is provided via a step-wise increase of the voltage supplied to the aluminized mylar strips that form the field cage. Guided by the electric field, all electrons drift with constant velocity towards the readout plane. The electron trajectory in the MTPCs is a straight vertical line. However, the VTPCs and the GTPC are placed in a magnetic field. By construction, the electric and magnetic fields are parallel to one another, both aligned to the y axis. In reality, distortions of the magnetic field exist close to the edges of the detectors due to the structure of the magnets. In these regions, the electrons no longer preserve straight drift paths but instead follow curved trajectories. This is the **E**×**B** effect. The drift velocity, v_D, in presence of electric, E, and magnetic, B, fields is derived from the Langevin equation [110] and is given by

$$\mathbf{v_D} = \frac{\mu}{1+\mu^2 B^2}\left(\mathbf{E} + \mu\mathbf{E}\times\mathbf{B} + \mu^2\mathbf{B}(\mathbf{E}\cdot\mathbf{B})\right), \tag{3.5}$$

where μ is the particle mobility. To derive Eq. 3.5, it is assumed v_D does not change in time. The mobility is given by $\mu = v_d/E$, where v_d is the drift velocity magnitude in absence of magnetic field. The electric field, E, and the drift velocity, v_d, are assumed to be constant in the active volume of the TPCs. Despite that, as the magnetic field changes inside the TPCs, v_D depends on the point in space. The change in the position, r, of drifting electrons with time, t, is

$$\mathbf{v_D}(\mathbf{r}) = \frac{d\mathbf{r}}{dt}. \tag{3.6}$$

Numerical integration of this differential equation gives the position of electrons during their drift in the TPCs.

Before reaching the readout plane, the number of electrons is increased. In the NA61/SHINE TPCs, Multi-Wire Proportional Chambers (MWPC) are used for this purpose. The amplification and readout regions of the TPCs are shown in Fig. 3.6. The MWPC consists of two parallel cathode planes and an anode sense wire plane in between. The readout volume is isolated from the drift space by another wire plane, called gating grid. The gating grid voltage supply is controlled by the trigger system. By adjusting the voltage setting, the gating grid "opens" for a short time to allow electrons in the readout volume and "closes" afterwards to block the slow positive gas ions. The gating grid, the cathode plane, and the sense wire plane comprise thin parallel wires. The cathode plane of the MWPC separates the drift volume with uniform electric field from the amplification region. The anode sense wires generate a high-gradient electric field that accelerates the drifting electrons. The latter collide with the gas atoms repeatedly to create an avalanche of electrons. This process is called gas amplification. The sense wire voltage is adjusted to guarantee proportional multiplication of electrons, whose number is increased by a factor of 10^4. These electrons are collected by the anode sense wire plane, while positive gas ions are repelled from it. The positive ions induce a signal pulse on the top cathode plane of the MWPC, which

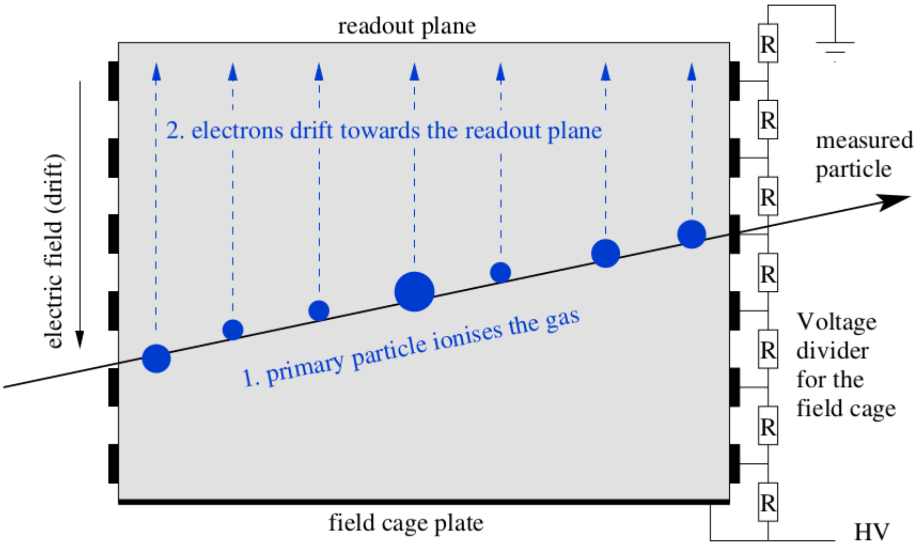

Fig. 3.5: Principle of operation of a TPC. The active volume is given in grey. The primary charged particle ionizes the gas to produce electrons. In presence of electric field, the electrons drift towards the readout plane on top of the chamber. The cathode plane is closing the volume from below. A series of strips on the sides of the volume form the field cage. A gradually changing voltage, applied to the strips, provides the uniform electric field. The figure is taken from Ref. [111].

is the readout plane. The latter is segmented into pads of about 1 cm^2 area to achieve high spacial resolution. Each pad position in the horizontal $x - z$ plane is known. To have a precise drift time estimate, during the acquisition time of the NA61/SHINE TPCs, which is about 50 μs, pad signals are read every 200 ns. These consecutive time intervals are called timeslices.

Pads are grouped along the x axis in rows called padrows. In a given padrow, following primary ionization, the produced charge is usually detected in several timeslices and distributed over a few pads. A weighted average over pad-timeslice pairs, called pixels, is calculated by assigning the deposited charge in each pixel as a weight. As a result, the arrival time of the signal and the x coordinate of its maximum over the padrow are determined. The position of the padrow along the beamline gives the corresponding z coordinate. Solving Eq. 3.5, the origin of the signal inside the chamber, called a cluster, is identified by its 3D position. The overall precision of this position measurement is about 200 μm for VTPCs and 210 μm for MTPCs [75]. Clusters are the building blocks of particle tracks. The number of clusters a track has is the number of padrows it crosses, given 100 % reconstruction efficiency. The total number of padrows in a TPC sets the maximum number of clusters a track can have in that TPC.

Besides their three-dimensional position, clusters are characterized by cluster charge. It is defined as the sum of all charges in all pad-timeslice pixels which form a given cluster. This charge is proportional to the energy an ionizing particle deposited in the gas, i.e. the energy loss of the particle. The energy loss measurement in the TPCs is based on a truncated mean calculation of the charge distributions of all clusters along a particle's trace. The method is called "truncated" as the lower 50% of the charge distribution is fitted with a Gaussian to define the mean energy loss of the track. The rest of the distribution is unused, truncated. Even though, distributions of energy loss are typically parameterized with the Landau distribution, a truncated method is used to reduce the impact of the fluctuations in the long upper-end tail. This procedure increases the resolution of particle identification based on the particle energy loss measurement. Usually, the energy loss is given by $\mathrm{d}E/\mathrm{d}x$ that is energy loss per unit length. The NA61/SHINE $\mathrm{d}E/\mathrm{d}x$ resolution is parameterized as $38\%/\sqrt{N}$, where N is the total number of clusters on a track [75]. A combination of energy loss and momentum measurements allow particle identification using the Bethe-Bloch formula [44].

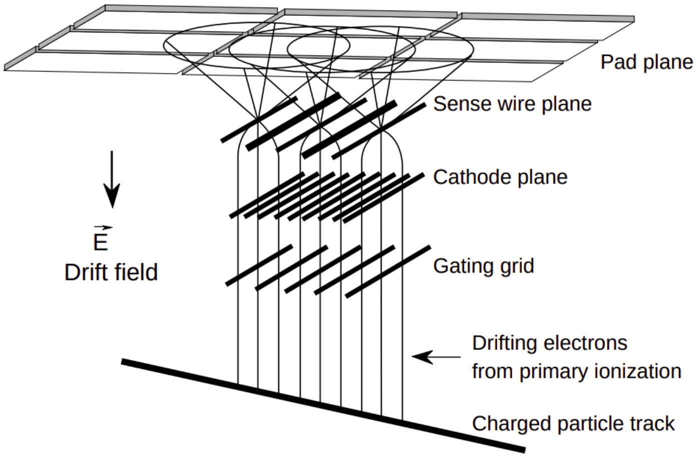

Fig. 3.6: A schematic picture of the charge amplification and registration regions in the NA61/SHINE TPCs. The figure is taken from Ref. [75].

3.1.5 Time of flight detectors

The NA61/SHINE spectrometer includes three time of flight detectors: forward TOF-F, left TOF-L, and right TOF-R. They perform time of flight measurements providing particle identification, which is complementary to the energy loss measurements of the TPCs. The TOF detectors are walls (arrays) of plastic scintillators placed behind the MTPCs. The TOF-L and TOF-R are positioned symmetrically around the beamline. They cover a selected portion of the high polar angle region that is relevant for the NA61/SHINE heavy-ion program. The forward-going particles are detected by the TOF-F wall. This detector is of great importance to the NA61/SHINE program of hadron production measurements and was constructed to facilitate such measurements for the T2K experiment. During the 2010 run with the T2K replica target, it consisted of 10 modules. Currently, this number is reduced due to the installation of additional TPCs in that forward region, see Sec. 3.1.6. A scheme of the TOF-F structure is given in Fig. 3.7. Every TOF-F module is an independent detector, which in turn consists of eight scintillator bars oriented vertically. The bars are placed in two rows in a zig-zag pattern with a 1-cm overlap between them. Each bar is made of a plastic scintillator that is wrapped with an aluminum foil. On top of that, the bars are covered by a black plastic foil. The dimensions of each bar are Width × Height × Length = 10 × 120 × 2.5 cm^3. Two PMTs are placed on the top and bottom of each bar. When a charged particle hits a particular bar, the produced light is reflected by the aluminum foil towards the two PMTs. The PMT signal marks the stop time of particle flight through the spectrometer. The corresponding start signal is provided by the S1 counter and is part of the trigger. The signal from each PMT is passed to a constant fraction discriminator (CFD), where it is divided to separate charge and time measurements. The mean value of these time measurements for the top and bottom PMTs of each bar is the timing reference of the stop signal, t_{stop}, and defines the arrival time of the particle:

$$t_{stop} = \frac{t_{PMTbottom} + t_{PMTtop}}{2}. \tag{3.7}$$

The time of flight, t_{TOF}, is

$$t_{TOF} = t_{stop} - t_{start}, \tag{3.8}$$

where t_{start} is the time measurement of the start S1 signal. In the end, the particle mass, m, is calculated from the measured time of flight, track length, l, and momentum, p, by

$$m^2 = \left(\frac{p}{c}\right)^2 \left[\frac{c^2 (t_{TOF})^2}{l^2} - 1\right]. \tag{3.9}$$

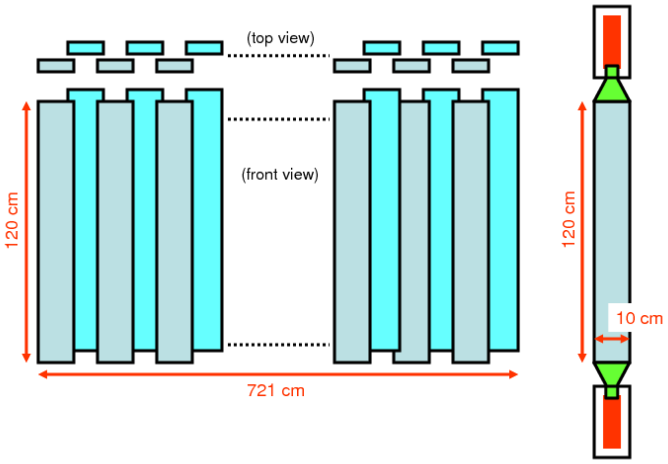

Fig. 3.7: The schematic layout of the scintillators building up the TOF-F detector. Two PMTs are glued to the top and bottom of each scintillator bar. The bars are placed in two rows in a zig-zag pattern with a 1-cm overlap between them.

The time of flight resolution of the TOF-F is about 110 ps [112]. The TOF-F detector is removed from the beamline for nucleus-nucleus measurements, where track density drastically increases. In that case, only the TOF-L and TOF-R are used as they have finer granularity.

3.1.6 Other detectors

Beside the sub-systems described in the previous few sections, the NA61/SHINE spectrometer has several other detectors. To facilitate centrality selection in nucleus-nucleus collisions, in the end of the NA61/SHINE beamline sits a Projectile Spectator Detector (PSD) [74]. It is a modular lead calorimeter that has 44 modules covering a transverse area of 120 × 120 cm^2. This calorimeter measures the energy of the projectile nucleons that did not interact in a collision. These nucleons are called spectators. The number of spectators is a measure of the centrality in a nucleus-nucleus collision. The PSD can extract this number with precision of one nucleon. Therefore, the PSD input is crucial for the study of the event-by-event fluctuations of multiplicity and forward energy, which are expected near the quark-gluon plasma transition. The PSD also serves as a beam dump.

For hadron-nucleus interactions, the collision centrality is deduced from the number of emitted low-momentum protons, which is measured by the Low Momentum Particle Detector (LMPD) [74]. This detector consists of two small TPCs on the two sides of the target that measure the ionization signal of radially emitted particles. In these TPCs, absorber layers are placed in the gas volume to help identify momentum cutoffs for protons that pass through the given layer. By measuring particle range and energy loss, it is possible to count the low-momentum protons in an event.

Direct measurements of D^0 meson production in heavy-ion collisions are facilitated by the Small Acceptance Vertex Detector (SAVD) [113]. It is designed to perform vertex reconstruction with about 70 μm accuracy. For the D^0 measurement, also called open charm measurement, the reconstructed vertex is the secondary vertex of the short-lived D^0 meson decaying to kaon and pion. The SAVD consists of two spectrometer arms composed each from four detector stations placed 5, 10, 15, and 20 cm downstream of the target. The stations are equipped with ultra-light 50 μm-thin silicon sensors of about 1.0×2 cm^2 active surface. These sensors have spatial resolution of 3.5 μm. The SAVD is a small-size version of a future detector, the Vertex Detector (VD), whose installation on the beamline is planned for after CERN's Long Shutdown 2 (LS2).

As mentioned in the previous Sec. 3.1.5, several TOF-F modules were removed when three additional forward TPCs, FTPC-1, FTPC-2, and FTPC-3, were installed in 2017. These TPCs perform tracking

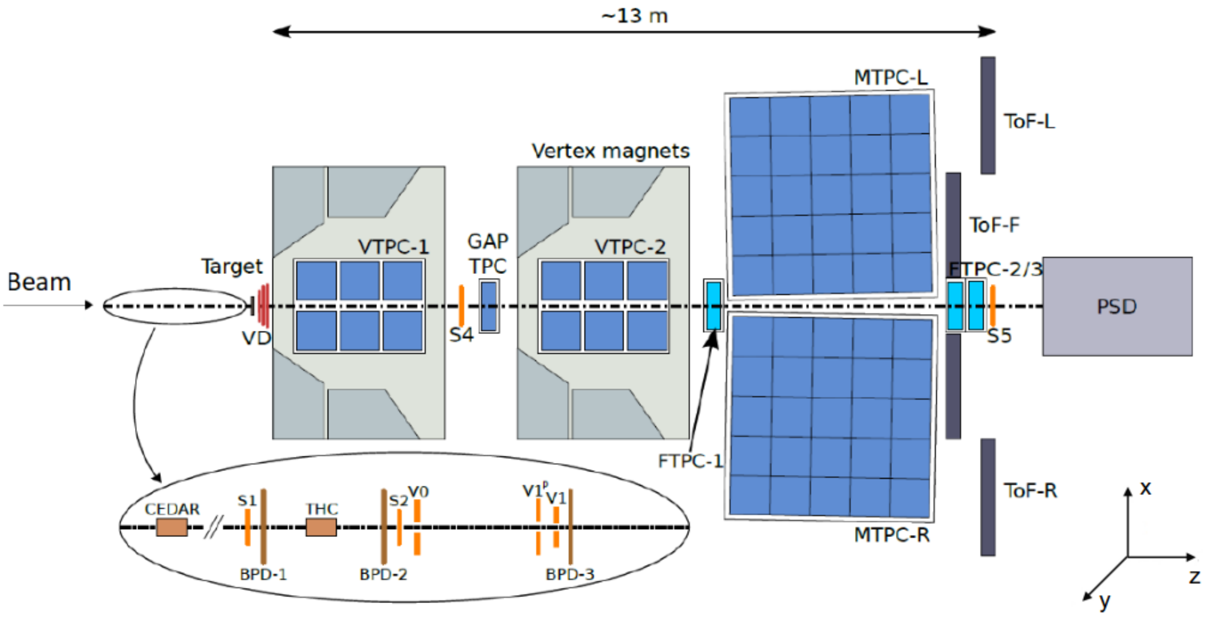

Fig. 3.8: The NA61/SHINE detector setup before Long Shutdown 2. Besides the detectors shown in Fig. 3.1, the FTPCs, PSD and Vertex Detector (VD) are displayed. The coordinate system is shown in the lower-right corner.

and energy loss measurements for forward-going particles, which are typically at or near the beam momentum. The three FTPCs have alternating drift field directions, which allows rejection of out-of-time background tracks, which are not associated with a primary interaction. This is referred to as tandem-TPC concept [114]. The layout of the NA61/SHINE spectrometer, including the FTPCs and other detectors described in this section, is presented in Fig. 3.8.

3.2 Data production

For each accepted trigger, the corresponding detector signals are stored in a single structure called an event. These signals are converted to particle trajectories and particle parameters are determined following reconstruction and calibration procedures. Dedicated software algorithms are used for this task. In the first years of NA61/SHINE operation, the collaboration adapted and used software products from the preceding NA49 experiment, referred to as Legacy software. Nowadays, it has been almost fully replaced by a new framework, called SHINE [115]. SHINE is based on the software of the Pierre Auger collaboration [116] and is written in C++. In addition to the SHINE-native modules, Legacy codes (clients) have been incorporated (wrapped) into the SHINE framework to form the so called Wrapped Legacy reconstruction chain. The data collected in 2010 with a proton beam on the T2K replica target, that is the focus of this work, was reconstructed via the Legacy software. The Legacy reconstruction chain performs the following tasks:

1. BPD reconstruction
2. cluster finding in the TPCs
3. correction of cluster positions for various effects, including $\mathbf{E}\times\mathbf{B}$
4. local track finding
5. global track finding
6. momentum determination

7. main interaction vertex fit
8. redo momentum fit with vertex constraint
9. calculation of the maximum number of clusters per track, i.e. potential point calculation
10. matching of TOF hits with tracks
11. V^0 and Ξ finder

This consecutive set of steps is repeated for each event. The reconstruction of beam tracks in the BPDs is independent of the reconstruction of traces in the TPCs. The BPD information is later used to determine the main interaction vertex in the target. To construct TPC tracks, first clusters are built based on the collected charge in the pad-timeslice pixels, as described in Sec. 3.1.4. After clusterization, corrections are applied to account for known effects that distort cluster position, e.g. $\mathbf{E}\times\mathbf{B}$ electron drift. Still, additional residual corrections resulting from data calibration are typically applied to account for other unidentified effects. From reconstructed clusters in a given TPC, tracks in that TPC are built. Those are called local tracks. In the MTPCs, clusters are fit with straight lines to form a local track. In the VTPCs and the GTPC, where the magnetic field is non-zero, a magnetic field tracker builds curved local tracks. Afterwards, local tracks are merged between TPCs to form global tracks. Once connected, each global track is fitted again and important parameters are determined, including particle charge, momentum, and energy loss. Next, the main vertex is determined. For T2K replica target measurements, this is done by extrapolating global TPC tracks towards the BPD track until the minimal distance of approach is reached. With the obtained main vertex, TPC tracks are refitted with a vertex constraint. Two types of global tracks are kept on output. One is the TPC global track before adding the main vertex to the fit and is called a *track*. The other is the global track fitted with the vertex constraint and is called a *vertex track*. In the analysis of T2K replica target data, only *tracks* are used because multiple re-interactions in the 90-cm-long target complicate main vertex reconstruction. The reconstruction chain continues with the estimation of the number of padrows that a track crossed. This gives the maximum number of clusters a track could have, which are called potential points. Then, signals (hits) in the TOF detectors are matched to existing global tracks. Finally, out-of-target re-interactions and weak decays are sought for by searching for vertices outside the target. Two finders look for weak decays in the beamline: the V^0 and Ξ finder. The former searches for decays in which two particles of opposite charge are produced. These can be decays of Λ or K^0_s. The Ξ finder looks for Ξ decays, e.g. $\Xi^- \to \pi^- + \Lambda$, which are indicated by a kink in the original track.

Several iterations of the reconstruction chain are needed to obtain all necessary calibration constants. The calibration procedure provides numerous crucial parameters for the proper reconstruction of events. Most of these parameters are specific for a given data-taking period and reflect time-dependent quantities, such as drift velocity. The NA61/SHINE data calibration comprises several steps that result in more accurate knowledge of detector geometry, drift velocity in each TPC, cluster positions (through residual corrections), magnetic field, time of flight, and energy loss measurements. Details of the calibration procedure can be found in Ref. [117]. The reconstruction chain and many calibration constants are also used in the simulations of target interactions and subsequent detector response to the passage of produced particles.

3.3 Monte Carlo production

Similarly to other high-energy experiments, the NA61/SHINE measurements of particle interaction properties are checked against models of different Monte Carlo (MC) generators. For this purpose, various MC techniques are used to simulate the detector response and a procedure to match simulated tracks to their reconstructed counterparts is developed. The Monte Carlo is used to correct the data for effects related to detector geometry and response, reconstruction algorithm inefficiency, and out-of-target interactions. It is also employed in estimation of systematic uncertainties. The simulation procedure comprises the following steps:

1. simulation of interactions inside the target
2. propagation of the produced particles from the target surface through the NA61/SHINE spectrometer, which may include secondary interactions, particle decays, and other processes
3. simulation of detector response, which includes procedures leading from known hit positions to digitized charge in pad-timeslice pixels
4. track reconstruction based on the simulated detector signal and matching of simulated tracks to reconstructed ones.

During the MC production, parameters such as drift velocity, target position, and detector positions are taken from data calibration.

Simulations employed in the analysis described in this work were carried out using two software realizations, namely

- Legacy MC chain: Legacy simulation and Legacy reconstruction chains
- SHINE simulation and Wrapped Legacy reconstruction chains

In the first case, FLUKA 2011 [100–102] is used to generate particle interactions inside the target, GEANT3/ GCALOR [103, 104] model describes interactions outside the replica, and GEANT3 is used for particle transport through the spectrometer. This MC production matches the T2K neutrino beam simulation in use of simulation frameworks, see Chap. 2, Sec. 2.2.4. For the SHINE simulation, GEANT4 package [118–120] is used for both in-target and out-of-target interactions and also particle propagation. In each case, the simulation does not include detectors situated before the target. Actually, the beam source is placed at the BPD-3 position. The set beam properties are based on those of accepted data triggers. The FLUKA 2011 input includes two histograms of the beam divergence dependence on x and y beam coordinates at the BPD-3 position along the beamline. For SHINE MC, a ROOT [121] file containing BPD data is added to other input files.

In both MC chains, simulation of TOF signals is not performed. Instead, each particle that hits the TOF-F is assigned a *TOF* mass with resolution based on the data. As TOF signals are not simulated, TOF-F efficiency cannot be corrected with Monte Carlo.

The reconstruction chain used in the MC productions is similar to the one described in the previous Sec. 3.2, except there are no BPD tracks to be reconstructed in MC, and no residual corrections are applied. The reasons residual corrections are excluded from the MC chain are that the target and detector geometries are perfectly known, all implemented procedures are well-established, and simulated physics effects are well understood. Consequently, there are no unidentified distortions in the detector response that would need to be corrected.

After simulated events are reconstructed, for each reconstructed track, a matching procedure finds the simulated one having the largest number of MC points that are geometrically close to the track's reconstructed clusters. After completion of this step, one has a handle to compare simulated input to reconstructed output. For the Legacy MC chain, the output files are converted to the file format used within the SHINE framework, called SHOE, to unify subsequent analysis.

3.4 Hadron production measurements program for neutrino experiments

The NA61/SHINE experiment performs dedicated hadron production measurements that are utilized to constrain interaction rates and particle production in the neutrino beam simulations of the T2K and the Fermilab neutrino experiments on the NuMI and LBNF beamlines. Before proceeding further, it is

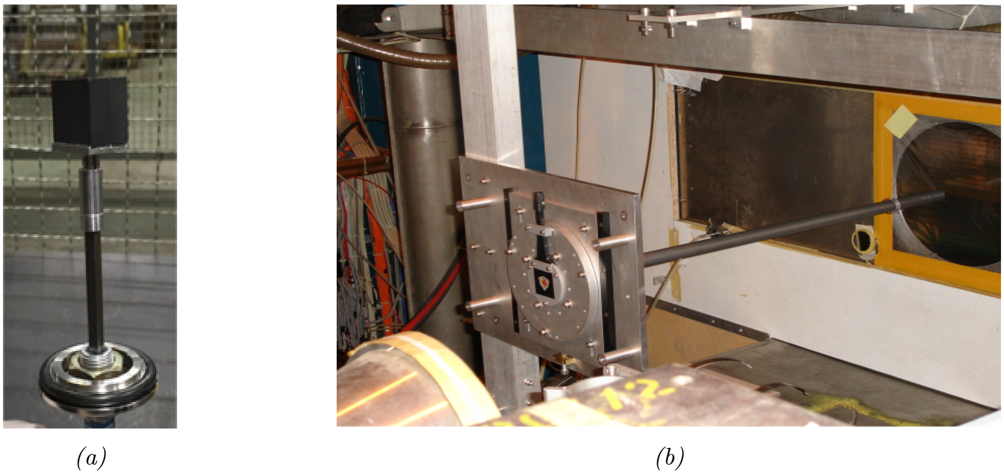
(a) (b)

Fig. 3.9: Photos of the thin (a) and replica (b) targets. The thin target is placed in the target holder. The T2K replica target is shown installed on the beamline without the BPD-3.

important to outline the definitions of nuclear interactions employed by the NA61/SHINE collaboration. This classification is based on the type of particles produced in the process. An elastic process, that is, coherent nuclear elastic scattering, is one where no new particles are produced. Except for coherent nuclear scattering, all other processes due to the strong interaction are labeled as inelastic. Furthermore, the inelastic interactions are subdivided into two groups: quasi-elastic and production processes. Quasi-elastic processes result in the fragmentation of the target nucleus. In production interactions, new hadrons are produced. The probability for each of these three processes is governed by the corresponding cross section and the total cross section, σ_{tot}, is:

$$\sigma_{\text{tot}} = \sigma_{\text{el}} + \sigma_{\text{inel}}, \tag{3.10}$$

where σ_{el} is the elastic cross section and σ_{inel} is the inelastic cross section, which is a sum of the quasi-elastic and the production cross sections, respectively σ_{qe} and σ_{prod}:

$$\sigma_{\text{inel}} = \sigma_{\text{qe}} + \sigma_{\text{prod}}. \tag{3.11}$$

These definitions agree with the ones used in the T2K experiment.

In the following sections, an overview of the NA61/SHINE data-taking and analysis campaign for the T2K experiment will be given. The targets used in the measurements will be presented, followed by a summary of the corresponding run periods, and a discussion of obtained results.

3.4.1 Targets

NA61/SHINE hadron production measurements relevant for T2K were performed using a 31 GeV/c secondary proton beam and two targets: a 2-cm-thin carbon target and a 90-cm-long T2K replica target. A view of the two targets is given in Fig. 3.9. Technical characteristics of the thin and extended targets are outlined in Tab. 3.4. The density of the T2K replica is about 1.5% higher compared to the density of the T2K target. This is considered an intrinsic effect of their manufacturing [122]. Moreover, the observed difference is about the size of the density measurement uncertainty.

A replica of the graphite core of the T2K target is installed on the NA61/SHINE beamline, without its cooling system or casing. To position the replica target, it had to be mounted on a target holder. For this purpose, the target has a flange at its upstream end. This flange has an inner graphite part and an outer aluminum shell that encloses the inner part. On the outside of the flange is a hole, where the S3 scintillator is placed and the BPD-3 is mounted on top. A plastic ring tied to a thin plastic thread is put at the target downstream end to fix its position. This solution minimizes material budget between the target surface and the NA61/SHINE detectors.

Target	Thin	T2K replica
Material	graphite	graphite
Density [g/cm^3]	1.84 ± 0.03	1.83 ± 0.03
Length [cm]	2	90
Cross-section shape	square	round
Cross-section dimensions	2.5 × 2.5 cm^2	$\oslash$ =2.6 cm
Interaction length [λ_I]	0.04	1.9

Tab. 3.4: Technical characteristics of the thin and the T2K replica targets.

Beam	Target	Year	Magnetic Field [GeV/c]	Triggers [10^6]	Results
protons at 31 GeV/*c*	thin	2007	20	0.7	$\pi^\pm, K^+, K^0_s, \Lambda$ multiplicities and σ_{prod} [106, 123, 124]
	replica	2007	20	0.2	*proof-of-principle* of replica target measurements [125]
	thin	2009	20	5.4	$\pi^\pm, K^\pm, p, K^0_s, \Lambda$ multiplicities and σ_{prod} [126]
	replica	2009	20	2.8	$\pi^\pm$ yields on target surface [127]
	replica	2010	20	9	$\pi^\pm, K^\pm, p$ yields on target surface [128]
	replica	2010	160	1.2	σ_{prod} (this thesis and [129])

Tab. 3.5: List of the NA61/SHINE hadron production measurements for the T2K experiment.

3.4.2 Data-taking periods

The NA61/SHINE experiment collected hadron production data for T2K during the runs in years 2007, 2009, and 2010. These measurements are summarised in Tab. 3.5. Primary hadron interactions in the target were studied using the thin carbon target. All interactions inside the T2K target were examined using the T2K replica target. The data collected in 2007 were used to establish the calibration and analysis procedures. Furthermore, the 2007 thin-target results were actually used in the T2K neutrino flux simulation and lowered the hadron production uncertainty to below 15% near the flux peak [57]. The 2009 measurements had increased statistics compared to those in 2007. The 2009 data were also incorporated in the T2K flux prediction and had an impressive impact leading to a total uncertainty of about 5%, see Fig. 2.14. During the summer of 2010, NA61/SHINE took data with the T2K replica target using magnetic field configurations of 1.2 T m or 9 T m bending power. The former setting is denoted "low" magnetic field. The corresponding dataset was used to measure hadron yields from the surface of the T2K replica target. In between the low magnetic field runs, the dipole magnets were operated at their maximal 9 T m bending power. This setting is denoted as a "maximum" or "high" magnetic field. It allowed for better detection of beam protons that scattered elastically or quasi-elastically in the target and passed through it. Analysis of the maximum magnetic field dataset is the subject of this thesis.

3.4.3 Discussion of results

In NA61/SHINE, particle production is measured with both thin and extended targets. As mentioned before, thin target measurements are used to constrain single interactions, in this case primary $p + C$ interactions at 31 GeV/*c* incident beam momenta. On the other hand, replica target particle production data is used to re-weight particle emission from the whole target surface, providing a handle on all interactions inside the thick target. In thin target analyses, hadron production is calculated in the phase space of momentum and polar angle, (p, θ). The results are presented as double differential

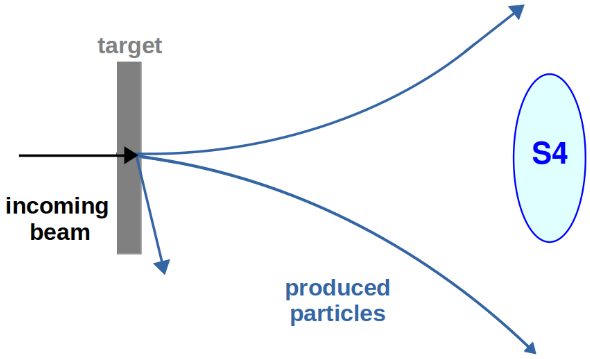

Fig. 3.10: A schematic of a production interaction where produced hadrons miss the S4 counter.

multiplicities, $\frac{d^2n}{dpd\theta}$, which are estimated as the double differential cross section, $\frac{d^2\sigma_h}{dpd\theta}$, normalized by the total production cross section:

$$\frac{d^2n}{dpd\theta} = \frac{1}{\sigma_{\text{prod}}} \frac{d^2\sigma_h}{dpd\theta}. \tag{3.12}$$

In the case of replica-target measurements, the data is given in terms of momentum, polar angle, and also longitudinal z position on the target surface (p, θ, z). The T2K beam simulations showed absolute neutrino fluxes are sensitive to the position along the beamline, where the neutrino parent particles exited the production target. The shape of the computed neutrino spectrum is dependent on the number of target z bins, but the beam peak position is not. At least 5 longitudinal bins are needed in order to satisfy the T2K physics requirements on the precision of the ν_μ beam at the far detector. For this reason, in the analyses of replica-target data, the target is fragmented to 6 longitudinal target bins: 5 equidistant bins of 18 cm each while the 6^{th} bin is the downstream end of the target. The statistics of the thick-target data collected in 2009 was sufficient to estimate only $\pi^\pm$ production. The larger 2010 dataset was used to extract $\pi^\pm$ and also $K^\pm$ and p yields on the replica surface. It is worth noting that the forward acceptance of the NA61/SHINE detector, prior installation of the FTPCs in 2017, with the low magnetic field configuration was insufficient to measure forward going high-momentum particles. However, more importantly, particle production measurements with this magnetic field setting cover most of the phase space of relevance to the T2K beam simulation. The NA61/SHINE replica-target data, excluding the maximum field data, is now incorporated in the T2K flux prediction and has helped considerably lower the total uncertainty to about 4% at the beam peak energy, see Fig. 2.14. In 2021, the NA61/SHINE collaboration plans to have an additional T2K replica target run. The goal is to collect more data needed to constrain high-energy charged kaon production and reduce the neutrino flux uncertainty in range 5-10 GeV/c [77].

The NA61/SHINE production cross-section measurements are used to constrain the interaction rate of protons in carbon at 31 GeV/c incident beam momenta. The production cross section can be extracted from thin- and replica-target data. In the thin-target case, the analysis approach is based on the kinematics, essentially geometry, of a production interaction. It is expected that in such interactions the produced particles will miss the S4 counter, see schematic in Fig. 3.10. The S4 detector is a round scintillator of a 2 cm diameter placed on the beamline between the two vertex magnets as per Fig. 3.8. The directly measured quantity is not the production cross section but a so-called *trigger* cross section. Besides contributions from production events, the trigger cross section includes a small fraction of elastically and quasi-elastically scattered particles that do hit S4. Also, production events with outgoing tracks that hit the S4 counter will be removed from the selected sample. In order to obtain the desired σ_{prod}, the trigger cross section is corrected for the above-mentioned effects by applying

Monte Carlo correction factors. In the end, the NA61/SHINE thin target production cross-section estimates for 2007 and 2009 data are

$$2007: \ \sigma_{\text{prod}} = 229.3 \pm 1.9(\text{stat}) \ \pm 9.0(\text{sys})\,\text{mb}, \tag{3.13}$$

$$2009: \ \sigma_{\text{prod}} = 230.7 \pm 2.8(\text{stat}) \ \pm 1.2(\text{det}) \ {}^{+6.3}_{-3.5}(\text{mod})\,\text{mb}. \tag{3.14}$$

Variation of the size of the S4 counter is included in these estimates as a source of systematic uncertainty. The 2009 data shows an improvement in the precision of the production cross-section estimate compared to the 2007 result. The main source of systematic uncertainty for the 2009 cross-section measurement is the model dependence.

The production cross section can be directly obtained from replica target measurements by means of beam attenuation in the thick graphite target. This method minimizes model dependence of the end result. In the replica-target case, the selection procedure is based on the energy transfer in elastic and quasi-elastic interactions and not the kinematics of the processes since multiple interactions take place inside the target. The production cross-section analysis of the 2010 replica target data at maximum magnetic field is described in detail in the following chapters.

Chapter 4

Validation of the data and Monte Carlo samples

Contents

Software modules for analysis and custom calibration tasks of the T2K replica target data have already been developed for the analysis of the 2010 low magnetic field replica target data. They are compatible with the SHINE framework and are further adapted to the analysis of the 2010 maximum magnetic field replica target data. Before proceeding to any calculations, tests are carried out to identify any deficiencies in event reconstruction. In this chapter, performed cross-checks for both data and Monte Carlo productions are briefly discussed.

4.1 Data reconstruction aspects

4.1.1 Track extrapolation to the target surface

The data of interest was collected with the maximal magnetic field setting of the NA61/SHINE detector. In the past, dedicated measurements of the magnetic field in the detector area had been carried out and a magnetic field map was created [75]. It has been used for track reconstruction ever since and is stored in the database. The map fully covers the sensitive volumes of VTPCs and GTPC. The field measurements were done in 8-cm steps in all directions. In between the measured points, linear interpolation is applied. The map spans an area of about 16.5 m^3 but does not cover the whole replica target region. The magnetic field is aligned with the y axis and consequently the B_y component is the largest one. In Fig. 4.1 the B_y component of the magnetic field is shown in the $x - z$ plane at $y = 0$ cm and the $y - z$ plane at $x = 0$ cm. The empty areas on both plots emphasize the limited coverage of the map in the region of the replica target.

In the analysis of the p + T2K replica target data, it is important to obtain the exit point of created particles on the target surface. For this purpose, TPC tracks are extrapolated backwards to the target surface. Hence, the magnetic field map has to be extended to cover the whole target area. This is done by fitting an exponential function to the tail of the magnetic field and using its parameters to calculate the field outside the map. The same approach was used for the low magnetic field data analysis. For the full magnetic field case, the same function is used, but the fit parameters are recalculated. An example of the field extrapolation along the beamline for $x = 0$ cm and $y = 0$ cm is given in Fig. 4.2. Details about the mathematical equations modeling the track extrapolation to

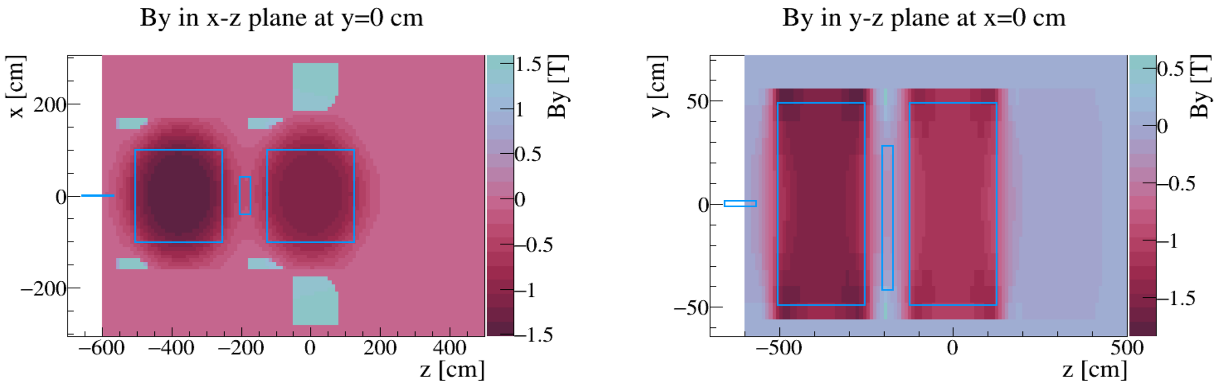

(a) *(b)*

Fig. 4.1: Magnetic field B_y component in $x - z$ plane at $y = 0$ cm (a) and the $y - z$ plane at $x = 0$ cm (b). Rectangles overlaid on the plots show the target, VTPC-1, GTPC, and VTPC-2. The detector markers on the figure include nonsensitive volumes as well. The available magnetic field map does not cover the full replica-target region.

the target surface can be found in Ref. [112]. The procedure accounts for multiple Coulomb scattering in the air between the TPCs and the target. The extrapolation continues until the track hits the target or distance of closest approach is reached. Therefore, it is essential that the target position is precisely determined. Target position calibration was again carried out for the low magnetic field analysis, and the calibration procedure is given in Ref. [112]. The obtained target upstream position, target tilt, and their uncertainties are given in Tab. 4.1. The (x, y) position of the target center is given with respect to the BPDs or the TPCs. The difference is indicative of the BPD-TPC alignment. The values from Tab. 4.1 are adopted for the current analysis as the maximum-magnetic field data was collected in between low-magnetic field runs.

	wrt BPDs		wrt TPCs				
	x [cm]	y [cm]	x [cm]	y [cm]	z [cm]	t_x [mrad]	t_y [mrad]
Value	0.01	0.28	0.15	0.12	-657.5	0.0	0.0
Uncertainty	0.01	0.01	0.03	0.02	0.1	0.3	0.3

Tab. 4.1: Target upstream position and target tilt in the NA61/SHINE coordinate system (see Fig. 3.1) and their uncertainties [112, 128]. The target tilt is a measure of the longitudinal alignment of the target to the nominal beam direction (the z axis) and is given separately for the $x - z$ plane (t_x) and the $y - z$ plane (t_y).

4.1.2 ExB electron drift

Electron drift in the TPCs in presence of an external magnetic field is subject to the $\mathbf{E} \times \mathbf{B}$ effect, see Chap. 3, Sec. 3.1.4. It distorts electron trajectories inside the active volumes of the TPCs, as shown on the schematic in Fig. 4.3. Instead of a straight vertical drift, electrons follow a path of some curvature, which leads to a shifted reconstructed cluster position with respect to the primary ionization. The size of this distortion for the x, y, and z coordinates of the clusters is given in Fig. 4.4. The effect is the strongest around the edges of the TPCs, close to the magnet yokes, where the desired alignment of the magnetic field cannot be preserved. The shifts in cluster positions can be of the order of a few centimeter. The size of the shifts scale with the magnitude of the magnetic field and this effect is less pronounced for the low magnetic field replica target data. In order to account for the $\mathbf{E}\times\mathbf{B}$ electron drift, Runge-Kutta methods are used to solve the differential equation in Eq. 3.6 and reconstruct cluster positions. The classic 4^{th} order Runge-Kutta method is implemented in the Legacy framework, while a 5^{th} order one is used in SHINE.

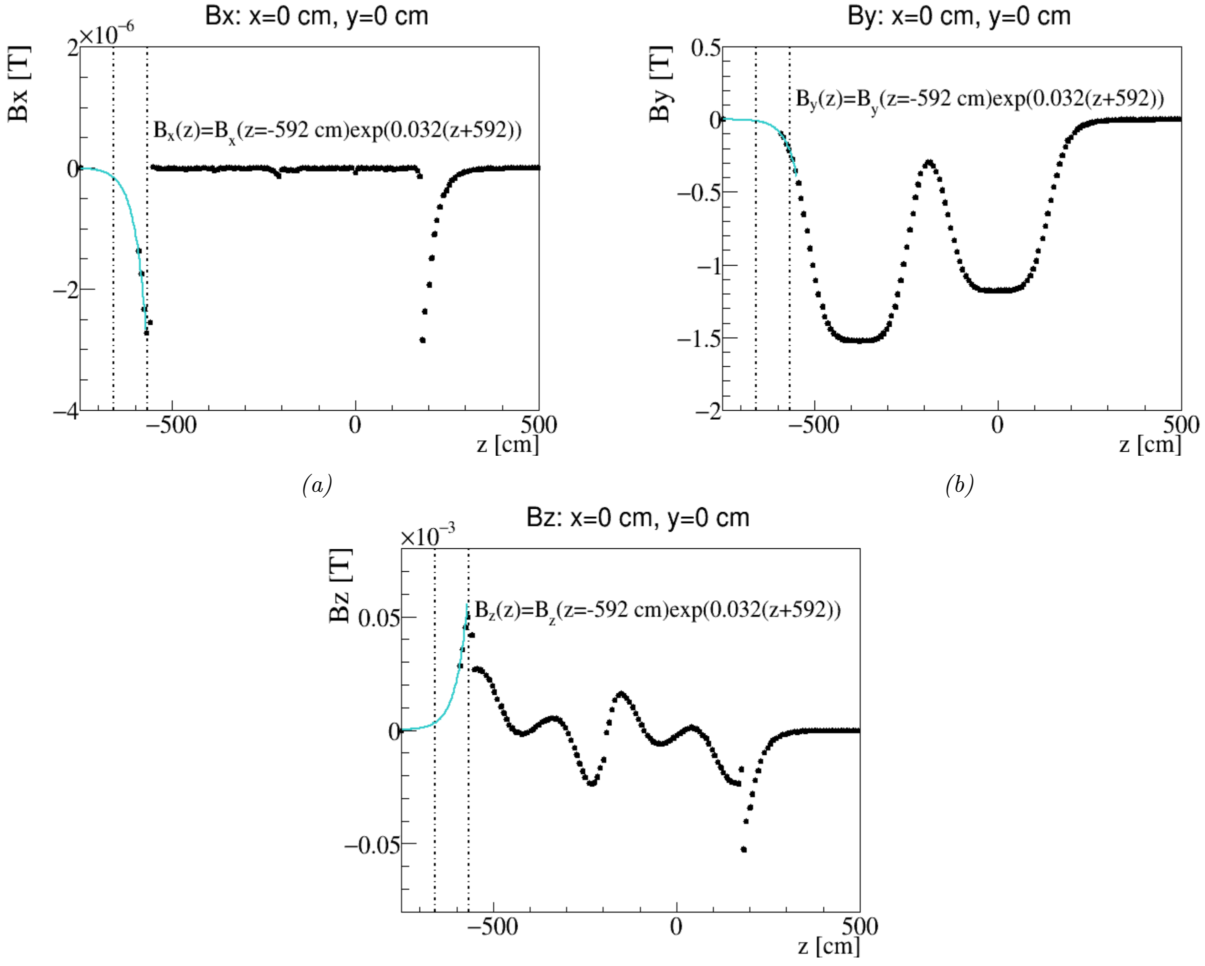

(a) *(b)*

(c)

Fig. 4.2: Extrapolation of the magnetic field B_x (a), B_y (b), and B_z (c) components outside of the field map. The extrapolation is done along the beamline for coordinates $x = 0$ cm and $y = 0$ cm. The dashed lines indicate the target boundaries in z direction.

After accounting for known effects and running data production, the latter is validated by a final test, which comprises the following. For small sub-volumes (*voxels*) of the TPCs, for all reconstructed clusters and tracks in that volume, the mean of the differences between a reconstructed cluster position and the reconstructed parent track's coordinates at the cluster's z coordinate is calculated. For all voxels, The obtained mean differences, also called *residuals*, in x and y direction are shown in Fig. 4.5. The colour scale is given on the plot and is ±0.2 cm. The lack of any rapid, periodic, or build-up effects in the calculated residuals indicates satisfactory performance of the data calibration and reconstruction.

4.2 Quality assurance of reconstruction procedures and Monte Carlo

Monte Carlo productions are examined to verify the consistency between generated and reconstructed parameters. This is done by performing two types of checks. First, it is confirmed that the reconstruction algorithm provides reliable results of cluster finding and building, called *clusterization*, and momentum determination. It is straightforward to check these by looking at the differences between the generated and the reconstructed track parameters. The reconstruction software fits particle momentum at the first reconstructed cluster on the particle's track. For this reason, parameters are compared at that point. The corresponding plots are given in Fig. 4.6. Overall, good agreement between generated and reconstructed track properties is found with no significant deviations.

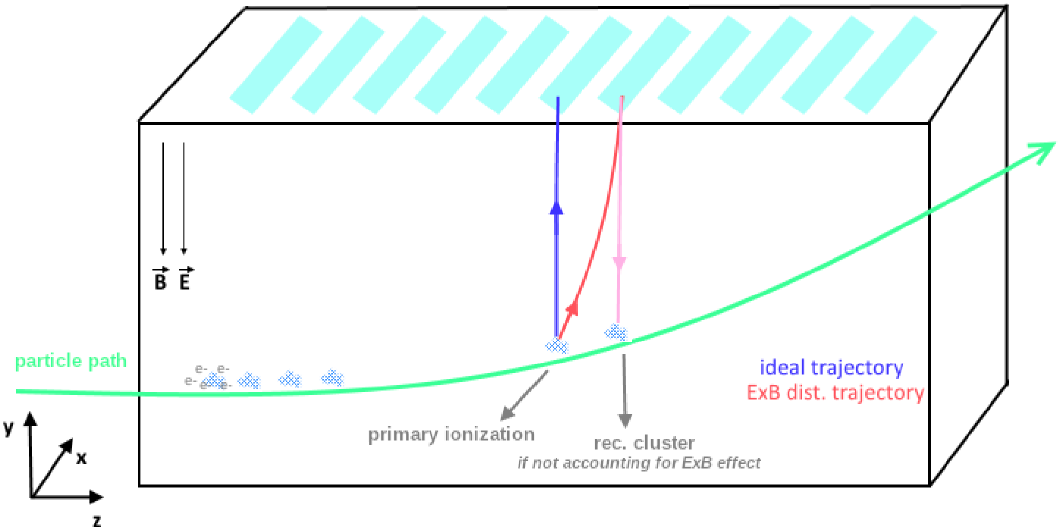

*Fig. 4.3: A schematic of the **ExB** effect on the electron drift inside a detector under electric, E and magnetic, B, fields. By construction the two fields are parallel to one another. In reality, this is not always the case.*

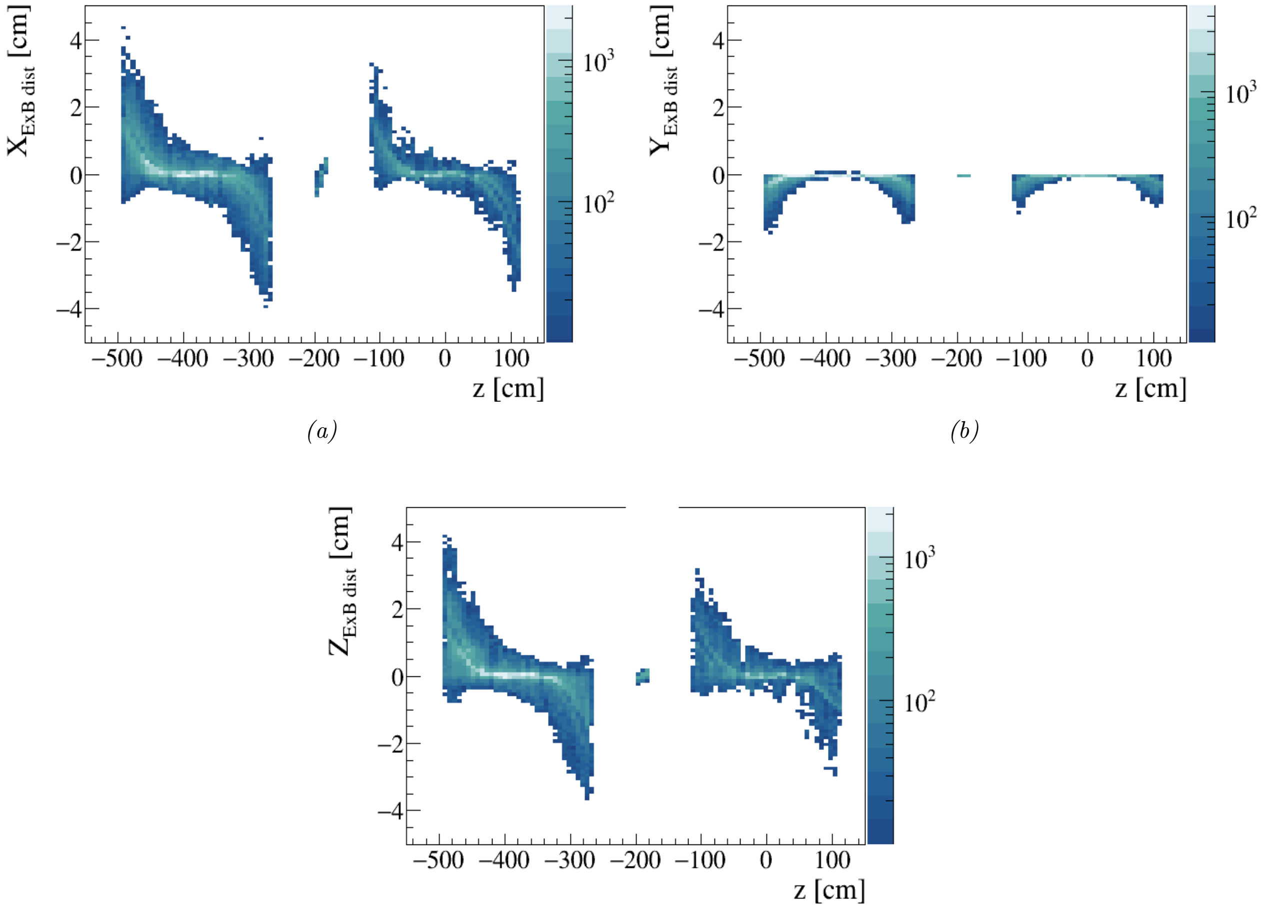

(a) *(b)* *(c)*

*Fig. 4.4: Size of the **E**×**B** distortion for the x (a), y (b), and z (c) cluster coordinates vs. cluster z position. In each plot, the first shape on the left is for clusters in the VTPC-1, the middle one is for the GTPC, and the last one is for the VTPC-2.*

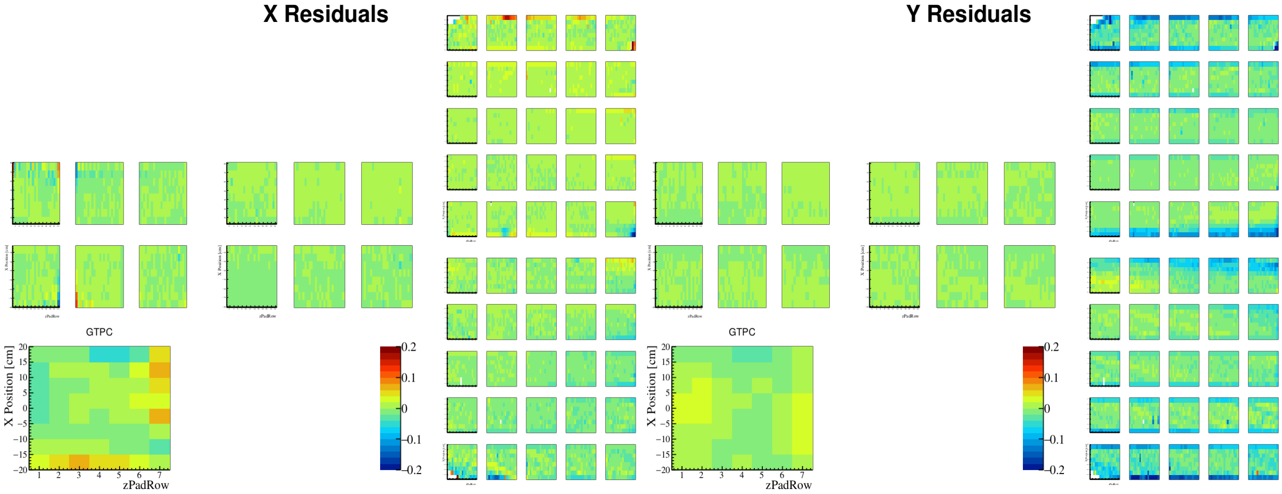

(a) (b)

Fig. 4.5: Data: Residuals between the cluster positions and the parent track's coordinates at the cluster's z coordinate along the x axis (a) and the y axis (b). The colour scale is ± 0.2 cm.

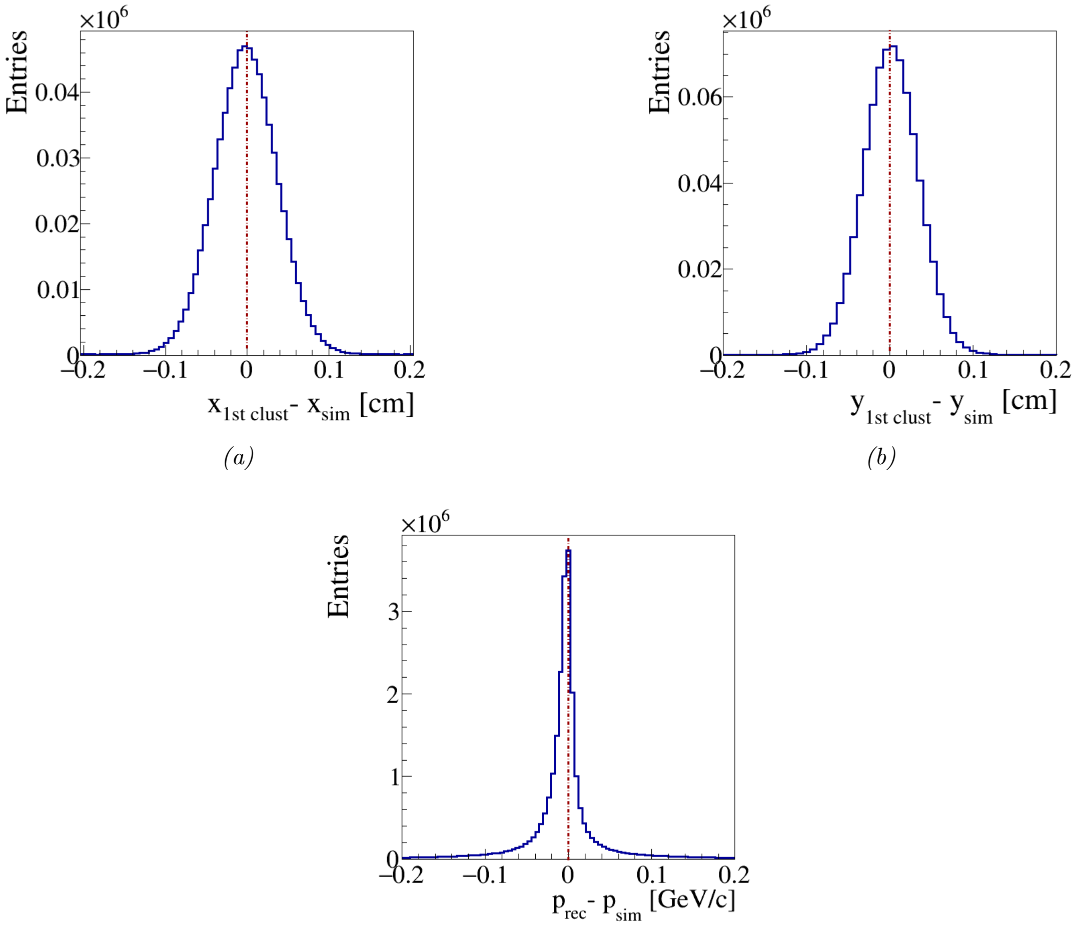

(a) (b)

(c)

Fig. 4.6: Comparison between reconstructed and simulated track parameters: x (a) and y (b) coordinates of the first clusters on particle tracks, as well as particle momenta p (c).

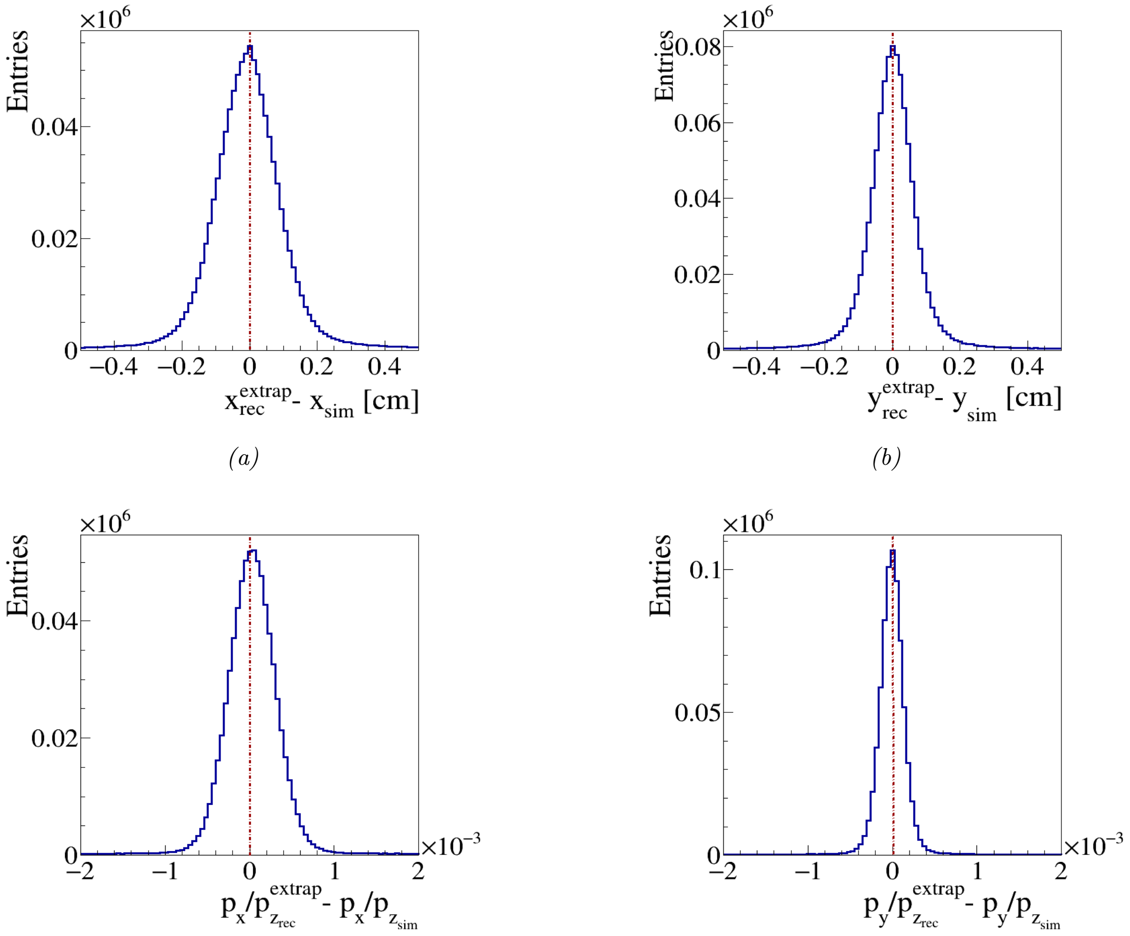

(a) *(b)*

(c) *(d)*

Fig. 4.7: Comparison between extrapolated and simulated track parameters on the target surface: x (a) and y (b) coordinates of the target exit point of particles and their track directions p_x/p_z (c) and p_y/p_z (d).

Once it is confirmed track reconstruction in the TPCs is not compromised, the accuracy of the backward track extrapolation from the detector to the replica surface is assessed. Reconstructed tracks from Monte Carlo are extrapolated to the target using the same procedure as for the data. Then, the extrapolated track parameters on the target surface are directly compared to the parameters at the generated particle exit point from the replica. In Fig. 4.7 the corresponding differences in x, y, and z coordinates and the track directions in the $x-z$ plane, p_x/p_z, and the $y-z$ plane, p_y/p_z, are shown. The total momentum is conserved during extrapolation to the target and is not plotted. The distributions in Fig. 4.7 have rather long tails, especially the plots for the target exit point coordinates. The extrapolation procedure depends on the track's momentum resolution and the distance between the first cluster and the target. As a result, the particle's exit point from the target might not be perfectly restored. Indeed, the backward extrapolation was one of the challenges of the analysis of the low magnetic field data and the largest systematic uncertainty source in many of the covered (p, θ, z) phase-space bins [128]. In the maximum magnetic field case, backward track extrapolation is considered among other systematic biases, but it is not a leading one. Different ways to aid the extrapolation procedure for future hadron production measurements with extended targets are being studied. The construction of additional tracking detectors surrounding the target or moving the latter a little inside VTPC-1, in the gap between sectors, are under consideration. For now, the benefits of these suggestions are studied using Monte Carlo.

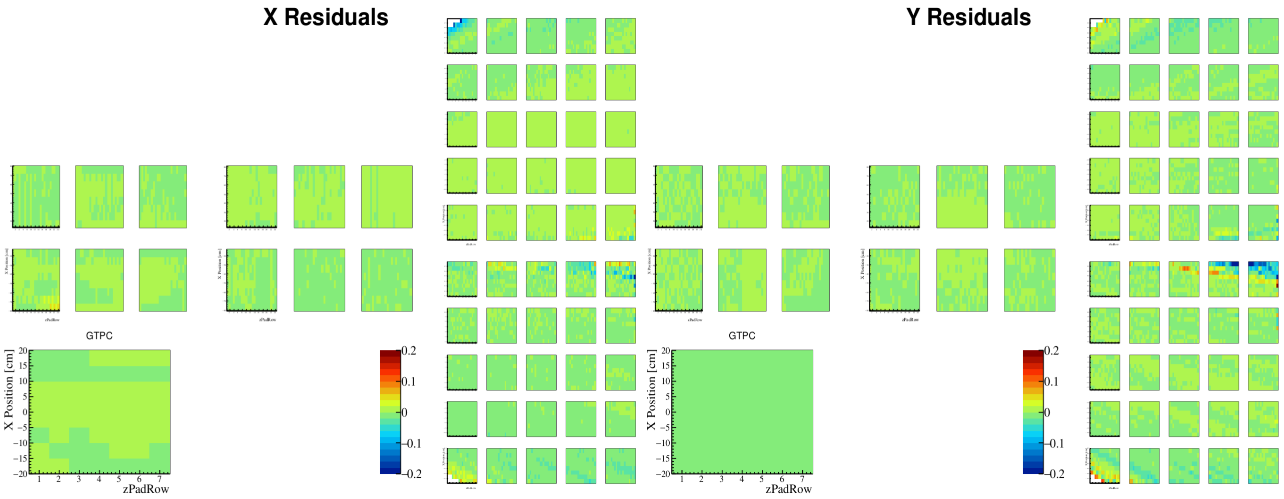

(a) *(b)*

Fig. 4.8: Monte Carlo: Residuals between the cluster positions and the parent track's coordinates at the cluster's z coordinate along the x axis (a) and the y axis (b). The colour scale is ±0.2 cm.

Similarly to data productions, the reconstruction of Monte Carlo events is inspected by calculating the residuals between cluster and parent track positions at the cluster's z coordinate. The obtained plots are shown in Fig. 4.8. The small magnitude of calculated residuals and the lack of any pattern inside the TPCs certify proper reconstruction of the Monte Carlo production.

Chapter 5

Analysis

Contents

In the summer of 2010, NA61/SHINE collected 1.2 M events with a 31 GeV/*c* proton beam on the T2K replica target with the maximal magnetic field in the spectrometer. As the strong magnetic field bends high-energy particles in the TPCs, the fraction of elastically and quasi-elastically scattered beam protons in the target is determined. Based on it, the production cross section in $p + C$ interactions at 31 GeV/*c* incident beam momentum is calculated. This replica-target result is expected to improve the precision of previously obtained production cross-section results from the 2007 and 2009 NA61/SHINE thin target data [106,126], thus reducing the associated systematic uncertainty of the T2K flux prediction. It will also aid understanding of the observed tension between thin- and thick-target tuned flux predictions.

This chapter presents the data analysis as follows: First, the scheme of production cross-section evaluation is presented. Next, selection of events and tracks is given. Then, two corrections are discussed: a Monte Carlo-based acceptance correction and a data-based TOF-F efficiency correction. Systematic biases of the end result are also discussed. Finally, the production cross-section estimate is given and compared to previous measurements.

5.1 Method for production cross-section evaluation

The presented approach to production cross-section estimation can be found in the review of experimental techniques given in Ref. [130]. When a particle goes through a thin slice of matter of thickness z along the particle trajectory, the probability the particle will interact, P_{int}, is

$$P_{\text{int}} = n\sigma z, \tag{5.1}$$

where n is the density of scattering centers and σ is the interaction cross section. On the other hand, when a particle passes through a material of any thickness, the probability the particle will not suffer an interaction, called *survival* probability and denoted P_{surv}, is

$$\begin{aligned} P_{\text{surv}}(z+dz) &= P_{\text{surv}}(z)(1-w\,dz), \\ P_{\text{surv}}(z) + \frac{dP_{\text{surv}}}{dz}dz &= P_{\text{surv}} - P_{\text{surv}}\,w\,dz, \\ dP_{\text{surv}} &= -w\,P_{\text{surv}}\,dz, \\ P_{\text{surv}} &= C\,exp(-w\,z), \end{aligned} \tag{5.2}$$

where $P_{\text{surv}}(z+dz)$ is the probability of not having an interaction between z and $z+dz$, $P_{\text{surv}}(z)$ is the probability of not having an interaction after traveling a distance z in the material, and $w\,dz$ is the probability of having an interaction between z and $z+dz$. The constant C is determined by the requirement $P_{\text{surv}}(z=0)=1$ and is $C=1$. Then, the probability that the particle will interact anywhere over distance z is

$$P_{\text{int}} = 1 - P_{\text{surv}} = 1 - exp(-w\,z). \tag{5.3}$$

The mean distance, λ, that the particle travelled without collision, which is the mean free path, is given by

$$\lambda = \frac{\int z P_{\text{surv}}(z)\,dz}{\int P_{\text{surv}}(z)\,dz} = \frac{1}{w}. \tag{5.4}$$

For a small material thickness, Eq. 5.3 can be approximated to

$$P_{\text{int}} = 1 - (1 - wz) = wz = \frac{z}{\lambda}. \tag{5.5}$$

Comparing Eqs. 5.1 and 5.5, one finds

$$\lambda = 1/n\sigma. \tag{5.6}$$

Finally, substituting Eqs. 5.4 and 5.6 into Eq. 5.2, the survival probability becomes

$$P_{\text{surv}} = exp(-n\sigma z). \tag{5.7}$$

In the current analysis, the formula in Eq. 5.7 is used to estimate the production cross section. The event and track selection procedures are designed to accept elastic and quasi-elastic interactions inside the target. The survival probability is then defined as the ratio

$$P_{\rm surv} = \frac{\text{Number of selected tracks}}{\text{Number of beam particles}} = e^{-Ln\sigma_{\rm prod}}, \tag{5.8}$$

where L is the target length along the beamline, n is the number density of carbon nuclei (scattering centers) in the T2K replica target, and the cross section in Eq. 5.7 is now the production cross section, $\sigma_{\rm prod}$. The next few sections explain how survival probability is extracted from the data.

5.2 Beam particle selection.

The NA61/SHINE beam is a secondary beam created when the primary SPS proton beam scatters on a beryllium target. Momentum selection is performed by the two spectrometers on the H2 line, see Chap. 3, Sec. 3.1.2. The beam momentum setting for this measurement is 30.92 GeV/c. Unfortunately, for this data-taking, a cross-check of this value is not possible on the NA61/SHINE side. The reason is no data was collected with the target removed from the beamline, which would have allowed direct detection of beam protons in the TPCs. Therefore, the 1% momentum spread reported for the H2 beamline in Ref. [74] is adopted as the precision of the beam momentum measurement. Further beam determination is carried out using the NA61/SHINE detectors.

Overall, the event selection ensures the beam consists of of protons that impinge on the target. For this purpose, the following requirements are imposed on the incoming beam particles:

1. particles pass the T3 trigger,
2. particles have measurements in all three BPDs in both orthogonal planes,
3. particles hit the upstream target face (UTF), the reconstructed path of each beam particle passes through the full target length and exists the target from the downstream target face (DTF).

The first condition provides that the beam particles produce the following signals in the scintillator counters and the Cherenkov detectors as described in Tab. 3.2:

$$\text{T3} = \text{S1} \ \wedge \ \text{S2} \ \wedge \overline{V_0} \ \wedge \ \overline{V_1^p} \wedge \ \text{CEDAR} \ \wedge \overline{\text{THC}}.$$

The two veto counters, $V0$ and V1^P, reduce beam divergence effects as they reject the beam halo at about 7 m upstream and just before the target region. Other scintillator detectors ensure that the beam hits the target. However, the S3 counter, which is closest to the target, is not featured in the used T3 trigger. The 90-cm-long replica is about 67 cm upstream of VTPC-1 and the VTX-1 magnet. Therefore, the fringe magnetic field in the target area is non-negligible, as is shown in Chap. 4, Sec. 4.1. The strong magnetic field affected the S3 counter operation and its signal was removed from the T3 trigger.

Particle type selection is performed by the two Cherenkov counters, CEDAR and THC, whose response is part of the T3 trigger. In order to select the pressure values in both detectors, special measurements, called pressure scans, are performed. In such scans, for a given particle momentum, the gas pressure is changed and the produced Cherenkov radiation is measured. The CEDAR and THC pressure scans for a 31 GeV/c beam are shown in Fig. 5.1. Both scans give consistent results on the hadron composition of the used secondary beam: about 86.3% π^+, 1.6% K^+, and 12.1% protons. To achieve a proton beam, the pressure in the CEDAR detector is set to about 3.3 bar and a value of 1.0 bar is chosen for the THC. Under the set conditions, in the CEDAR only protons produce Cherenkov photons at the angle, see Eq. 3.4, that allows their focusing on the 8 readout PMTs. A 6-fold coincidence of PMT signals is used for a positive tag. On the other hand, in the THC, which is used in anti-coincidence, protons do not produce Cherenkov radiation. In the end, a proton beam of high purity around 100% is achieved. In 2009, NA61/SHINE performed a purity check for an identified proton beam at 31 GeV/c. The target was removed and the maximal magnetic field was

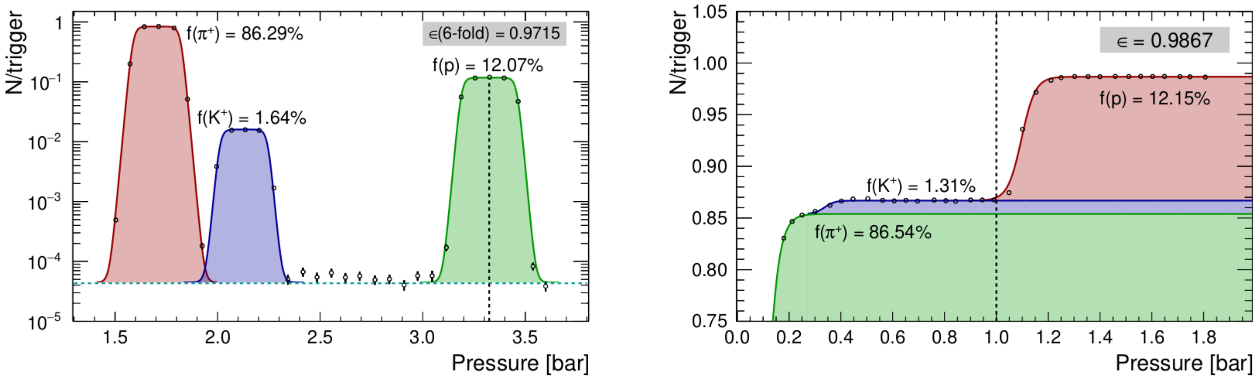

Fig. 5.1: Left: CEDAR pressure scan. Right: THC pressure scan. Detector efficiencies are given in grey. Beam composition in percentage is also reported. Vertical dotted lines indicate pressure settings used during the 2010 data-taking. The figure is from Ref. [112].

used to deflect beam particles into the TPCs. The energy loss measurements showed beam purity of about 99.8% [126]. Therefore, it is considered unnecessary to account for possible impurities of the beam.

Beam particles that are not synchronous to the trigger must be rejected. They are called pile-up or out-of-time events. These are additional beam particles that hit and interact in the target inside the acquisition time of the spectrometer. Typically, such events are removed during event selection. For this purpose, at NA61/SHINE, the Wave Form Analyzer (WFA) collects information from the beam counters to determine the number of beam particles that traverse the detector during the TPC readout. However, it has been reported, see Ref. [112], that a cabling problem with the WFA during the 2010 T2K replica-target runs degrade its measurements. Consequently, this detector has not been used to reject pile-up events and that task is transferred to another detector, the TOF-F. Removal of out-of-time beam particles is carried out based on the reconstructed track information, namely the presence of a TOF-F hit. The procedure is further explained in Sec. 5.3.

Returning to event selection, to maximize the precision of the beam track reconstruction, it is required that each beam particle must have been detected in all three BPDs in both orthogonal cathode planes. This is denoted as a 'BPD cut'. Straight lines in the $x - z$ and $y - z$ planes are fitted to the BPD cluster positions. These lines are then extrapolated to the z position of BPD-3. At this analysis stage, the beam profile parameters are obtained and saved since they are essential input for the Monte Carlo production, see Chap. 3, Sec. 3.3. The beam divergence in $x - z$ and $y - z$ planes is shown in Fig. 5.2.

Beam tracks are also extrapolated to the z planes containing the upstream and the downstream target face. There, it is required that the extrapolated beam coordinates fall inside a circle of a 1.28-cm radius. The center of the circle is set to the target (x, y) center position measured with respect to the BPDs using the low magnetic field dataset. More details about this measurement are given in Chap. 4, Sec. 4.1 and Ref. [112]. The coordinates of the centers of the upstream and the downstream target face-areas are identical since the target tilt is practically negligible, as reported in Tab. 4.1. Even though the target radius is 1.3 cm, the 1.28-cm cut value is chosen to account for the precision of the BPD measurement, which is around 200 μm. The cut on the beam spot size removes events where the beam particle hits the target close to its edge and at a relatively large angle. Once the requirement is applied to the upstream target face, the same requirement on the extrapolated beam at the downstream target face does not alter the event statistics much, see Tab. 5.1. The reason is that the mean beam polar angle during data-taking was about 0.3 mrad. Over the 90 cm of target length, this corresponds to below a millimeter shift in x or y position. Still, it is considered such a cut is meaningful in respect of the broad beam geometry of the setup. In this study, the process of interest is beam attenuation following particle interaction inside the target. Therefore, the contribution of beam divergence to that effect is kept as minimal as possible. The beam profiles on the UTF and the DTF are shown in Fig. 5.3. The red circles represent the boundaries of the target bases. The mesh structure on both plots originates

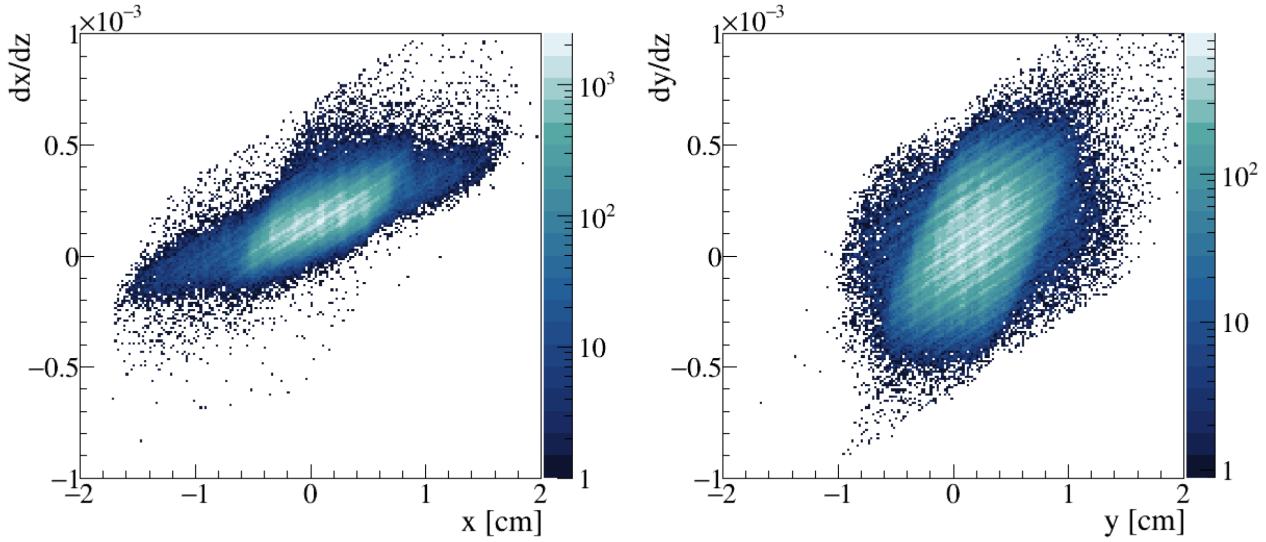

(a)

(b)

Fig. 5.2: Beam slope dx/dz vs. x position (a) and dy/dz vs. y (b) for beam particles selected by the T3 trigger. The distributions are used to generate beam particles in simulations at random $x - y$ positions.

Event selection criterion	N [10^6]
Total	1.235
T3 trigger	0.965
BPD cut	0.790
R_{upstream}	0.766
$R_{\text{downstream}}$	0.766

Tab. 5.1: Number of events after consecutive application of the event selection criteria. The notations $R_{upstream}$ and $R_{downstream}$ indicate the extrapolated beam track passed through the upstream and the downstream target face, respectively.

from the finite width and pitch between the strips on the cathode planes of the BPDs[1]. In addition, the width of the beam profile on the upstream target face is shown in Fig. 5.4. Due to the presence of two veto counters in the T3 trigger, most protons hit the target in a densely populated central target region of about 0.7-cm radius. Perfect agreement between the NA61/SHINE beam properties for a given hadron production measurement and the T2K beam is not feasible as the beam profile at T2K changes on a run-by-run basis. However, a comparison of the radial distributions of the two beams for the low magnetic field replica-target measurement and given T2K runs can be found in Fig. 3 in Ref. [128]. There, the T2K beam profile is wider than the used T3 beam profile. For the maximal field analysis, the width of the beam profile on the UTF is considered in the assessment of the systematic biases on the production cross-section result.

In the end, the numbers of remaining events in the course of the event selection process are given in Tab. 5.1.

---

[1] In Ref. [112], the check pattern in the beam profile is attributed to the description of the induced charge distribution on the cathode strip planes in the BPDs. For each cluster, the signals from 5 neighbouring strips on average are fitted with a Gaussian to determine the cluster position. In Ref. [131], it is shown that such an approach induces a bias in the reconstructed cluster positions, which can result in comb-like structures.

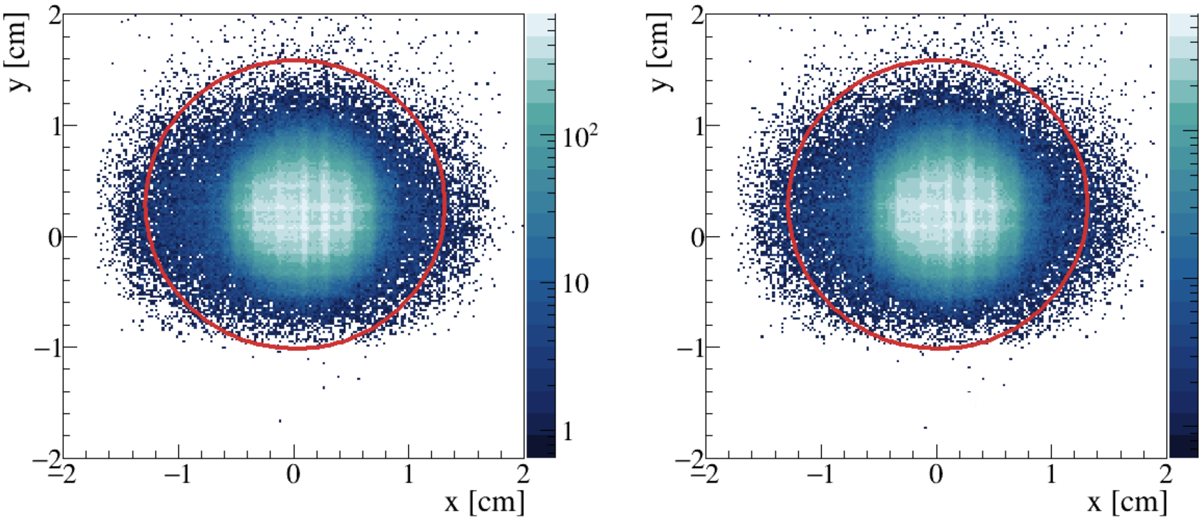

(a) *(b)*

Fig. 5.3: Beam $x - y$ profile at the upstream (b) and the downstream (b) target face before event selection is applied. The red circles mark the calibrated boundaries of the target bases.

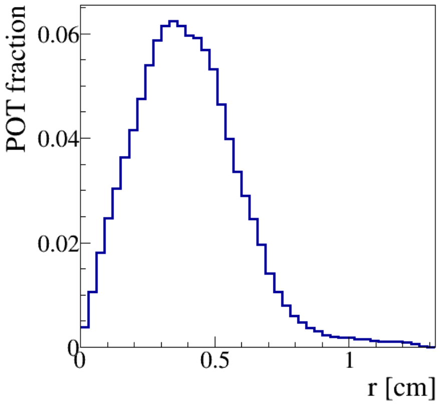

Fig. 5.4: Radial distribution of the incoming proton beam with respect to the center of the target for the selected T3 trigger.

5.3 Track selection

5.3.1 Track selection procedure

Among all particles that go through the NA61/SHINE TPCs, the track selection is designed to extract traces of high-energy beam particles that have passed through the full target length. These beam protons have scattered elastically or quasi-elastically inside the target. The track selection is outlined in the following few lines and is described in greater detail afterwards. Reconstructed particle tracks must

1. have fitted momentum,
2. have their point of closest approach to the target surface within $3\sigma_R$, where σ_R is the uncertainty of the extrapolated radial position,
3. be of a positively charged particle,

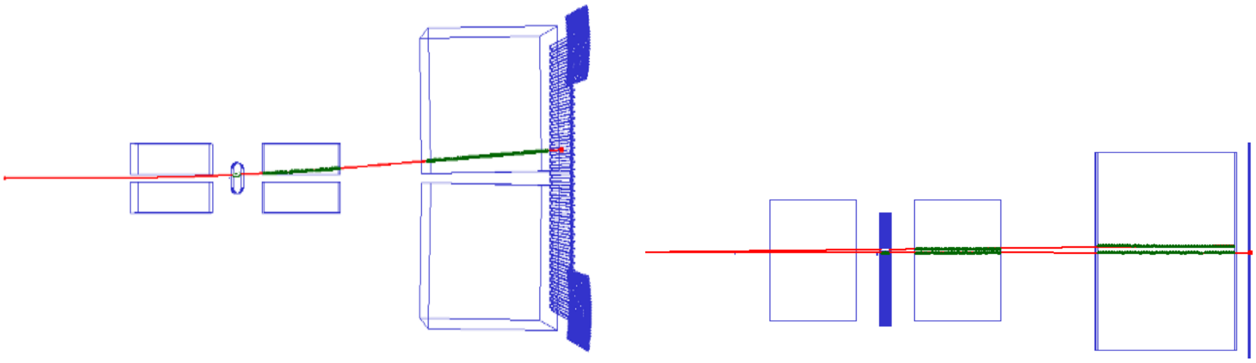
(a) (b)

Fig. 5.5: Top (a) and side (b) view of the tracks of two high-energy particles going through the TPCs. The beam comes from the left. The track points are shown in green and the reconstructed TPC tracks are given in red. The two tracks are indistinguishable in the $x - z$ plane shown on plot (a). Plot (b), illustrating the $y - z$ plane, shows that only one of the particles is detected by the TOF-F wall on the right. This is marked by a big red dot. The other track is of an off-time particle that scattered elastically or quasi-elastically in the target and did not produce a signal in the TOF detector, which was busy processing the previous hit. The images are taken from the NA61/SHINE event display.

4. have a hit in the TOF-F detector,
5. have emerged from the downstream target face, the $z6^{th}$ bin,
6. pass the dE/dx graphical cut,
7. have reconstructed momentum larger than 29.73 GeV/c,
8. be the only reconstructed particle trace in an event or must be reconstructed alongside other tracks that all have $p \geq 29.73$ GeV/c.

In the NA61/SHINE software framework, track must have more than 5 clusters in at least one TPC in order to be build. Then, track momentum is determined using nonlinear least-squares fit. If the fit is successful, the track is selected. Next, tracks are extrapolated backwards from the TPCs to the target surface. Extrapolation ends if the track hits the downstream target face or continues until the minimum distance to the target-body surface is reached. If that distance is less than three times the radial uncertainty[2] of the extrapolated position, the track is selected. This requirement removes most particles that do not emerge from the target, but are products of interactions and decays outside the target. Also, only traces of positively charged particles are accepted given the aim is to extract penetrating beam protons that scattered elastically or quasi-elastically inside the target.

It was mentioned in Sec. 5.2 that handling of pile-up events is based on the detection signals of particles that came out from the target rather than those of incoming beam protons. During the 2010 data-taking period, the mean time difference between beam particles was around 120 μs. The selection of on-time TPC tracks is ensured by a requirement that tracks must be matched to a TOF-F hit. Such a functionality of the TOF-F detector is possible since its acquisition time window is about 100 ns, while the readout time of the TPCs is much larger. It is the time electrons need to drift from the bottom to the top of the TPC chamber, which is around 50 μs for any of the TPCs, see Tab. 3.3. An example of a pile-up event is given in Fig. 5.5, where two particle tracks are detected by the TPCs in the same readout period. Both particles passed through the target without producing new hadrons. There is a small difference between their reconstructed momenta, namely $p_{track_1} = 30.54$ GeV/c and $p_{track_2} = 30.52$ GeV/c. Additionally, each of the two values is also close to the incident proton beam momentum of 31 GeV/c. Consequently, momentum conservation requires that one of the two particles

---

[2] The radial uncertainty is defined as $\sigma_R = \sqrt{\sigma_x^2 + \sigma_y^2}$, where σ_x^2 and σ_y^2 are the uncertainties of the extrapolated x and y coordinates of the target exit point.

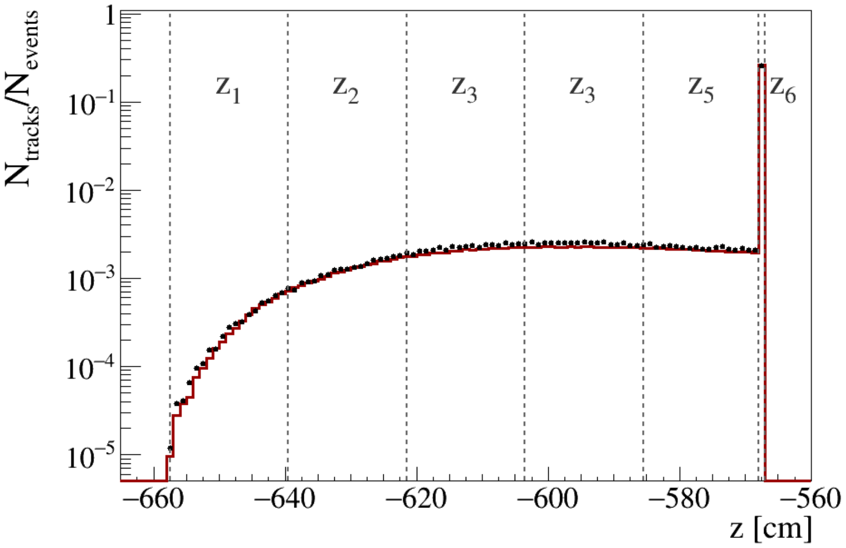

Fig. 5.6: Distributions of the z coordinates of the extrapolated target exit point of data (black points) and Monte Carlo (red line) tracks. Longitudinal bin borders are overlaid on top of the plot. The Monte Carlo input is from GEANT4 *simulations with the QBBC physics list.*

is a pile-up. To identify which one, the signal from the TOF-F is used. The particle that first entered the spectrometer passed the event selection and was matched to a recorded TOF-F hit. The second beam particle, the off-time particle, came afterwards and was not detected by the TOF-F wall as it hit the same TOF-F scintillator bar[3] while the signal of the first particle was being processed. Hence, the TOF-F hit requirement allows for the rejection of out-of-time TPC tracks. The case where an off-time beam particle produced new hadrons in the target, while the triggered event was an elastic or quasi-elastic one, is discussed under the systematic uncertainty study in Sec. 5.6.6.

Particles produced in in-target interactions are emitted from the whole target surface. They are detected by the TPCs and reconstructed TPC tracks are extrapolated backwards to the target surface. The extrapolated z position for each track is plotted in Fig. 5.6 for data and Monte Carlo. Alongside it, a schematic of the longitudinal z binning of the T2K replica target is given in Fig. 5.7. The vast majority of tracks are extrapolated to the downstream target face, which corresponds to the $z6^{th}$ bin. Actually, only particles which exit the target from the downstream target face are further analyzed. Such a choice is straightforward since the underlying process related to this production cross-section measurement is the beam attenuation in the target. Moreover, for the $z6^{th}$ bin, the radial uncertainty of the extrapolated position, shown in Fig. 5.8, is the lowest and is below 0.3 cm.

Contrary to the usual case, the TOF-F detector is not used in particle identification. The reason is that its resolution is insufficient for particle separation in the energy range of interest. However, the specific energy loss, dE/dx, measurements provide good discrimination between different particle types in the sample. Figure 5.9 shows the dE/dx vs momentum distribution for particles passing the selection so far. Two distinct areas of protons and pions are formed. A linear graphical cut, presented with a red line, is used to separate the two particle species. In the momentum range above 20 GeV/c, almost all particles are protons.

The most restrictive criterion in the selection is the momentum cut. It is required that reconstructed track momentum must be larger than 29.73 GeV/c. The reasoning behind this choice is explained in the next lines. The momentum cut value accounts for the continuous energy loss due to ionization in the target and the recoil energy in quasi-elastic interactions. Naturally, the energy transfer in elastic processes is less than in quasi-elastic ones and only the larger value is considered.

---

[3] Around 70% of forward-going high-energy particles hit the same scintillator bar.

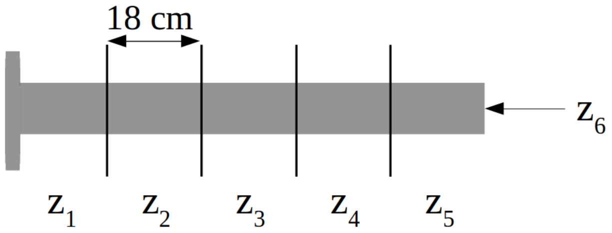

Fig. 5.7: Longitudinal binning scheme, adopted for the analysis of T2K replica target data. The target is divided in five equidistant 18-cm-long z bins, and the downstream target base is the last z6th bin.

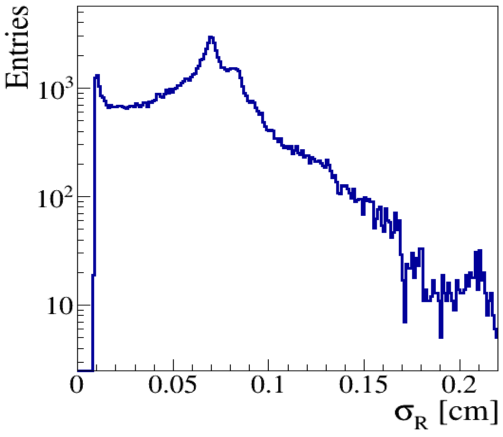

Fig. 5.8: Radial uncertainty of the obtained target-exit-point position for TPC tracks extrapolated to the downstream target face.

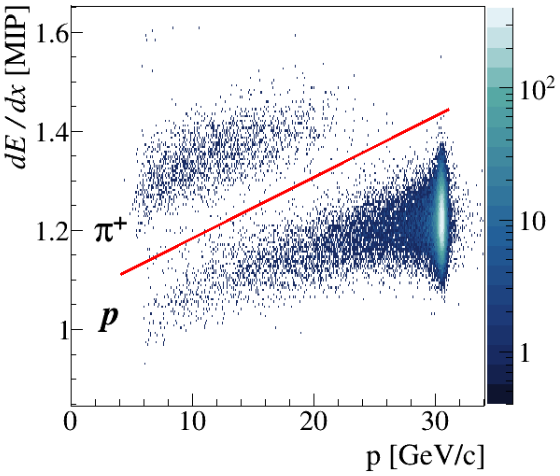

Fig. 5.9: Energy loss in the TPCs as a function of momentum. Protons and π^+ are well separated. The red line indicates the graphical cut applied in the track selection.

Let's first discuss the ionization losses inside the target and quantify their effect on the incident proton momentum. The ionization losses inside the target produce a Landau-distributed spectrum. These losses can be examined using simulations where the set beam and target properties recreate as closely as possible those during data-taking. For this purpose, a GEANT4 Monte Carlo with the QBBC physics list is employed. Only elastic interactions in the target are selected for this study. The resulting Monte Carlo energy loss distribution for 30.92 GeV/c protons going through a 90-cm-long graphite target with a density of 1.83 g/cm^3 is plotted in Fig. 5.10. It is fitted with a Landau function, which describes it well. However, a Landau distribution has an undefined mean. On the other hand, the median of such skewed distributions can be used to quantify them. The calculated median for the distribution in Fig. 5.10 is $E_{\text{ion}} = 315$ MeV. Additionally, using the Bethe-Bloch formula, the average energy loss of 30.92 GeV/c protons in 90 centimeters of carbon is estimated to about 342 MeV. However, the value adopted for the momentum cut determination is the reported median since it is a more conservative estimation. For other GEANT4 physics list, in case of elastic interactions in the target, the median of the energy loss distribution has the same magnitude.

In order to estimate the recoiling energy in elastic and quasi-elastic interactions, one can start with the four-momentum transfer, t, in a single interaction of these types

$$t = m^2 - 2E_{\text{beam}}E_{\text{out}} + 2\mathbf{p}_{\text{beam}} \cdot \mathbf{p}_{\text{out}} + m^2 = M^2 - 2ME_R + M^2, \tag{5.9}$$

where m is the proton mass, E_{beam} and p_{beam} are the total energy and momentum of the beam particle, E_{out} and p_{out} are the total energy and momentum of the outgoing proton particle that goes through the TPCs, while M is the rest mass of the recoiling particle, and E_R is its energy following the interaction. In the end, for elastic and quasi-elastic interactions with the carbon nuclei or the nucleons inside the nuclei, the kinetic energy of the recoiling particle, T_R, is

$$T_R = \frac{|t|}{2M} = \frac{p_{\text{beam}}^2\theta^2}{2M}, \tag{5.10}$$

where θ is the scattering angle between the incoming and outgoing particle. In elastic and quasi-elastic interactions, the scattered particle stays intact with most of its energy, and an applicable approximation of the four-momentum transfer is $|t| \sim p_{\text{beam}}^2\theta^2$. From Eq. 5.10, the kinetic energy of the recoiling particle is the largest when the recoil energy is transferred to a single nucleon, i.e. in a knock-out reaction. A value of 30 mrad, at the tail of the scattering angle distribution for particles with energy above 30 GeV, is assigned to θ in Eq. 5.10. This distribution is shown in Fig. 5.11. Thus, the calculated maximal kinetic energy of the recoiling particle in quasi-elastic interactions is 459 MeV. The binding energy of the nucleon inside the nucleus, which is about 8 MeV for carbon, is considered negligible compared to this kinetic recoil. Consequently, it is not reflected in the calculations. The length of the T2K replica target amounts to about two nuclear interaction lengths and one can expect, on average, two nuclear scatterings for a particle passing through the full target length. Taking this into account, the expected energy range of an outgoing elastically or quasi-elastically scattered beam particle, E_{out}, is

$$E_{\text{out}} \geq E_{\text{beam}} - E_{\text{ion}} - 2T_R. \tag{5.11}$$

In terms of proton momenta, Eq. 5.11 transforms to $p \geq 29.73$ GeV/c. There comes the momentum cut value in this analysis.

In elastic and quasi-elastic events, alongside the high-energy selection candidate, low-energy nuclear fragments, electrons, protons, neutrons, and de-excitation photons can be produced. Some of them do not escape from the target. Of the products that emerge from the target, the very low-energy charged particles are deflected away from the TPC system by the strong magnetic field, while neutral products cannot be detected by the TPCs. The remaining low-energy particles that have reconstructed tracks in the TPCs, don't reach the TOF detectors due to the strong bending. For such particles, particle identification relies solely on energy loss measurements. Unfortunately, the latter lie in a crossover region between electrons and π^- or protons and π^+. This is depicted in the low-momenta range in Fig. 5.12, which shows the specific energy loss vs. momentum distribution for tracks reconstructed in the same event with a high-energy selection candidate. In this case, particle type of low-energy products cannot be determined based on dE/dx information.

The unidentified products in the low-momenta range in Fig. 5.12 could be pions that are born in production interactions in the target. Production processes are not wanted in the selection. Therefore events, where low-energy products of unknown type are present should not be selected. But energy losses of the high-energy particles that are selection candidates are not plotted in Fig. 5.12. Then, at larger momenta Fig. 5.12 shows pile-up beam particles, primarily π^+ and protons, which have not undergone production interaction inside the target and have passed through the TPCs. An example of such an out-of-time track is shown in Fig. 5.5. To collect the maximum number of elastically and quasi-elastically scattered particles without damaging the purity of the selection, it is required that every reconstructed track in the same event as the selection candidate, if any, must have momentum larger than the calculated 29.73 GeV/c cut value. Therefore, interactions are discarded in cases where low-energy particles are detected by the TPCs, regardless of there being a high-energy proton track in

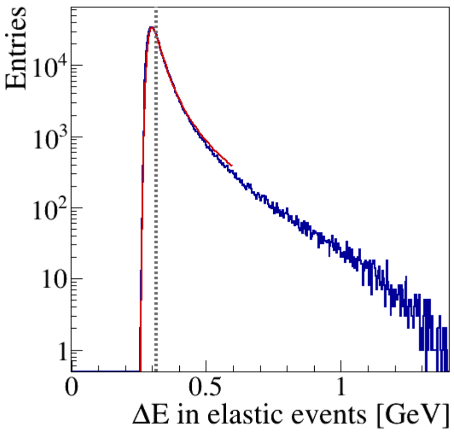

Fig. 5.10: Ionization energy losses inside the 90-cm-long T2K replica target as extracted from GEANT4 *QBBC physics list. Only particles undergoing elastic interactions inside the target are considered. A fit with a Landau function is overlaid on the plot. The median, which is at 315 MeV, is indicated with a dotted vertical line.*

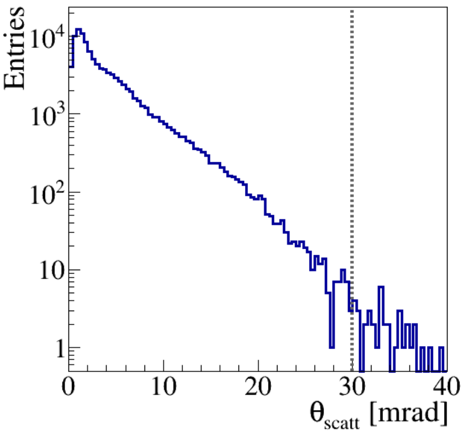

Fig. 5.11: Scattering angle distribution for particles having momenta larger than 30 GeV/c. The dotted line shows the chosen value, $\theta_{scatt} = 30$ mrad, for the computation of the maximal energy transfer in a quasi-elastic knock-out reaction.

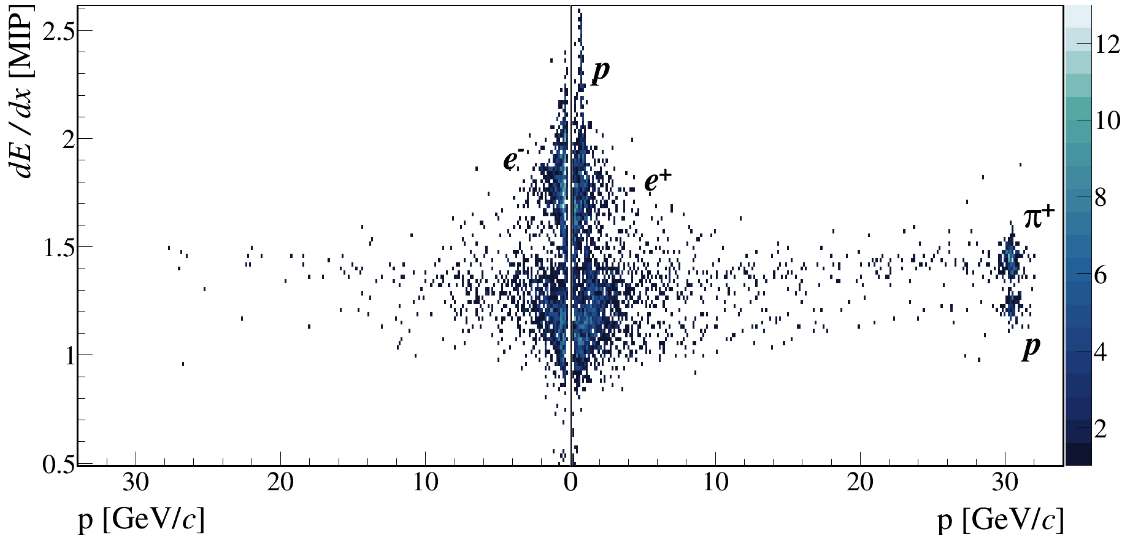

Fig. 5.12: Energy loss in the TPCs as a function of momentum for tracks produced alongside the high-energy selection candidate. On the left is the distribution for negatively charged particles, $q < 0$, while on the right is the distribution for positively charged ones, $q > 0$. Separation of particle species is troublesome in the low-momentum regions of both plots. For positive particles at momenta around the 31 GeV/c proton beam momentum, there are two distinct peaks. These are pile-up beam particles that have survived the nuclear interactions inside the target – off-time protons (lower) and π^+ (higher in $\mathrm{d}E/\mathrm{d}x$).

the same event. This way, tracks accompanied by an off-time elastically scattered beam particle will be selected, whereas tracks that are reconstructed alongside low-energy products, whose type cannot be resolved, are removed from the final sample. With this last requirement, the track selection is finalized. The numbers of remaining tracks in the course of the track selection process are given in Tab. 5.2.

Track selection criterion	N $[10^6]$
Fitted momentum	4.650
Distance from target	2.839
Charge	1.848
TOF-F hit	0.313
Target exit point	0.195
dE/dx meas.	0.176
$p \geq 29.73$ GeV/c	0.108

Tab. 5.2: Number of tracks after consecutive application of the track selection criteria.

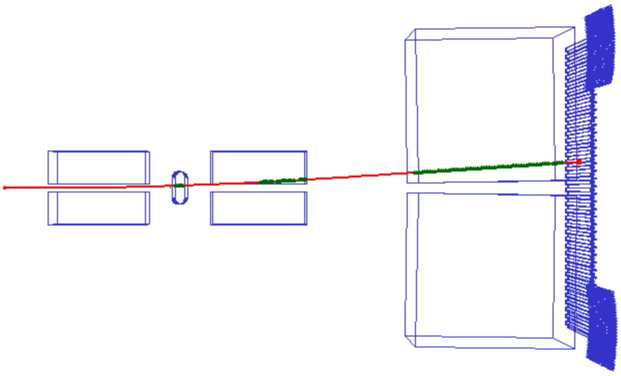

Fig. 5.13: Top view of a selected event - a single track going through GTPC, VTPC-2 and MTPC-L. The green markers, 125 in total, represent the measured points along the track. The red line is the reconstructed particle trajectory starting from the target on the left to the TOF-F wall on the right. The track's reconstructed momentum is $p = 30.34$ GeV/c. The image is taken from the NA61/SHINE event display.

5.3.2 Properties of the selected sample

Before closing this section, several important parameters of the selected high-energy track sample are discussed. To begin with, a typical selected event, i.e. a single track passing through the NA61/SHINE spectrometer, is shown in Fig. 5.13. This track has a total of 125 measured points, hits the TOF-F wall, and has momentum of 30.34 GeV/c.

Further, the phase space in $\{p, \theta\}$ of selected particle tracks is plotted in Fig. 5.14. Most tracks have polar angles below a few milliradians and momenta around 30.6 GeV/c, which corresponds to elastic scattering. In addition, the $\{\phi, \theta\}$ distribution of selected high-energy tracks is plotted in Fig. 5.15. In the narrow polar angle range of the sampled traces, the ϕ distribution is rather flat. The reason is the tailored detector configuration, which optimizes the spectrometer acceptance for beam protons penetrating the target and going through the TPCs. A slight preference to $-90° < \phi < 90°$ is also observed in Fig. 5.15. It could be caused by the non-zero magnetic field in the target area, which is deflecting beam protons during their passage in the replica to such values of the azimuthal angle.

In this analysis, traces of selected particles can be divided into two topologies based on the segments they have in different TPCs. Selected tracks have clusters in GTPC, VTPC-2, and MTPC-L. Less than 10% of them only go through GTPC and MTPC-L. No explicit restrictions on the number of points on track are applied in the selection procedure. However, for both track topologies, selection indirectly implies that the number of clusters in GTPC is the maximum possible, i.e. 7, and in the MTPC-L their number is more than 20, out of 90 possible. Tracks that pass through VTPC-2 turn out to have more than 20 clusters in that chamber, out of a maximum of 72. Due to the strong magnetic field, the selected high-energy tracks go through the gap between VTPC-1 sectors and do not have track segments in that chamber. In a TPC, the number of clusters on track influences momentum resolution. The total number of points per selected high-energy track is given in Fig. 5.16. The minor peak around $n_{clusters} = 97$ corresponds to tracks having segments in GTPC and MTPC-L.

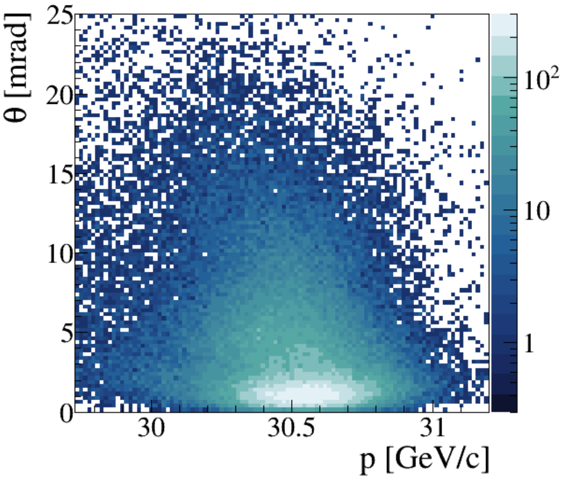

Fig. 5.14: Distribution of selected high-energy tracks in $\{p, \theta\}$. The abscissa range starts at the 29.73 GeV/c momentum cut value.

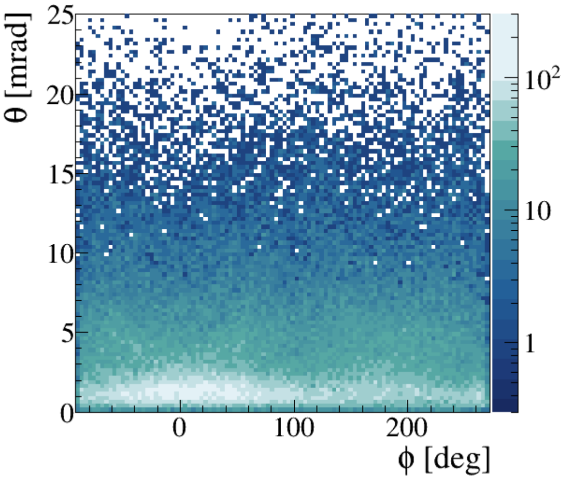

Fig. 5.15: Distribution of selected high-energy tracks in $\{\phi, \theta\}$ space.

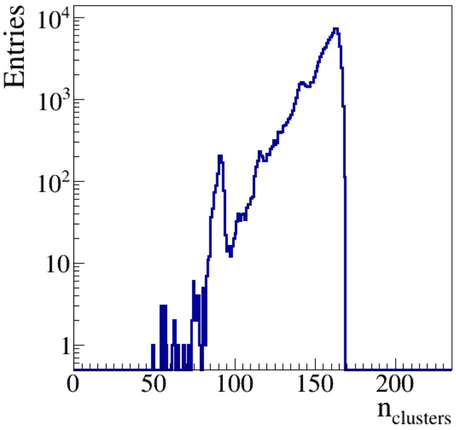

Fig. 5.16: Number of clusters per selected high-energy track.

The maximum number of clusters, given the two topologies of the final track sample, is 169. It corresponds to traces that spread over GTPC, VTPC-2, and MTPC-L. The resultant fractional momentum resolution is 5×10^{-3}.

Lastly, four-momentum transfer of selected tracks is shown in Fig. 5.17. An approximation that is valid for elastic and quasi-elastic scattering, $|t| \sim p^2_{\mathrm{beam}}\theta^2$, is made. Two regions of different steepness can be identified on the plot. They are fitted with two exponents given in colour. Following the approach of Bellettini *et al.* in Ref. [82], the low-momentum-transfer range ($|t| < 0.03$ (GeV/c)^2) is attributed to elastic interactions. There, a rapid variation in the t-distribution is observed, which is explained by the strong angular dependence of the cross sections for both Coulomb and coherent nuclear elastic scatterings. Then, for higher four-momentum transfers, a more moderate incline is exhibited. Similar change of slope is reported by Bellettini *et al.* and is interpreted as a domination of quasi-elastic over elastic scattering in this four-momentum transfer domain. Nevertheless, Bellettini *et al.* describe and quantitatively model the case of single interactions using thin targets. On the other hand, the t-distribution in Fig. 5.17 is smeared by the effects of ionization losses and multiple Coulomb scattering inside the 90-cm-long graphite target. Because of that difference, no comparisons are made between quantities extracted from the T2K replica target data and the measures in Ref. [82].

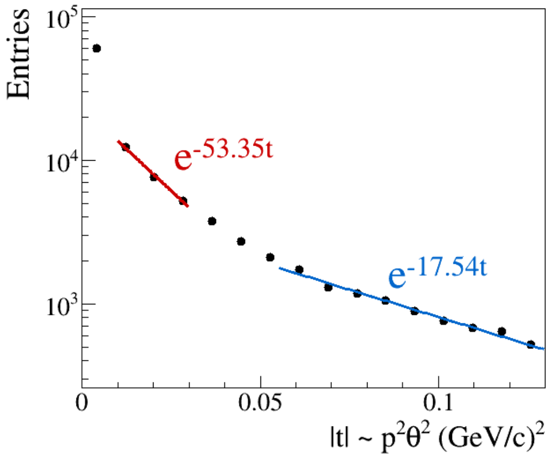

Fig. 5.17: Four-momentum transfer for particles passing the proposed selection of beam protons penetrating the thick target. The steep line in the low-momentum-transfer range (red) is associated with elastic interactions in the target. For higher four-momentum transfers, the fitted line (blue) is less steep, which is explained by domination of quasi-elastic scatterings over elastic ones. Note the logarithmic scale on the y axis.

5.4 Correction factors

The event and track selection procedures described in Secs. 5.2 and 5.3 provide the needed input to estimate the survival probability in Eq. 5.8. However, before any calculations are made, two corrections are applied to the extracted number of selected beam and TPC tracks. Those corrections are a Monte Carlo-based acceptance correction and a data-based TOF-F efficiency correction. Their product gives the total correction factor.

5.4.1 Monte Carlo correction

Approximately 6×10^6 events were simulated using GEANT4 version 10.4.p03 [118–120]. The beam properties from data are used to generate the Monte Carlo beam. The target position, which is calibrated using data from the maximal and the low magnetic field runs, is provided as input to the simulation. The Monte Carlo correction is defined as:

$$C^{MC} = \frac{\text{Number of non-production simulated events}}{\text{Number of selected reconstructed events}}, \tag{5.12}$$

where the numerator is the number of simulated beam protons that pass through the full target length and do not produce new hadrons inside it. The denominator is the number of reconstructed Monte Carlo events accepted as elastic or quasi-elastic by the same selection procedure applied to the data.

By means of a Monte Carlo correction various effects are treated at once. These include the efficiency of particle registration and reconstruction of particle tracks in the detectors. The former combines the geometrical acceptance of the spectrometer and particle transport through it, which includes secondary interactions with the detector material. The reconstruction effect is related to the efficiency of the software track reconstruction, which involves finding clusters among charge deposits in the detectors, track building and fitting of track parameters. In the case of replica-target measurements, it also includes backward track extrapolation from the TPCs to the target. The reconstruction efficiency in terms of track parameter resolution may determine whether a track passes certain selection criteria. For example, migration of the reconstructed momentum or longitudinal z target exit point with respect to the simulated (true) ones is of particular importance as track selection imposes restrictions on these parameters.

At the same time, the magnitude of the MC correction depends on several analysis definitions. By construction, any variation in the event and track selection has an impact on the magnitude of the MC correction factor. Also, in the simulation one must accurately reproduce the data-taking environment, including detector geometry. Thereby, the reconstruction algorithm in the Monte Carlo and the data case is run under similar conditions and a proper estimate of the MC correction can be obtained. Any differences between the spectrometer geometry description in the simulation and the real detector geometry would affect track reconstruction and thus the correction magnitude. Furthermore, the MC correction value is sensitive to changes related to the generation of particle interactions inside the target. Both interaction rates and particle production vary with different Monte Carlo generators, which makes the MC correction model dependent. The reference physics model employed in this analysis is the one of the GEANT4 QBBC physics list. A more detailed discussion on the physics model choice and dependence is given in Sec. 5.7. The calculated MC correction for the reference Monte Carlo sample is $C^{MC} = 1.035$. Sections 5.6 and 5.7 address all of the above-mentioned biases.

5.4.2 *TOF-F* efficiency correction factor

The response of the TOF-F detector is not simulated. Simply, if a simulated track passes through the TOF-F wall, a TOF-F hit is assigned to it. Therefore, the TOF-F efficiency cannot be corrected with the Monte Carlo correction factor. To account for it, another correction is added: the TOF-F correction. It is the inverse of the TOF-F efficiency. The latter is obtained from the efficiencies of the TOF-F scintillator bars, which are calculated from the data. The procedure to obtain bar efficiencies is described in Ref. [128].

The efficiency of each scintillator bar in the TOF-F detector is defined as the ratio of the number of tracks that hit that bar to the number of tracks that reach the end of the MTPCs and are extrapolated to a point that falls in the area of that scintillator bar. By requiring that tracks must have reached the MTPCs, one ensures that particles did not re-interact or decay before hitting the TOF-F wall. In Ref. [128], two factors that reduce the bar efficiency were identified. The first one is the endorsement of a quality cut on the timing difference between the signals of the top and bottom PMTs of each scintillator. It is required that this difference must be below 2000 ps. The timing cut is implemented to improve separation between particles for the mass squared particle identification. Even though this particle identification method is not applicable in the current analysis, the quality cut is preserved in the estimation of the TOF-F efficiency. During the 2010 data-taking, there were 4 bars with only one active channel due to a nonworking PMT or a DAQ problem. These bars are not affected by that quality cut. The second factor arises when in a single event two or more tracks hit and produce signal[4] in the same scintillator bar. In such a case, it is impossible to distinguish between tracks, and the TOF-F hit is discarded during reconstruction. This effect depends on the track density. In the end, the obtained efficiency of each scintillator bar is shown in Fig. 5.18. Except for the two bars closest to the beamline, the bar efficiencies vary slightly within a few percent.

The scintillator bar efficiencies are used to obtain the combined efficiency of all active bars. More explicitly, the TOF-F efficiency in the phase space of the selected tracks is calculated as

$$\epsilon^{\mathrm{TOF}} = \frac{n_{\mathrm{sel}}}{\sum_s n^s_{\mathrm{sel}}/\epsilon^s}, \tag{5.13}$$

where n_{sel} is the total number of selected data tracks, n^s_{sel} is the number of selected data tracks that hit bar s, and ϵ^s is the efficiency of this bar s. The summation goes over every active bar. The sample of selected tracks produced signals in about 10 scintillator bars. Most of the tracks, above 70%, hit the same bar as is shown in Fig. 5.19. In Fig. 5.19, the numbering of the bars starts close to the corner of MTPC-L at $x \approx 370$ cm, while the last bar is close to the corner of MTPC-R at $x \approx -370$ cm.

---

[4] Off-time events are only identified as such if produced particles hit a given TOF-F scintillator bar while it is processing previous signal. Then, pile-up particles will not produce any record.

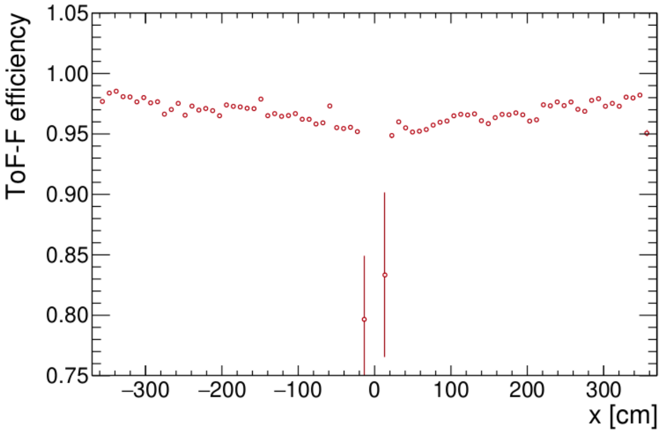

Fig. 5.18: Efficiency of each scintillator bar vs its x position. The efficiency gradually decreases from the sides to the center of the TOF-F wall at the beamline ($x = 0$ cm). The efficiency is much lower for the two bars around the beamline. The reason is the increasing track density with decreasing distance to the beam. In the current analysis, selected tracks go through MTPC-L and have positive x coordinates at the TOF-F z position. They also do not hit the central two bars. The figure is taken from Ref. [112].

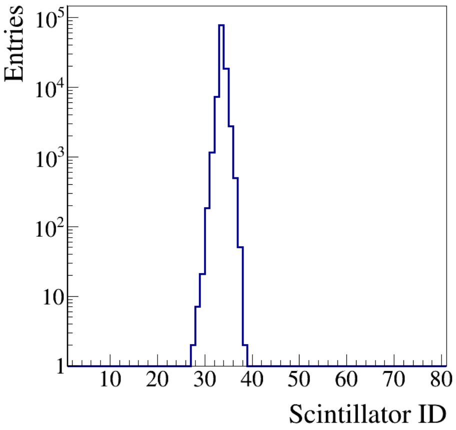

Fig. 5.19: Numbers of selected particles having a recorded hit in TOF-F scintillator bars. The TOF-F detector is positioned such that the first bar in the wall, ID = 1, is placed at about $x \approx 370$ cm and the last scintillator bar, ID = 80, is located at about $x \approx -370$ cm.

The estimated TOF-F efficiency is around 96%. Its uncertainty serves as an estimate of the TOF-F systematic uncertainty.

After completing the selection process and obtaining the MC and TOF-F efficiency correction factors, the production cross section can be calculated.

5.5 Production cross section

The probability, P_{surv}, that a beam particle avoids production interactions in the 90-cm-long target and the production cross section, σ_{prod}, are related via Eq. 5.8. Following the event and track selection procedures, described in Secs. 5.2 and 5.3, the number of selected beam particles is 766 164 and the number of selected tracks is 108 378. Using Eq. 5.8 for the survival probability and applying the correction factors from Eqs. 5.12 and 5.13, the production cross section becomes

$$\sigma_{\text{prod}} = -ln\left(\frac{\text{Number of selected tracks}}{\text{Number of beam particles}} \times C^{MC} \times \frac{1}{\epsilon^{\text{TOF}}}\right)/(L \cdot N_A \cdot \rho/\mu), \tag{5.14}$$

where the number density $n = N_A \cdot \rho/\mu$ is given in terms of Avogadro's number N_A, the target material density and molar mass, ρ and μ. Table 5.3 summarizes all quantities used in the estimation of σ_{prod} in Eq. 5.14. The production cross section for the measured $p + C$ reaction at 31 GeV/c incident beam momentum and its statistical uncertainty are

$$\sigma_{\text{prod}} = 227.6 \pm 0.8(\text{stat})\text{mb}. \tag{5.15}$$

The analysis further continues with the study of the systematic and physics model biases of this result.

Parameter	Value	Unit
Number of selected tracks	108 378	-
Number of selected beam particles	766 164	-
C^{MC}	1.035	-
ϵ^{TOF}	96.02 ± 0.56	%
L	90.0 ± 0.05	cm
N_A	$6.022{\times}10^{23}$	mol^{-1}
ρ	1.83 ± 0.01	g/cm^3
μ	12.01	g/mol

Tab. 5.3: Numerical values of all parameters that enter into the production cross-section formula Eq. 5.14. The reported here uncertainties are employed in the assessment of systematic effects.

5.6 Systematic uncertainties

Following many cross-checks and a broad overview of previous analyses within NA61/SHINE, several systematic uncertainty sources were identified. On one side, correcting data estimates with correction factors induces systematic biases. They are treated by changing certain analysis features such as cut values, the TPC chambers' positions, or the target position. Systematic uncertainties also arise from the finite precision of parameter values that enter the production cross-section calculation in Eq. 5.14. Furthermore, off-time events and the lack of capacity to perform particle identification of low-energy products are treated as systematic biases of the analysis and the cross-section result. The magnitude of most systematic effects is calculated as the deviation from unity of the ratio of the recalculated production cross section to the standard, nominal one. For other biases, the uncertainty of the associated parameter is propagated to the production-cross section result. In the current section, experimental systematic uncertainties are discussed, while the physics model uncertainty is presented in Sec. 5.7.

5.6.1 Target density

The target density enters the production cross-section calculation via the number density, as shown in Eq. 5.14. Dedicated measurements of the target mass and dimensions were carried out for the first NA61/SHINE data-taking with the T2K replica target in 2007 and were repeated in 2020 for the present analysis. The more conservative estimates from 2007 are adopted in the evaluation of the corresponding systematic bias. The reported target density is 1.83 ± 0.01 g/cm^3. Its uncertainty is propagated to the production cross-section result. The obtained target density systematic effect is ±0.6%.

The uncertainty related to the precision of the target length measurement is examined similarly to the target density case. The estimated systematic effect is below 0.06% and is considered negligible.

5.6.2 Backward track extrapolation

In this analysis, selected TPC tracks have their first reconstructed clusters inside the GTPC, which is about 3 m upstream of the target. This large distance affects the backward track extrapolation, and migration of the reconstructed target-exit-point position with respect to the actual one occurs. The accuracy of the backward track extrapolation depends on the precision of the momentum determination and the precision of the target position calibration. The TPC momentum measurement and its resolution are products of the track reconstruction, which is treated as a separate systematic uncertainty source and will not be discussed here. On the other hand, the target position and tilt, see Chap. 4, Sec. 4.1.1, have a finite precision that can induce biases when extrapolating TPC tracks backwards to the target surface. To study this bias, in the analysis codes the target position and tilt are changed within the calibration uncertainties, which are given in Tab. 4.1. Each target parameter is separately changed in positive and negative direction. The data are reprocessed and additional

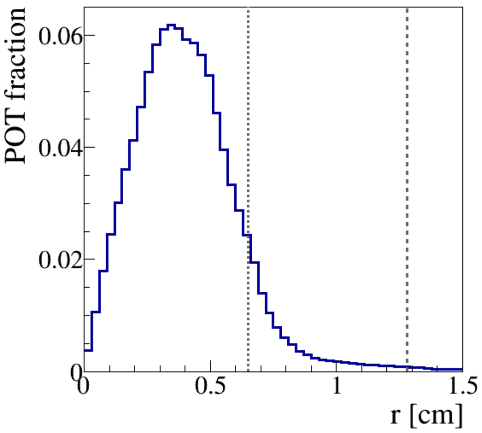

Fig. 5.20: Reduction in the number of selected beam particles when the beam spot size on the upstream target face is artificially narrowed in the selection. The nominal 1.28-cm and the new 0.65-cm radius cut values are indicated on the radial distribution of the incoming proton beam as dotted lines. The T3 trigger configuration is used.

estimates of the survival probability and the production cross section are obtained. The effects of the target position and tilt shifts in each axis and plane are added in quadrature, respecting sign, to form the total size of the backward track extrapolation bias, which is about ±0.1%.

5.6.3 Beam spot size on upstream target face

Many re-interactions can take place inside the 90-cm-long graphite target. Consequently, tracks that hit the target center are less likely to be scattered outside of the target before reaching its downstream end than those that hit the outer edge of the replica. To study this effect, for both data and Monte Carlo, the chosen value for the radius of the beam profile on the target front face is reduced from 1.28 cm to 0.65 cm, cutting down 10% of selected beam particles. The radial distribution in Fig. 5.20 shows this change. Both the survival probability, P_{surv}, and the MC correction, C^{MC}, are recalculated and an additional production cross-section estimate is obtained. The assigned systematic uncertainty is -0.2%.

5.6.4 Particle identification of low-energy products

In elastic and quasi-elastic events, besides the high-energy proton, low-energy nuclear fragments, electrons, protons, neutrons, and de-excitation photons can be produced. In the current analysis, the species of the above-mentioned charged particles cannot be resolved due to the limitations of the $\mathrm{d}E/\mathrm{d}x$ measurements, see Fig. 5.12, and the lack of TOF-F records for them. Consequently, such particles are indistinguishable from pions and kaons created in production interactions, which processes must not be selected. For that reason, events are discarded if the type of any of the produced particles cannot be resolved. However, simulations provide particle identification (PID) that can be consulted when calculating the Monte Carlo correction factor described in Sec. 5.4.1. For this purpose, matching of simulated and reconstructed tracks is performed and one knows the true particle type corresponding to each reconstructed trace in the MC sample. Then, reconstructed MC events, in which a high-energy proton is produced alongside low-energy particles such as protons, electrons, and nuclear fragments, can be flagged as elastic or quasi-elastic. If the high-energy proton in these flagged events passes all other selection criteria, those events and selected events with a single reconstructed high-energy proton track, will be used to calculate the MC correction factor. Their total number will become the denominator in Eq. 5.12. Overall, the described procedure mimics the case where PID is possible for all charged particles produced in an event. Using Monte Carlo PID, the MC correction factor is recalculated and so is the production cross section. The systematic uncertainty attributed to particle identification of low-energy products is -0.4%. It is one of the main contributors to the total systematic uncertainty of the production cross section.

5.6.5 Proton loss

Beam protons that have scattered elastically or quasi-elastically in the target may miss the TOF-F wall or re-interact with the detector material. Removal of the requirement for a TOF-F hit adds such particles to the selected sample. However, it also means that pile-up TPC tracks will join as well. Off-time beam particles surviving all interactions in the target and passing through the TPCs are not wanted and have to be accounted for. For this purpose, in an event where more than one high-energy particle trace, with momentum above 29.73 GeV/c, is reconstructed, a single track is accepted. As a result, an out-of-time track might be selected in place of the on-time track in the same event. Such an interchange of traces is admissible since the selection aims to extract a total number of desired particles, which is not binned in parameters such as momentum or polar angle. In addition, to ensure high-quality track reconstruction and momentum fit, selected traces in this study must have a segment in VTPC-2. With no requirement for a TOF-F detection, but with a VTPC-2 measurement, the survival probability, P_{surv}, and the MC correction, C^{MC}, are recalculated. The corresponding production cross-section value is compared to the standard result. A -0.1% effect is assigned to proton loss.

5.6.6 Off-time events

When the triggered beam particle undergoes an elastic or quasi-elastic interaction in the target, but there is also an off-time event that produces new hadrons in the replica (an off-time production event), the surviving beam particle will not be selected. The reason is the products of the two interaction types cannot be separated, and one cannot be certain of the underlying process from which a given track emerged. As a result, such elastic or quasi-elastic events are excluded from the analysis. However, the probability of such a combination of events, $P(EL+QE^{trigg}\ \&\ EL+QE^{off-time})$, can be estimated based on the number of cases where both the triggered and the out-of-time beam particles scatter elastically or quasi-elastically, denoted $N_{\text{EL+QE}^{\text{trigg}}\ \&\ \text{EL+QE}^{\text{off-time}}}$. It is assumed this number is the number of events that result in two reconstructed high-energy tracks in the TPCs altogether. Since the probability of any type of interaction in the target is independent of whether the beam particle is counted by the trigger system or not, one can write

$$\begin{aligned} P(EL+QE^{trigg}\ \&\ EL+QE^{off-time}) &= P(EL+QE)\cdot P(EL+QE)\cdot P(off-time) \\ &= \frac{N_{\text{EL+QE}^{\text{trigg}}\ \&\ \text{EL+QE}^{\text{off-time}}}}{N_{\text{events}}}, \end{aligned} \tag{5.16}$$

where $P(EL+QE)$ is the survival probability, $P(off-time)$ is the probability of there being an off-time beam particle, and N_{events} is the onumber of selected beam particles. The survival probability estimate from this analysis is employed. Following the Monte Carlo and TOF-F efficiency corrections, it is $P_{\text{surv}} = 0.15$. It is then straightforward to estimate the probability $P(off-time)$ from Eq. 5.16. It is about 2%. Further, the number of beam particles avoiding production interactions in the replica target but accompanied by products of an off-time beam particle production interaction, $N_{\text{EL+QE}^{\text{trigg}}\ \&\ \text{PROD}^{\text{off-time}}}$, is estimated from

$$\begin{aligned} P(EL+QE^{trigg}\ \&\ PROD^{off-time}) &= P(EL+QE)\cdot P(PROD)\cdot P(off-time) \\ &= P(EL+QE)\cdot[1-P(EL+QE)]\cdot P(off-time) \\ &= \frac{N_{\text{EL+QE}^{\text{trigg}}\ \&\ \text{PROD}^{\text{off-time}}}}{N_{\text{events}}}, \end{aligned} \tag{5.17}$$

where $P(PROD)$ is the probability of there being a production interaction. The number $N_{\text{EL+QE}^{\text{trigg}}\ \&\ \text{PROD}^{\text{off-time}}}$ is obtained from Eq. 5.17 and added to the total number of selected tracks.

This alters the survival probability in Eq. 5.14. The production cross section is recomputed, compared to the nominal result, and the systematic effect is found to be -0.8%. The effects caused by off-time beam particles are a dominant factor in the total systematic uncertainty of the end production cross-section result.

5.6.7 TOF efficiency uncertainty

Particles may also lack a recorded TOF-F hit, and so be removed from the selection, due to inefficiencies of that detector. More importantly, the TOF-F efficiency is used as a correction factor, which is described in Sec. 5.4.2, and so has an impact on the production cross-section value. For these reasons, the uncertainty of the calculated TOF-F efficiency is propagated to the production cross-section uncertainty. The uncertainty of the TOF-F efficiency comes from the efficiency uncertainties of individual scintillator bars and the statistical uncertainties of the numbers of particles that hit them, see Eq. 5.13. A conservative estimate of the efficiency uncertainty of each bar is 0.5% [112], while the overall uncertainty of the TOF-F detector efficiency is below 0.6%, see Tab. 5.3. The size of the systematic effect associated with the TOF efficiency is $\pm 0.3\%$.

5.6.8 Reconstruction

Potential differences between the detector description in the simulation and the real spectrometer would affect track reconstruction and bias the MC correction factor. The detector model serves as input to the Monte Carlo production chain. It consists of the detector geometry and information about used materials. Variation in the properties of the materials, such as density, will impact particle interaction rates and particle transport, including energy losses. However, one does not expect many re-interactions in the TPCs. Moreover, particle re-interactions are considered in the systematic uncertainty study in Sec. 5.6.5. Also, the bulk of interactions take place in the target, and the systematic effect related to its density is treated in Sec. 5.6.1. On the other hand, the $\mathrm{d}E/\mathrm{d}x$ measurement in the TPCs depends not only on the exact parameters of the gas but also on track reconstruction, which is sensitive to the detector description. Therefore, the effect of variations in the detector geometry should be examined. This is done by introducing small detector shifts in the geometry description used for the track reconstruction in the MC chain. The VTPC-2 position is moved by ± 0.2 mm in x and ± 0.3 mm in the y direction. The shift sizes are chosen to be much larger than any observed alignment and residual effect in the data calibration, see Chap. 4, Sec. 4.1.2. The other detectors are not moved since the selected high-energy tracks do not produce clusters in VTPC-1 and the GTPC covers the forward region. Although the MTPCs are crucial for the $\mathrm{d}E/\mathrm{d}x$ measurements, their positions are not shifted. The reason is that these chambers are well outside the magnetic field and are not used for momentum determination. The momentum selection is the most confining requirement in this analysis. Each VTPC-2 shift is separately introduced in positive and negative direction. The Monte Carlo correction factor and the production cross section are recalculated for each of the produced four MC samples. Their deviations from the nominal production cross-section estimate are then added in quadrature, taking into account the corresponding sign. The resulting asymmetric fractional uncertainty is $^{+0.5}_{-0.8}\%$.

5.6.9 Track momentum cut

As discussed in Sec. 5.3, the most constraining selection criterion is the momentum requirement $p \geq 29.73$ GeV/c. On one side, track momentum determination depends on the quality of TPC track reconstruction, which is separately studied. On the other side, the cut value itself, see Eqs. 5.11 and 5.10, depends on the beam momentum resolution. In absence of a beam momentum measurement, the beam momentum spread of less than 1%, which is reported in Ref. [74], is used. This spread is in turn propagated to the cut value uncertainty. Then, the cut value is varied within its estimated uncertainty, and track selection is repeated. The change in track selection reflects on both the survival probability and the Monte Carlo correction. The corresponding systematic effect is $\pm 0.2\%$. In this evaluation, no uncertainty is assigned to the chosen value of energy loss due to ionization inside the replica target.

Physics model used for correction	MC correction C^{MC}	Measured σ_{prod} [mb]	1 - $\frac{\sigma_{\text{prod}}^{\text{ref}}}{\sigma_{\text{prod}}}$ [%]
QBBC	1.035	227.6	-
FTFP_BERT	1.036	227.5	- 0.04
QGSP_BIC	1.042	226.8	- 0.4
FLUKA 2011.2c.5	1.037	227.4	- 0.09

Tab. 5.4: Monte Carlo correction, the production cross section obtained using the corresponding MC correction, and resulting fractional uncertainty for GEANT4 *version 10.4.p03 and* FLUKA *2011.2c.5 interaction generators. QBBC, FTFP_BERT, and QGSP_BIC are the employed three physics lists from* GEANT4*. The reference MC model is QBBC.*

5.7 Physics model uncertainty

It is discussed in Sec. 5.4.1 that introducing a Monte Carlo correction factor reduces many biases of the data estimates. However, a new dependence is induced. Variations in the Monte Carlo modeling of physics processes can lead to different values of the MC correction factor. In the analysis, the MC-related correction is estimated with GEANT4 version 10.4.p03 simulations using the QBBC physics list. The underlying model of elastic processes for this list is the recommended one by the GEANT4 collaboration [80]. In order to evaluate the physics model uncertainty, two additional GEANT4 physics lists are used: FTFP_BERT and QGSP_BIC. The treatment of elastic processes for FTFP_BERT and QGSP_BIC is identical, but it differs for QBBC. In general, modeling of inelastic, and so of its subgroup quasi-elastic, interactions changes with each of the three physics list. However, in the range of interest, above $p \geq 29.73$ GeV/c, QBBC and FTFP_BERT both use the Fritiof parton model. A separate Monte Carlo set using the FLUKA 2011.2c.5 package [100–102] is also prepared. The Monte Carlo samples for all of the GEANT4 physics lists and for FLUKA 2011.2c.5 are of the same size, namely 6×10^6 events. Normalized momentum, p, and polar angle, θ, distributions for reconstructed data and MC events are shown in Fig. 5.21. All traces that have more than 30 clusters in the TPCs are processed to obtain Fig. 5.21a. Fig. 5.21b is for tracks that pass the full selection procedure. In certain momentum and polar angle ranges, one or more MC models reproduce the data quite well. In others, all of the MC predictions differ from the data points. Such variations emphasize the necessity of simulation tuning with experimental data.

In order to estimate the size of the physics model bias, separate estimates of the MC correction factor are obtained for each MC set. Then, these MC corrections are used to evaluate the associated production cross sections. Table 5.4 presents production cross sections computed using the survival probability extracted from the data, applying Monte Carlo corrections calculated with each of the three GEANT4 lists and also with FLUKA 2011.2c.5. Previous NA61/SHINE production cross-section analyses used a GEANT4-based MC correction, while the latest NA61/SHINE results for hadron production in the T2K replica target rely on FLUKA 2011.2c.5 simulations for the MC correction of particle yields. Moreover, the T2K neutrino flux simulations employ FLUKA as a generator of hadronic interactions in the target. For these reasons, and as a cross-check, the FLUKA 2011.2c.5 Monte Carlo is produced and associated MC correction is applied to the data. The FLUKA-corrected production cross section is in best agreement with the FTFP_BERT one. Overall, production cross-section estimates with MC corrections from the three GEANT4 models and the FLUKA2011 model show good agreement. The maximum size of the uncertainty due to the modeling of interactions is observed for the QGSP_BIC list and is -0.4%.

In the presented analysis, and many other works, the physics model uncertainty is an essential part of the assessment of the total uncertainty of the end result. Still, in the current study, the model dependence is not the leading factor in the uncertainty. Such an effect is expected since the production cross section is directly obtained from survival probability using only a straightforward MC correction. On the contrary, the NA61/SHINE thin-target production cross-section estimates, see Chap. 3, Sec. 3.4.3, suffer from strong physics model dependence, which is the main contributor to their total uncertainty.

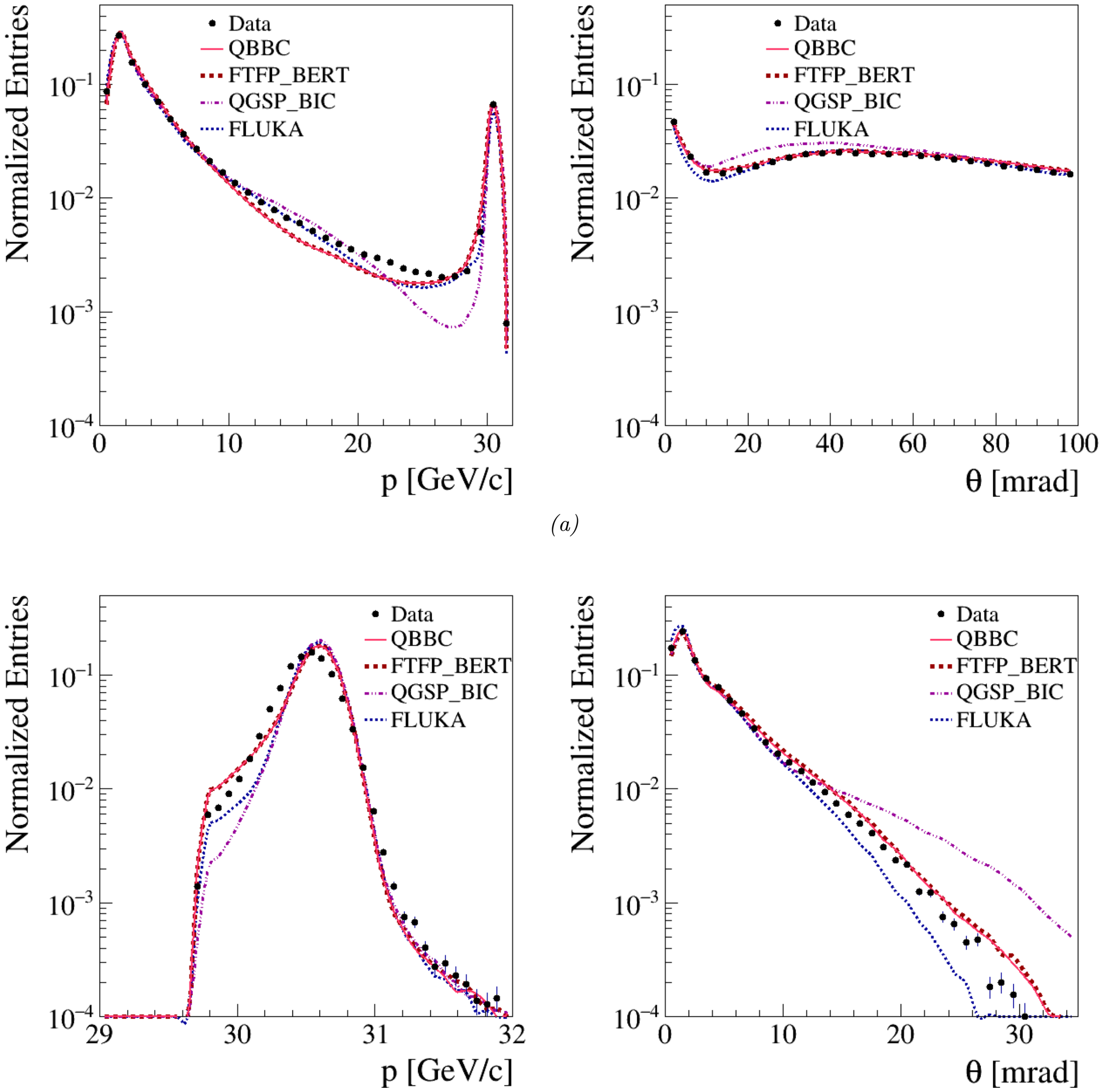

(a)

(b)

Fig. 5.21: Normalized momentum and polar angle distributions for all reconstructed tracks having more than 30 points in the detector (a), and for selected high-energy traces (b). Distributions for the three GEANT4 *physics lists (QBBC, FTFP_BERT, and QGSP_BIC) and* FLUKA *2011.2c.5 are displayed. The colour scheme is indicated on each plot. The sharp cut in the momentum distribution on the left-hand plot of (b) corresponds to the* $p \geq 29.73$ *GeV/c track selection requirement.*

Uncertainty source	Fractional size [%]
Target density	±0.6
Backward track extrapolation	±0.1
Beam spot size on upstream target face	-0.2
PID of low-energy products	-0.4
Proton loss	-0.1
Off-time events	-0.8
TOF-F efficiency	±0.3
Reconstruction	$^{+0.5}_{-0.8}$
Track momentum cut	±0.2
Physics model	-0.4
Statistical	±0.4

Tab. 5.5: Uncertainty sources considered in the current production cross-section measurement and their fractional magnitudes. Sections 5.6 and 5.7 describe each item.

5.8 Final result and discussion

5.8.1 Result and comparisons

It has been demonstrated that production cross section can be calculated from survival probability and thus experimentally determined via measurement of beam particles that penetrate a target of known length. In the analysis of p+T2K replica target interactions at 31 GeV/*c* incident beam momentum, a selection procedure is applied to identify beam protons that pass through the 90-cm-long target, interact elastically or quasi-elastically inside it, and leave a track in the spectrometer. Then, a number of systematic uncertainty sources are studied, including Monte Carlo modeling of target interactions. In the end, a production cross section for $p + C$ at 31 GeV/*c* interactions is obtained. The result, including statistical, systematic, and physics model uncertainties, is

$$\sigma_{\text{prod}} = 227.6 \pm 0.8(\text{stat})\ ^{+1.9}_{-3.2}(\text{sys})\ -0.8(\text{mod})\ \text{mb}. \tag{5.18}$$

The estimated total uncertainty of the reported production cross section is around 2%. A list of all identified uncertainty sources and their fractional magnitudes is given in Tab. 5.5. The sizes of experimental systematic sources, which exclude MC model bias, are added in quadrature respecting their sign to form the total asymmetric systematic uncertainty. To assess the model dependence, only GEANT4 physics models are used since it is unclear whether the FLUKA2011 generator includes simulation of quasi-elastic interactions. The differences between the cross sections obtained using MC corrections from each of the two additional GEANT4 physics lists, FTFP_BERT and QGSP_BIC, and the nominal QBBC-corrected production cross section are added in quadrature respecting sign to extract the model uncertainty. The model bias has a limited impact on the total uncertainty as a simple Monte Carlo correction is applied in this analysis. The main systematic biases come from sources such as the impossibility to tag off-time events, the event reconstruction (detector geometry), and the finite precision of the target density measurement.

The reported estimate can be compared to previous production cross-section measurements carried out by the NA61/SHINE collaboration or other groups. Such a comparison is illustrated in Fig. 5.22. In addition, Tab. 5.6 summarizes the production cross-section values and uncertainties that are shown in Fig. 5.22. To have a comparison between results from NA61/SHINE and external experiments, the production cross-section measurements for $p + C$ at 60 GeV/*c* by NA61/SHINE[5] [80] and by Carroll *et al.* [83] are also given. It should be stressed that the cross sections reported by Carroll *et al.* in Ref. [83] are categorized as production ones in the classification used by NA61/SHINE.

---

[5] The production cross-section measurement in $p + C$ interactions at 60 GeV/*c* beam momentum is part of NA61/SHINE's hadron production measurements program for Fermilab neutrino experiments.

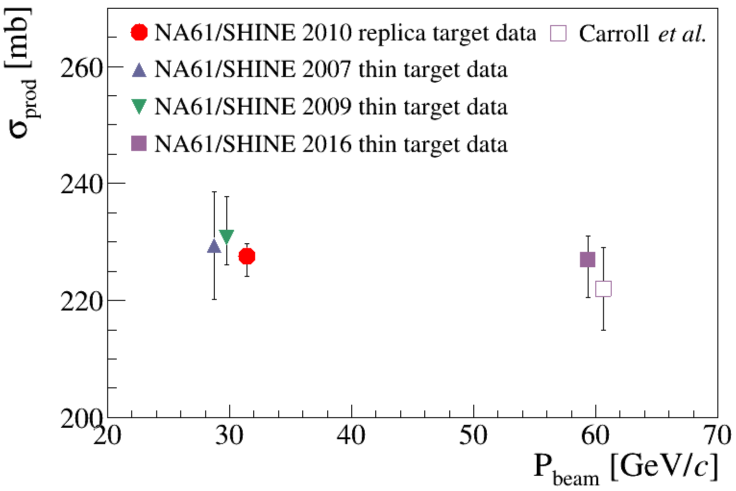

Fig. 5.22: The result of this analysis, represented by the red point, compared to the production cross-section measurements for $p + C$ interactions at different beam momenta. Alongside the NA61/SHINE thin-target results, production cross section by Carroll et al. at 60 GeV/c [83] is shown.

Experiment	p_{beam} [GeV/c]	σ_{prod} [mb]	Δ_{total} [mb]
NA61/SHINE 2010	31	227.6	$^{+2.1}_{-3.4}$
NA61/SHINE 2007	31	229.3	± 9.2
NA61/SHINE 2009	31	230.7	$^{+7.0}_{-4.6}$
NA61/SHINE 2016	60	226.9	$^{+4.1}_{-6.4}$
Carroll *et al.*	60	222	± 7

Tab. 5.6: Result of this analysis compared to the production cross-section thin-target measurements by NA61/SHINE [80,106,126] and Carroll et al. [83] for p+C interactions at different beam momenta. The reported total uncertainty (Δ_{total}) is the statistical, systematic and model uncertainties added in quadrature.

The current production cross-section measurement is in agreement with previous NA61/SHINE results for $p + C$ interactions at 31 GeV/c beam momentum [106, 126], while providing better precision. One of the reasons behind the lower uncertainty levels for the replica-target measurement is that the result is directly calculated from survival probability, while it is indirectly obtained in the thin-target case. In the latter, the production cross section is computed from the trigger cross section by subtraction of products of Monte Carlo-based correction factors and cross sections. Therefore, the physics model dependence of the thin-target results is much stronger than it is for the replica target one. The pronounced model bias of thin-target production cross-section estimates can be viewed as an argument supporting production cross-section measurements by means of beam attenuation in extended targets.

5.8.2 Possible implications for the T2K neutrino flux prediction

Presented here is a direct production cross-section measurement based on the number of beam particles penetrating a thick medium – a replica of the T2K target. Even though the reported result is not yet employed in the re-weighting of the T2K neutrino flux, some indications about its impact can be inferred. To begin with, the lower total uncertainty of the current measurement with respect to previous estimates will allow for a more precise hadron interaction rate re-weighting of the T2K neutrino flux simulation. Of course, any qualitative evaluations can be made only after implementation of the presented replica-target result in the T2K neutrino beam simulation. Moreover, this thick-target measurement aids the understanding of the discrepancy between thin and replica target re-weighted neutrino flux predictions at T2K[6], see Chap. 2, Sec. 2.2.4. The replica-target result is complementary and uncorrelated to NA61/SHINE thin-target measurements. Negligible tension between the thin and thick target production cross-section estimates is found. This indicates further studies of the cause(s) of the discrepancy between thin- and replica-target constrained flux predictions is(are) needed. Actually, in Ref. [127], it is shown that better agreement between measured $\pi^{\pm}$ yields on the surface of the T2K replica target and MC predictions can be obtained shall the production cross section be around 221 mb. The result presented in this work can accommodate such a value within two standard deviations, but its central value is about 3% higher. In the near future, following the approach of Bellettini *et al.* [82], the EMPHATIC collaboration is expected to release another production cross-section estimate of $p+C$ interactions at 31 GeV/c momentum. It will likely shed more light on the thin versus replica target tuning puzzle. In the end, although the reported production cross section is based on a measurement with the T2K replica target, the result can still be used to tune hadron interaction models used in simulations at other neutrino beamlines.

---

[6] Deviations from unity of the ratio of thin- and thick-target tuned flux predictions have also been reported for the neutrino beam simulation at the MINERνA experiment [73].

Chapter 6

Conclusions and Future Prospects

Precise hadron production measurements are crucial for reducing the total systematic uncertainty of the neutrino flux predictions at accelerator-based neutrino experiments. The NA61/SHINE experiment facilitates such reference measurements since more than a decade now. The obtained results, particle yields and interaction cross sections, are being used to constrain neutrino beam simulations at long-baseline neutrino experiments such as T2K. For tuning of the T2K beam prediction, NA61/ SHINE performed measurements with a 2-cm-thin carbon target and a 90-cm-long T2K replica target. This thesis describes an experimental study of proton interactions on carbon nuclei reproduced when a 31 GeV/*c* proton beam strikes the T2K replica target at the entrance of the NA61/SHINE spectrometer. Presented is a method for production cross-section evaluation based on measurement of beam attenuation in the thick target. This approach lowers the physics model dependence of the result since a simple Monte Carlo-based correction is applied during analysis. The obtained production cross section is

$$\sigma_{\text{prod}} \; = \; 227.6 \; \pm \; 0.8(\text{stat}) \, ^{+\,1.9}_{-\,3.2}(\text{sys}) \; - \; 0.8(\text{mod}) \text{ mb}.$$

The reported value is in agreement with previous NA61/SHINE production cross-section results in $p + C$ interactions at 31 GeV/*c* incident beam momenta. It also has the smallest total uncertainty. That being said, the current replica-target measurement implies further studies are needed to understand the discrepancy between thin- and thick-target tuned neutrino flux predictions. Still, the calculated production cross section will be implemented in the T2K flux prediction and will help reduce the hadron production-related flux uncertainty.

In the future, NA61/SHINE plans for more hadron production measurements with both thin and extended targets, observing the requirements for more precise flux predictions at current and next generation accelerator-based neutrino experiments. During CERN's Long Shutdown 2, the NA61/SHINE collaboration has been working on important detector upgrades, including replacement of the TPC readout electronics, new beam trigger and data acquisition system, new TOF and vertex detectors [77]. These improvements will enable an increase of the data-taking rate by a factor of 10 to 1 kHz and will lower down measurement uncertainties. Dedicated research of the feasibility and the construction of a Very Low Energy tertiary beamline (beam momenta in range 1-20 GeV/*c*) is under action as well. It will allow for hadron production measurements in energy regions where reference data is sparse or nonexistent.

Bibliography

[1] N. Bohr *J. Chem. Soc.* (1932) 349–384. Faraday lecture. chemistry and the quantum theory of atomic constitution.

[2] W. Pauli, "Pauli letter collection: letter to Lise Meitner," 1930-12-04. Letter 259.

[3] F. Reines and C. Cowan *Phys. Rev.* **92** (1953) 830–831.

[4] G. Danby, J. Gaillard, K. A. Goulianos, L. Lederman, N. B. Mistry, M. Schwartz, and J. Steinberger *Phys. Rev. Lett.* **9** (1962) 36–44.

[5] K. Kodama *et al.*, [DONUT Collab.] *Phys. Lett. B* **504** (2001) 218–224, `arXiv:hep-ex/0012035`.

[6] R. Davis, Jr., D. S. Harmer, and K. C. Hoffman *Phys. Rev. Lett.* **20** (1968) 1205–1209.

[7] Z. Maki, M. Nakagawa, and S. Sakata *Prog. Theor. Phys.* **28** (1962) 870–880.

[8] B. Pontecorvo *Sov. Phys. JETP* **26** (1968) 984–988. Neutrino Experiments and the Problem of Conservation of Leptonic Charge.

[9] K. Hirata *et al.*, [Kamiokande-II Collab.] *Phys. Lett. B* **280** (1992) 146–152.

[10] Y. Fukuda *et al.*, [Super-Kamiokande Collab.] *Phys. Rev. Lett.* **81** (1998) 1562–1567, `arXiv:hep-ex/9807003`.

[11] Q. Ahmad *et al.*, [SNO Collab.] *Phys. Rev. Lett.* **87** (2001) 071301, `arXiv:nucl-ex/0106015`.

[12] M. Aker *et al.*, [KATRIN Collab.] *Phys. Rev. Lett.* **123** no. 22, (2019) 221802, `arXiv:1909.06048 [hep-ex]`.

[13] N. Aghanim *et al.*, [Planck Collab.] *Astron. Astrophys.* **641** (2020) A6, `arXiv:1807.06209 [astro-ph.CO]`.

[14] M. Gell-Mann, P. Ramond, and R. Slansky *Conf. Proc. C* **790927** (1979) 315–321, `arXiv:1306.4669 [hep-th]`.

[15] T. Yanagida *Conf. Proc. C* **7902131** (1979) 95–99. KEK-79-18-95.

[16] R. N. Mohapatra and G. Senjanovic *Phys. Rev. Lett.* **44** (1980) 912.

[17] J. Ebert *et al. Phys. Rev. C* **94** no. 2, (2016) 024603, `arXiv:1509.04113 [nucl-ex]`.

[18] C. Alduino *et al.*, [CUORE Collab.] *Eur. Phys. J. C* **79** no. 9, (2019) 795, `arXiv:1811.10363 [nucl-ex]`.

[19] S. Cebrian *Prog. Part. Nucl. Phys.* **114** (2020) 103807, `arXiv:2008.06426 [nucl-ex]`.

[20] X. Qian and P. Vogel *Prog. Part. Nucl. Phys.* **83** (2015) 1–30, `arXiv:1505.01891 [hep-ex]`.

[21] S. Mondal `arXiv:1511.06752 [hep-ph]`. Physics of Neutrino Oscillation.

[22] L. Wolfenstein *Phys. Rev. D* **17** (1978) 2369–2374.

[23] S. Mikheyev and A. Smirnov *Sov. J. Nucl. Phys.* **42** (1985) 913–917.

[24] A. Suzuki, [KamLAND Collab.] *Phys. Scripta T* **121** (2005) 33–38.

[25] Y. Suzuki *Eur. Phys. J. C* **79** no. 4, (2019) 298.

[26] Y. Nakajima, “Recent results and future prospects from super-kamiokande,” June, 2020. Plenary Talk from Neutrino 2020.

[27] I. Esteban, M. Gonzalez-Garcia, M. Maltoni, T. Schwetz, and A. Zhou *JHEP* **09** (2020) 178, `arXiv:2007.14792 [hep-ph]`.

[28] N. Vinyoles, A. M. Serenelli, F. L. Villante, S. Basu, J. Bergström, M. Gonzalez-Garcia, M. Maltoni, C. Peña Garay, and N. Song *Astrophys. J.* **835** no. 2, (2017) 202, `arXiv:1611.09867 [astro-ph.SR]`.

[29] M. Aartsen *et al.*, [IceCube Collab.] *Phys. Rev. Lett.* **120** no. 7, (2018) 071801, `arXiv:1707.07081 [hep-ex]`.

[30] M. Aartsen *et al.*, [IceCube Collab.] *Phys. Rev. D* **99** no. 3, (2019) 032007, `arXiv:1901.05366 [hep-ex]`.

[31] K. Abe *et al.*, [T2K Collab.] *Nucl. Instrum. Meth. A* **659** (2011) 106–135, `arXiv:1106.1238 [physics.ins-det]`.

[32] J. Evans, [MINOS Collab.] *Adv. High Energy Phys.* **2013** (2013) 182537, `arXiv:1307.0721 [hep-ex]`.

[33] D. Ayres *et al.*, [NOvA Collab.], “The NOvA Technical Design Report,” 10, 2007. FERMILAB-DESIGN-2007-01.

[34] P. Dunne, “Latest neutrino oscillation results from t2k,” July, 2020. Plenary Talk from Neutrino 2020.

[35] A. Himmel, “New oscillation results from the nova experiment,” July, 2020. Plenary Talk from Neutrino 2020.

[36] M. Scott, [T2K Collab.] *J. Phys. Conf. Ser.* **1342** no. 1, (2020) 012043.

[37] NuFIT 5.0 web page, 2020. `http://www.nu-fit.org/`.

[38] Y. Abe *et al.*, [Double Chooz Collab.] *Phys. Rev. Lett.* **108** (2012) 131801, `arXiv:1112.6353 [hep-ex]`.

[39] F. An *et al.*, [Daya Bay Collab.] *Phys. Rev. Lett.* **108** (2012) 171803, `arXiv:1203.1669 [hep-ex]`.

[40] J. Ahn *et al.*, [RENO Collab.] *Phys. Rev. Lett.* **108** (2012) 191802, `arXiv:1204.0626 [hep-ex]`.

[41] K. Abe *et al.*, [T2K Collab.] *Nature* **580** no. 7803, (2020) 339–344, `arXiv:1910.03887 [hep-ex]`. [Erratum: Nature 583, E16 (2020)].

[42] M. A. Tórtola, G. Barenboim, and C. A. Ternes *JHEP* **07** (2020) 155, `arXiv:2005.05975 [hep-ph]`.

[43] I. Esteban, M. Gonzalez-Garcia, A. Hernandez-Cabezudo, M. Maltoni, and T. Schwetz *JHEP* **01** (2019) 106, `arXiv:1811.05487 [hep-ph]`.

[44] P. D. Group *et al. Progress of Theoretical and Experimental Physics* **2020** no. 8, (2020) .

[45] P. de Salas *et al.* `arXiv:2006.11237 [hep-ph]`. 2020 Global reassessment of the neutrino oscillation picture.

[46] R. Acciarri *et al.*, [DUNE Collab.], "Long-Baseline Neutrino Facility (LBNF) and Deep Underground Neutrino Experiment (DUNE): Conceptual Design Report, Volume 2: The Physics Program for DUNE at LBNF," 12, 2015. `arXiv:1512.06148 [physics.ins-det]`.

[47] K. Abe *et al.*, [Hyper-Kamiokande Collab.], "Hyper-Kamiokande Design Report," 5, 2018. `arXiv:1805.04163 [physics.ins-det]`.

[48] S. van der Meer, *A directive device for charged particles and its use in an enhanced neutrino beam.* CERN Yellow Reports: Monographs. CERN, Geneva, 1961.

[49] L. Aliaga Soplin, *Neutrino Flux Prediction for the NuMI Beamline.* PhD thesis, William-Mary Coll., 2016.

[50] S. E. Kopp *Phys. Rept.* **439** (2007) 101–159, `arXiv:physics/0609129`.

[51] H. Atherton *et al.*, *Precise Measurements of Particle Production by 400-GeV/c Protons on Beryllium Targets.* 1980.

[52] G. Ambrosini *et al.*, [SPY Collab.] *Phys. Lett. B* **420** (1998) 225.

[53] G. Ambrosini *et al.*, [SPY Collab.] *Phys. Lett. B* **425** (1998) 208–214.

[54] G. Ambrosini *et al.*, [NA56/SPY Collab.] *Eur. Phys. J. C* **10** (1999) 605–627.

[55] M. Bonesini, A. Marchionni, F. Pietropaolo, and T. Tabarelli de Fatis *Eur. Phys. J. C* **20** (2001) 13–27, `arXiv:hep-ph/0101163`.

[56] T. Eichten *et al. Nucl. Phys. B* **44** (1972) 333–343.

[57] K. Abe *et al.*, [T2K Collab.] *Phys. Rev. D* **87** no. 1, (2013) 012001, `arXiv:1211.0469 [hep-ex]`. [Addendum: Phys.Rev.D 87, 019902 (2013)].

[58] M. Catanesi *et al.*, [HARP Collab.] *Nucl. Instrum. Meth. A* **571** (2007) 527–561.

[59] M. Catanesi *et al.*, [HARP Collab.] *Eur. Phys. J. C* **52** (2007) 29–53, `arXiv:hep-ex/0702024`.

[60] M. Apollonio *et al.*, [HARP Collab.] *Phys. Rev. C* **82** (2010) 045208, `arXiv:1006.1223 [hep-ex]`.

[61] M. Apollonio *et al.*, [HARP Collab.] *Phys. Rev. C* **80** (2009) 065204, `arXiv:0909.0337 [hep-ex]`.

[62] J. Sanford and C. Wang, "Empirical Formulas for Particle Production in P-Be Collision Between 10-GeV/c and 35-GeV/c," 3, 1967. BNL-11299.

[63] J. Sanford and C. Wang, "Empirical Formulas for Particle Production in P-Be Collision Between 10 and 35 BeV/c. Part II," 1967. BNL-11479.

[64] C. Wang *Phys. Rev. Lett.* **25** (1970) 1068–1072.

[65] M. Ahn *et al.*, [K2K Collab.] *Phys. Rev. D* **74** (2006) 072003, `arXiv:hep-ex/0606032`.

[66] A. Aguilar-Arevalo *et al.*, [MiniBooNE Collab.] *Phys. Rev. D* **79** (2009) 072002, `arXiv:0806.1449 [hep-ex]`.

[67] SciBooNE Collaboration web page. `https://www-sciboone.fnal.gov/data_release/flux/`.

[68] M. Catanesi *et al.*, [HARP Collab.] *Astropart. Phys.* **29** (2008) 257–281, `arXiv:0802.0657 [astro-ph]`.

[69] R. Raja *Nucl. Instrum. Meth. A* **553** (2005) 225–230.

[70] S. Mahajan and R. Raja, [MIPP Collab.], "Particle Production Measurements using the MIPP Detector at Fermilab," in *Meeting of the APS Division of Particles and Fields*. 11, 2013. `arXiv:1311.2258 [hep-ex]`.

[71] J. Paley *et al.*, [MIPP Collab.] *Phys. Rev. D* **90** no. 3, (2014) 032001, `arXiv:1404.5882 [hep-ex]`.

[72] S. M. Seun, *Measurement of* $\pi - K$ *ratios from the NuMI target*. PhD thesis, Harvard U., 2007.

[73] L. Aliaga *et al.*, [MINERvA Collab.] *Phys. Rev. D* **94** no. 9, (2016) 092005, `arXiv:1607.00704 [hep-ex]`. [Addendum: Phys.Rev.D 95, 039903 (2017)].

[74] N. Abgrall *et al.*, [NA61/SHINE Collab.] *JINST* **9** (2014) P06005, `arXiv:1401.4699 [physics.ins-det]`.

[75] S. Afanasev *et al.*, [NA49 Collab.] *Nucl.Instrum.Meth.* **A430** (1999) 210–244.

[76] S. Ilieva, [NA61/SHINE Collab.], "Hadron production measurements at NA61/SHINE for precise determination of accelerator neutrino fluxes," in *70th International conference on Nuclear physics and elementary particle physics: Nuclear physics technologies*. 10, 2020. `arXiv:2011.00277 [hep-ex]`.

[77] L. Fields and P. Podlaski, [NA61/SHINE Collab.], "Report from the NA61/SHINE experiment at the CERN SPS," Tech. Rep. CERN-SPSC-2020-023. SPSC-SR-278, CERN, Geneva, Oct, 2020.

[78] A. Aduszkiewicz *et al.*, [NA61/SHINE Collab.] *Phys. Rev. D* **98** no. 5, (2018) 052001, `arXiv:1805.04546 [hep-ex]`.

[79] A. Aduszkiewicz *et al.*, [NA61/SHINE Collab.] *Phys. Rev. D* **100** no. 11, (2019) 112004, `arXiv:1909.06294 [hep-ex]`.

[80] A. Aduszkiewicz *et al.*, [NA61/SHINE Collab.] *Phys. Rev. D* **100** no. 11, (2019) 112001, `arXiv:1909.03351 [hep-ex]`.

[81] T. Akaishi *et al.*, [EMPHATIC Collab.] `arXiv:1912.08841 [hep-ex]`. EMPHATIC: A Proposed Experiment to Measure Hadron Scattering and Production Cross Sections for Improved Neutrino Flux Predictions.

[82] G. Bellettini *Nucl. Phys.* **79** (1966) 609.

[83] A. Carroll *et al. Phys. Lett.* **B80** (1979) 319.

[84] S. Denisov *et al. Nucl. Phys.* **B61** (1973) 62.

[85] T. Sekiguchi *et al.*, [T2K Collab.] *Nucl. Instrum. Meth. A* **789** (2015) 57–80, `arXiv:1502.01737 [physics.ins-det]`.

[86] D. Beavis *et al.*, [E899 Collab.], "Long Baseline Neutrino Oscillation Experiment at the AGS Approved by the HENPAC as AGS Experiment 889," 1995. BNL-52459.

[87] J.-M. Levy, "Kinematics of an off axis neutrino beam," 2010. `arXiv:1005.0574 [hep-ex]`.

[88] K. Abe *et al.*, [T2K Collab.] *Phys. Rev. D* **88** no. 3, (2013) 032002, `arXiv:1304.0841 [hep-ex]`.

[89] J. Altegoer *et al.*, [NOMAD Collab.] *Nucl. Instrum. Meth. A* **404** (1998) 96–128.

[90] I. Giomataris, R. De Oliveira, S. Andriamonje, S. Aune, G. Charpak, P. Colas, A. Giganon, P. Rebourgeard, and P. Salin *Nucl. Instrum. Meth. A* **560** (2006) 405–408, `arXiv:physics/0501003`.

[91] Y. Nakano, [Super-Kamiokande Collab.] *J. Phys. Conf. Ser.* **1342** no. 1, (2020) 012037.

[92] Y. Ashie *et al.*, [Super-Kamiokande Collab.] *Phys. Rev. D* **71** (2005) 112005, `arXiv:hep-ex/0501064`.

[93] J. Hosaka *et al.*, [Super-Kamiokande Collab.] *Phys. Rev. D* **74** (2006) 032002, `arXiv:hep-ex/0604011`.

[94] A. Takenaka *et al.*, [Super-Kamiokande Collab.], "Search for Proton Decay via $p \to e^+\pi^0$ and $p \to \mu^+\pi^0$ with an Enlarged Fiducial Volume in Super-Kamiokande I-IV," 2020. `arXiv:2010.16098 [hep-ex]`.

[95] T. Kajita, E. Kearns, and M. Shiozawa, [Super-Kamiokande Collab.] *Nucl. Phys. B* **908** (2016) 14–29.

[96] Super-Kamiokande web page, 2020. `http://www-sk.icrr.u-tokyo.ac.jp/sk/index-e.html`.

[97] L. Marti-Magro *PoS* **ICRC2019** (2020) 957. SuperK-Gd: The Gd future of Super-Kamiokande.

[98] A. Murakami, *Measurement of Neutrino Oscillation Parameters with the Precise Nuetrino Flux Prediction in the T2K Experiment.* PhD thesis, Kyoto U., 2013. T2K-THESIS-034.

[99] T. Vladisavljevic, *Predicting the T2K Neutrino Flux and Measuring Oscillation Parameters.* PhD thesis, Oxford U., Cham, 2020. T2K-THESIS-116.

[100] A. Ferrari, P. R. Sala, A. Fasso, and J. Ranft, *FLUKA: A multi-particle transport code (Program version 2005)*, 10, 2005. CERN-2005-010.

[101] T. Böhlen, F. Cerutti, M. Chin, A. Fassò, A. Ferrari, P. Ortega, A. Mairani, P. Sala, G. Smirnov, and V. Vlachoudis *Nucl. Data Sheets* **120** (2014) 211–214.

[102] G. Battistoni, S. Muraro, P. R. Sala, F. Cerutti, A. Ferrari, S. Roesler, A. Fasso, and J. Ranft *AIP Conf. Proc.* **896** no. 1, (2007) 31–49.

[103] C. F. Brun R., *GEANT Detector Description and Simulation Tool, CERN Program Library Long Writeup W5013*, 1993. CERN-W-5013.

[104] C. Zeitnitz and T. Gabriel, "The GEANT-CALOR interface," in *3rd International Conference on Calorimetry in High-energy Physics (Note: dates changed from Oct 6-9)*, pp. 394–404. 9, 1992.

[105] C. Strabel, *Evaluation of Particle Yields in 30 GeV Proton-Carbon Inelastic Interactions for Estimating the T2K Neutrino Flux.* PhD thesis, 2011. CERN-THESIS-2011-295.

[106] N. Abgrall *et al.*, [NA61/SHINE Collab.] *Phys. Rev.* **C84** (2011) 034604.

[107] T. Vladisavljevic, "Constraining the T2K Neutrino Flux Prediction with 2009 NA61/SHINE Replica-Target Data," in *Prospects in Neutrino Physics*, pp. 189–193. 4, 2018. `arXiv:1804.00272 [physics.ins-det]`.

[108] L. Aliaga *et al.*, [MINERvA Collab.] *Nucl. Instrum. Meth. A* **743** (2014) 130–159, `arXiv:1305.5199 [physics.ins-det]`.

[109] C. Bovet, R. Maleyran, L. Piemontese, A. Placci, and M. Placidi, *The Cedar Counters for Particle Identification in the SPS Secondary Beams: A Description and an Operation Manual.* 1982. CERN-82-13.

[110] W. Blum, L. Rolandi, and W. Riegler, *Particle detection with drift chambers.* Particle Acceleration and Detection. 2008.

[111] A. Aduszkiewicz, *Energy dependence of negatively charged pion production in proton-proton interactions at the CERN SPS.* PhD thesis, Warsaw U., 2016. CERN-THESIS-2016-010.

[112] M. Pavin, *Measurements of hadron yields from the T2K replica target in the NA61/SHINE experiment for neutrino flux prediction in T2K.* PhD thesis, University of Paris VI, 2017. CERN-THESIS-2017-233.

[113] M. Deveaux *et al.*, [NA61/SHINE Collab.] *EPJ Web Conf.* **171** (2018) 10003.

[114] B. Rumberger *et al. JINST* **15** no. 07, (2020) P07013, `arXiv:2004.11358 [physics.ins-det]`.

[115] R. Sipos, A. Laszlo, A. Marcinek, T. Paul, M. Szuba, M. Unger, D. Veberic, and O. Wyszynski *J. Phys. Conf. Ser.* **396** (2012) 022045.

[116] S. Argiro, S. Barroso, J. Gonzalez, L. Nellen, T. C. Paul, T. Porter, J. Prado, L., M. Roth, R. Ulrich, and D. Veberic *Nucl. Instrum. Meth. A* **580** (2007) 1485–1496, `arXiv:0707.1652 [astro-ph]`.

[117] N. Abgrall, [NA61 Collaboration Collab.], "Calibration and Analysis of the 2007 Data," Jul, 2008. CERN-SPSC-2008-018.

[118] S. Agostinelli *et al.*, [GEANT4 Collab.] *Nucl. Instrum. Meth.* **A506** (2003) 250.

[119] J. Allison *et al.*, [GEANT4 Collab.] *IEEE Trans.Nucl.Sci.* **53** (2006) 270.

[120] J. Allison *et al.*, [GEANT4 Collab.] *Nucl. Instrum. Meth.* **A835** (2016) 186–225.

[121] CERN ROOT web page, 2020. `https://root.cern/`.

[122] Toyo Tanso graphite. `https://www.toyotanso.com/Products/Special_graphite/data.html`.

[123] N. Abgrall *et al.*, [NA61/SHINE Collab.] *Phys. Rev.* **C85** (2012) 035210.

[124] N. Abgrall *et al.*, [NA61/SHINE Collaboration Collab.] *Phys.Rev.* **C89** no. 2, (2014) 025205, `arXiv:1309.1997 [physics.acc-ph]`.

[125] N. Abgrall *et al.*, [NA61/SHINE Collab.] *Nucl. Instrum. Meth.* **A701** (2013) 99.

[126] N. Abgrall *et al.*, [NA61/SHINE Collab.] *Eur. Phys. J. C* **76** no. 2, (2016) 84, `arXiv:1510.02703 [hep-ex]`.

[127] N. Abgrall *et al.*, [NA61/SHINE Collab.] *Eur. Phys. J. C* **76** no. 11, (2016) 617, `arXiv:1603.06774 [hep-ex]`.

[128] N. Abgrall *et al.*, [NA61/SHINE Collab.] *Eur. Phys. J.* **C79** no. 2, (2019) 100, `arXiv:1808.04927 [hep-ex]`.

[129] A. Acharya *et al.*, [NA61/SHINE Collaboration Collab.] *Phys. Rev. D* **103** (Jan, 2021) 012006.

[130] W. Leo, *Techniques for Nuclear and Particle Physics Experiments: A How to Approach.* Springer, 1987. 978-3-540-57280-0.

[131] I. Endo, T. Kawamoto, Y. Mizuno, T. Ohsugi, and T. Takeshita *Nucl. Instrum. Meth.* **188** (1981) 51.

Acknowledgements

Writing this thesis completes a process of skills and knowledge building that spans over a few years. And during that period many people contributed to different aspects of the work involved, for which I would like to thank them.

I would like to express my gratitude to my supervisor, Mariyan Bogomilov, for setting up the framework of my doctorate and supporting my participation in various activities both within and outside the university. I would also like to thank Dimitar Kolev for the time he spent actively helping me out with simulations and the numerous discussions we had, whose scope reach a lot further than the topic of this thesis. To both of them, I am grateful for their guidance and patience through the different stages of my education.

I would also like to thank my colleagues at NA61/SHINE for their cooperativeness and friendly regard. Special thanks go to the members of the Neutrino community for sharing their expertize and providing practical advice during the ups and downs of this analysis.

I am profoundly grateful to my family and friends for the love, understanding, and support they have always given me. This thesis, in particular, would have never been possible without these solid foundations!